Studies of the Ionization Energy Loss in the DELPHI TPC and the Identification of Quark and Gluon Jets in Hadronic Events at LEP

O.Bärring

Department of Particle Physics
University of Lund
Sölvegatan 14
S-223 62 Lund
Sweden

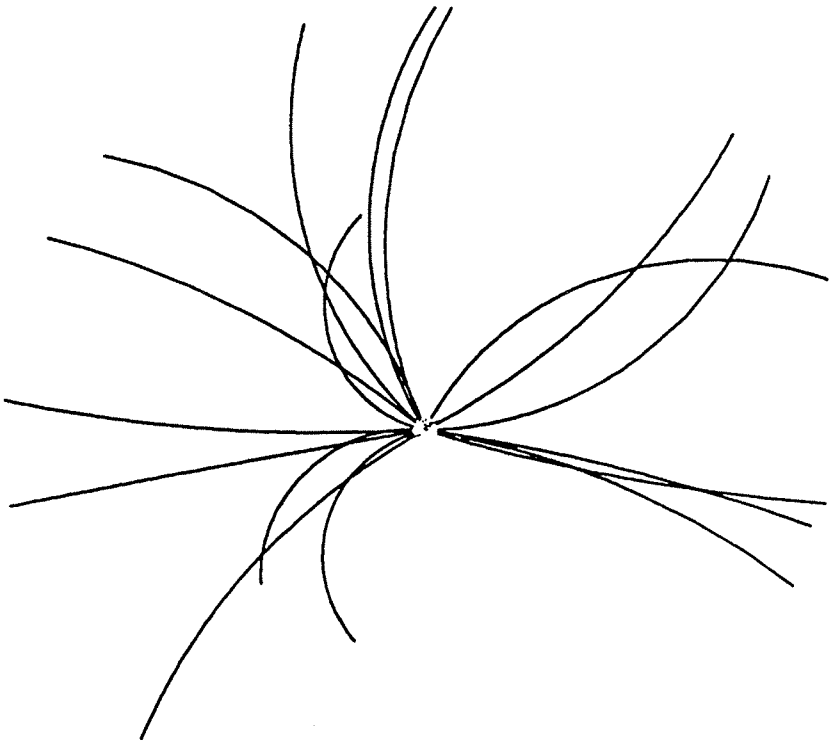

ISBN 91-628-0701-3
LUNFD6/(NFFL-7071)1992

Studies of the Ionization Energy Loss in the DELPHI TPC and the Identification of Quark and Gluon Jets in Hadronic Events at LEP

By due permission of the faculty of mathematics and natural science of the University of Lund to be publicly discussed at the lecture hall B of the department of Physics, October 2 1992, at 10.15 a.m., for the degree of doctor of philosophy

by
O.Bärring

Department of Particle Physics
University of Lund
Sölvegatan 14
S-223 62 Lund
Sweden

This thesis is based on five papers

1 The DELPHI Time Projection Chamber
Nucl. Instr. Methods A283 (1989) 567

2 Energy Loss Calculations with Fast Fourier Transform Routines
Nucl. Instr. Methods A284 (1989) 459

3 Jet Classification with a Neural Network
DELPHI 90-59 PHYS 78 (1990)

4 Quark/Gluon Classification with Fragmentation Sensitive Variables
DELPHI 92-38 PHYS 170 (1992)

5 Evidence for the Triple-Gluon Vertex from 4-Jet Events at LEP (addendum)
Submitted to the XXVI International Conference in High Energy Physics **Dallas**, Texas, USA, **August 5-12 1992**.
DELPHI 92-70 PHYS 181 (1992)

Abstract

In this thesis a fast and accurate method for the calculations of the energy loss spectrum is presented. The algorithm, which is based on the Laplace transform method, differs from earlier approaches in that it makes use of Fast Fourier Transform routines instead of numerical integration or series expansion.

We present also a new type of jet classification, based on Artificial Neural Network technique. The classification is proved to be insensitive to the jet energy, i.e. it exploits only the fragmentation differences between quarks and gluons. We apply this method in a measurement of the triple-gluon vertex in four-jet events at LEP.

Contents

Foreword

This report summarizes my more than four years long participation in the DELPHI collaboration. Evidently only the successes are accounted for; the large number of side-tracks and novice mistakes committed are omitted, as they usually have interest to nobody but possibly myself. The search for anomalous charged particles presented in section 1.5 serves as an exception. My part in that uncomplete analysis is limited to the writing and tuning of the tagging code and accordingly that section should be regarded as a contribution to the DELPHI software rather than a physics study. During the tests of the TPC in 1988 to 1989 I took on a small part, mainly writing software for testing the shapers, which I choose not to recount. This is partly because a description of the various FASTBUS routines, addressing modes, registers etc. would be very tedious for the reader.

The present thesis is based on five articles (or rather two articles, one conference contribution and two internal DELPHI notes) [16, 23, 24, 25], which are enclosed in the appendices A to E. The first paper [3] describes the DELPHI TPC, in which collaboration I have been a member since 1987. The other four papers have I been personally responsible for. Chapter 2 concerns a method for the calculation of ionization energy loss, which is presented in the article [16] (appendix B). The DELPHI notes [24, 25] (appendices C, D), which describe a method for identifying the parton origin of a hadronic jet, are reviewed in the section 3.2. Finally the addendum [23] (appendix E) to a DELPHI measurement of the triple-gluon coupling presented as a contribution at the 1992 Dallas conference [22] is discussed in section 3.3.2 and 3.3.3.

Throughout the text there are not many indications on what exactly I have done and what have been done by others. This is in particular true for the last chapter. Whenever appropriate I have tried to point out my own part by making citations to the five papers mentioned above. However, trying to do this consequently would greatly disturb the text and for that reason I wish here to make some clarifications. Since 1987 I have been connected to the TPC subdetector group of DELPHI where my main contribution is the software for the *calculation* of ionization energy loss. My code is used in the particle identification but I am *not* responsible for that part, although I have of course been working in close collaboration with the people concerned. Further, though less important, I have prepared the simulation code for the upgrade to faster wire electronics and been involved in the writing of the corresponding reconstruction code. As already mentioned I have written the tagging code for the search of anomalous charged particles. However, the tagging criterias were of course set up in collaboration with the physics team. For the four-jet analysis presented in the last chapter my contribution was the application of a new method for the identification of the jets. The method itself of measuring N_C/C_F and T_R/C_F was *not* mine and had, in fact, already been practiced in DELPHI. Here again, I have of course been working in close collaboration with the people in concern.

Chapter 1

Apparatus

DELPHI, a DEtector with Lepton, Photon and Hadron Identification, is one of the four experiments operating at LEP, the Large Electron Positron collider. This chapter is intended as a brief introduction to LEP and the subdetectors of DELPHI that are relevant for the analysis in the coming sections. Emphasis is put on describing the TPC, Time Projection Chamber, the principal tracking device of DELPHI, since it is important for the verification of the *ionization energy loss* calculations in chapter 2. The online data acquisition together with the offline reconstruction software are discussed and in particular an interactive implementation of data unpacking and analysis is proposed. Finally, as an example on offline data processing, the tagging code for anomalous charged particles, e.g. free quarks, is described.

1.1 LEP, Large Electron Positron collider

LEP, an e^+e^- collider ring with 27 kilometer circumference, was constructed in the years 1982 to 1989. It is resident in an underground tunnel outside Geneva at the border between Switzerland and France. The machine was ready for physics in the summer 1989 and the *pilot* run took place with start the 14th of August the same year.

After an acceleration phase in the PS and SPS the projectiles, the electrons and positrons, are injected into LEP as four bunches of about 10^{11} particles each. In LEP the particles are accelerated further from an energy of 20 GeV up to about 46 GeV where they are kept for several hours. The bunches can be imagined as thin ribbons with 300 μm width, 12 μm thickness and 1.5 cm length. The energy loss, due to synchrotron radiation, of about 120 MeV per completed turn at 46 GeV, is compensated for in acceleration cavities situated at two straight sections of LEP.

LEP was designed to profit from the increase in the e^+e^- annihilation cross section due to the presence of the electro-weak gauge boson, Z^0, resonance ($\sigma \sim 40$ nb at $\sqrt{s} = 92$ GeV). In a second stage of operation, foreseen to the middle of the 1990's, the LEP machine will reach an energy of about 200 GeV, thus being able to benefit from the W^+W^- production resonance.

The nominal luminosity of $1.6 \cdot 10^{31} cm^{-2} s^{-1}$, corresponding to 3 millions Z^0s per detector and year of 1500 hours running, has not been reached during the first 3 years of operation. The number of detected Z^0 events in DELPHI during 1989, 1990 and 1991 were about 10^4, $1.3 \cdot 10^5$ and $3.8 \cdot 10^5$ respectively.

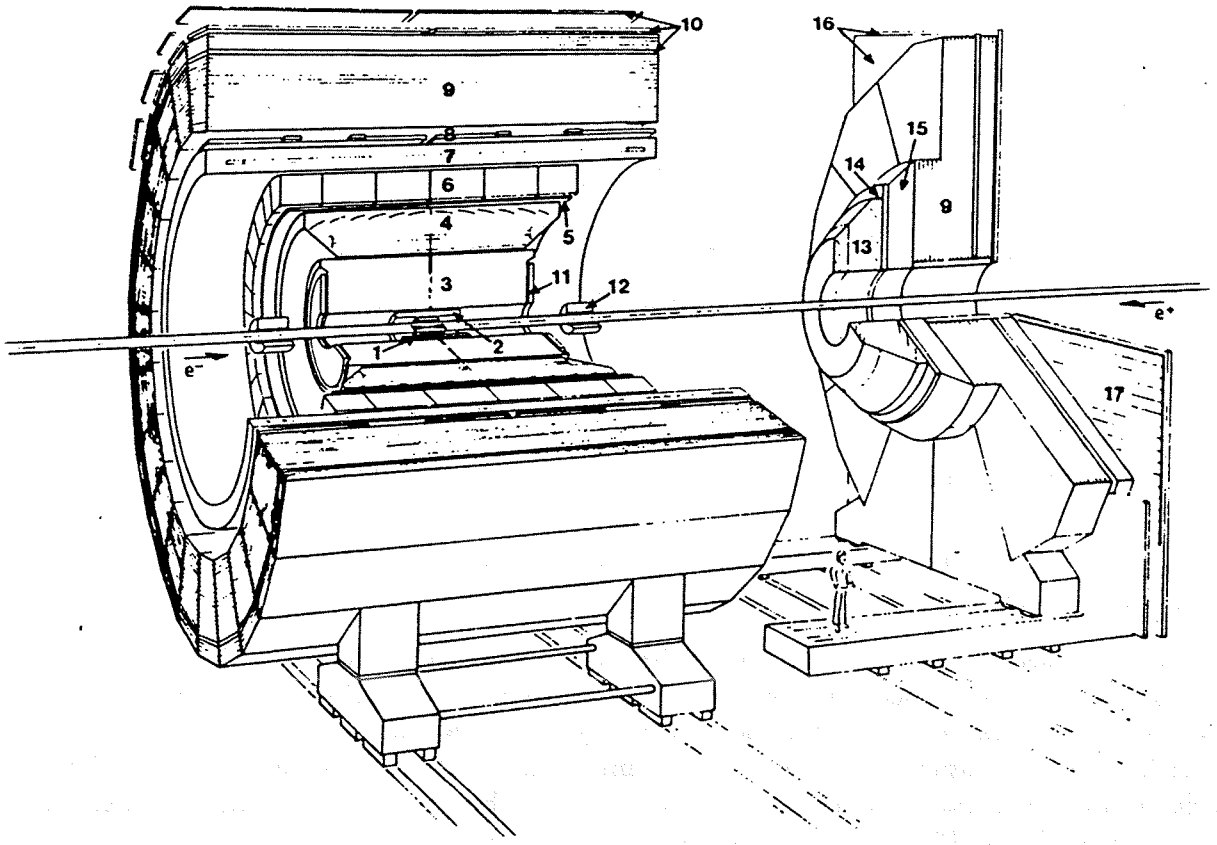

Figure 1.1: Perspective view of the DELPHI detector. 1=Micro-vertex Detector. 2=Inner Detector. 3=Time Projection Chamber. 4=Barrel Ring Imaging Cherenkov Counter. 5=Outer Detector. 6=High density Projection Chamber. 7=Superconducting Solenoid. 8=time of Flight Counters. 9=Hadron calorimeter. 10=Barrel Muon chambers. 11=Forward Chamber A. 12=Small Angle tagger. 13=Forward Ring Imaging Cherenkov Counter. 14=Forward Chamber B. 15=Forward Electromagnetic calorimeter. 16=Forward Muon Chambers. 17=Forward Scintillator Hodoscope.

1.2 DELPHI

The DELPHI detector is depicted in Figure 1.1 In this section, the subdetectors for tracking of charged particles, ID, TPC and OD and the electromagnetic calorimeters HPC and FEMC will be described. For a more thorough treatment of all the submodules in DELPHI refer to [1] and the references given therein.

1.2.1 The Inner Detector, ID

The ID [2] is the innermost multiwire detector around the beampipe. With the inner and outer radii of 116 and 280 mm respectively, and a length along the beampipe of $|z| < 50$ cm it covers an angular region $17° < \Theta < 163°$. The detector consists of two concentric layers:

- a jet type chamber to measure accurately the trajectory of the outgoing particles in the plane perpendicular to the primary beams

active length	2×134 cm
radius	32.5 – 116 cm
volume	$\sim 14\ m^3$
gas	80% argon +20% CH_4 at 1 atm.
electric field	150 V/cm

Table 1.1: Main characteristics of the DELPHI TPC.

- five layers of proportional chambers which measure the coordinate along the beam direction via cathode strip readout.

The jet-chamber has 24 azimuthal sectors with 24 sens wires each, giving the $R\Phi$-coordinates of the track. The gas and operating point where chosen to produce a drift velocity proportional to the total drift distance to facilitate fast triggering; a time window of $\sim$ 100 ns determines the position and straightness to better than 1-2 mm for a radial track coming from the origin. Provided a transverse momentum of more than 1.5 GeV/c the track bending and displacement can be neglected in the 10 cm of track segment seen by the jet chamber.

The five cylindrical MWPC layers, 8 mm deep, have each 192 wires and 192 circular cathode strips. The sens wires are spaced about 8 mm apart and interleaved with field wires. They provide fast trigger information and resolve left/right ambiguities from the jet section.

The resolution has been measured with cosmic ray and beam tests: single point resolution $\sigma_{R\Phi} = 90\mu$m in the jet-chamber and $\sigma_z < 1$ mm for the outer layers. The trigger efficiency for the jet-chamber is above 90% for jet events. The outer layers give $> 95\%$ trigger efficiency for single tracks.

1.2.2 The Time Projection Chamber, TPC

The TPC [3] is the central tracking device of the DELPHI experiment. It was primary designed for good tracking purpose, whereas for the particle identification DELPHI contains a dedicated detector, the Ring Image CHerenkov (RICH) counter. However, a limited particle identification by dE/dx, in particular e/π separation below 8 GeV, was still foreseen. The main characteristics of the TPC are listed in Table 1.1.

The detector consists essentially of two large drift volumes, separated by the central drift anode, and the two end-caps. The central anode is set to –20 kV and the drift field is degraded by a chain of 333 high precision 4 MΩ resistors connected to Cu strips on the inner and outer field cages. With a nominal drift field of 150 V/cm, the drift velocity is $v_D = 66.94 \pm 0.07$ mm/μs at T=22°C and the maximum drift time $\sim$ 20 μs.

The circular end-caps are subdivided in 2×6 sectors equipped with multiwire proportional chambers, MWPC's. Each chamber contains three wire planes: a gate grid, a cathode wire plane and a sense + field wire plane. The base plate is coated with 70 μm copper on which are engraved 16 circular rows of capacitive pads. A schematic view of a segment of the end-plate is shown in Figure 1.2.

The **cathode wire** plane, which is connected to ground (0 V) voltage, defines the border between the drift volume and the proportional gap. The wires have 75 μm diameter and the

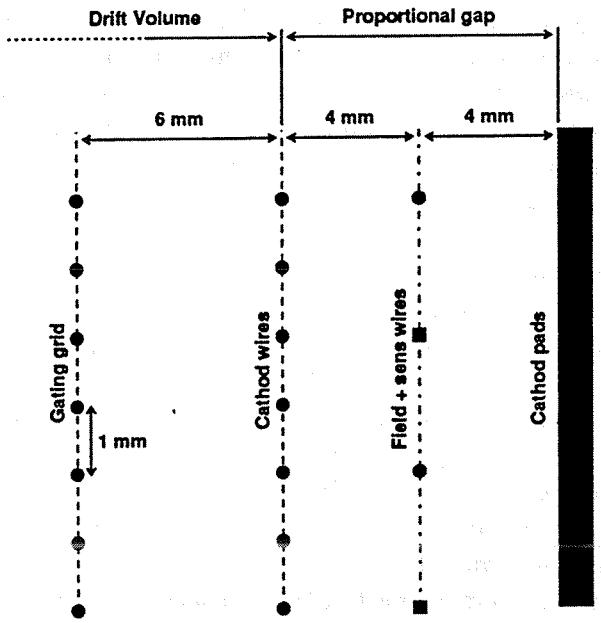

Figure 1.2: A segment of the end-plate showing the wire plane arrangement and the cathode pads.

spacing is 1 mm.

The **sense wire** plane with 192 wires spaced 4 mm, constitute the anode of the proportional chamber. The thin sens wires, ø= 20 μm, are set to a high voltage of 1385 V (1435 V from March 1991) so that the ionization electrons coming from the drift volume will induce an avalanche which is proportional to the primary ionization. The amplification factor is about 20000. To eliminate mutual electrostatic influence between neighbouring sens wires, they are interspersed with field wires which hold a potential of 60 V. Thus, each sens wire can be regarded as an independent proportional cell which is important for the measurement of ionization energy loss, dE/dx, see Chapter 2.

The positive ions, mainly CH_4, created in the avalanche, drift slowly (0.34 cm/ms) towards the central anode. At high event rate an accumulated free positive charge in the drift volume may cause serious distorsions to the drift field, which is the reason for the **gating grid**. The gating grid, situated 6 mm out from the cathode wire plane, consists of 1 mm spaced wires. In *dynamic* mode the gate is closed by applying a potential of $\pm$150 V to consecutive wires. The electric field induced between each wire pair will capture both the entering electrons and exiting ions. During 3 μs after each beam crossing the gate is opened by setting all wires to –150 V which allows electron transparency for a first level trigger decision. In case of a positive response the gate is kept open during the full drift time (22 μs) of the electrons, else it is closed immediately.

With the low luminosities in 1989 and 1990 the gating grid was not needed and consequently kept off. In 1991 it was put in a *static* mode with an fixed semi-transparent field induced by biasing consecutive wires to –150 V $\pm$20 V. This permitted a capture of positive ions without distorting the drift field lines too much. On the other hand a small part of the electrons was

also captured, which slightly affected the dE/dx resolution.

The chamber electronics provides the analog information from the in total 22 464 channels of the TPC (12×1680 pads and 12×192 wires). Directly mounted on the end-plate backplane are low noise hybridized MOSFET preamplifiers. The amplified signals are feed through 30 m of *twisted pair* cables (18 pairs per cable) to the TPC control room. The pulses acquire Gaussian shape through a two-stage active filter amplifier, the shaper, mounted in one slot wide FASTBUS modules of 32 channels each. The shaping procedure, which retains the integrated amplitude, is important for good charge measurement. The final analog pulses have about 180 ns width. Sampling and digitization of the shaped pulses are accomplished by 8-bit Flash Analog to Digital Converters (FADC) running at 13.5 MHz. The response function of the FADC has broken characteristics: 6 mV steps up to the breaking point at channel 191 and 29.7 mV from 192 to 255. The three slots wide *digitizer* contains 48 daughterboards of two FADC's each. The same FASTBUS unit houses a zero suppression (ZS) card; only time clusters with at least two adjacent signals, that are bigger than a defined threshold, are recorded. At the current working frequence both pad and wire signals are sampled with a pixel time of 73.82 ns but, in order to improve the two-track separation, an upgrade to three times the frequence of the wire digitization is foreseen.

The remaining part of the data acquisition system, common to all the submodules in DELPHI, will be described in section 1.3.

With the delayed installation of the RICH extensive efforts have been made to improve the particle identification capabilities of the TPC. For argon at atmospheric pressure and > 4 mm sampling one can expect a dE/dx resolution: $\sigma(dE/dx) \sim 5.5\%$ [4]. This is to be compared to the 3.65% of the Berkeley TPC [5] which had the same sampling but 8.5 atm. pressure. After correction of numerous effects, e.g. track angle, drift distance, track separation, sector edge effects etc. the resolution is 6.2% for minimum ionizing particles and 5.7% for electrons. The e/π separation works efficiently up to 5 GeV/c momentum. Truncated mean (80% of the lowest amplitudes are kept) is used as estimator though attempts have been made to use the Kolmogorov distance between the measured ionization spectrum and the calculated distributions of chapter 2, for the mass hypotheses e, μ, π, K and p. Those latter attempts have so far failed partly due to structures occuring in the calculated Landau spectra for small values on xP (sample-length $\times$ pressure) which cannot be seen in data, see chapter 2.

The space point determination is done assuming Gaussian shape of the signals over adjacent pads. For tracks with P_T greater than 1.5 GeV/c the average resolution is found to be 230 μm in $R\Phi$ and 900 μm in z.

1.2.3 The Outer Detector, OD

The outermost tracking detector [6] in the barrel is situated in the radial region 1.97 to 2.08 m from the beampipe. It consists of 3480 individual drift tubes arranged in 24 modules of five staggered layers each, mounted on the B-RICH (Barrel Ring Image CHerenkov detector). An overlap between adjacent modules ensures full azimuthal coverage. The drift tubes have an active length of 4.5 m and a square cross section with the inner dimension 1.65×1.65 cm^2 and they are operating in *limited streamer mode.* In addition to the $R\Phi$ information given by all the layers, three of them also provides a fast z measurement by relative timing of signals from both ends. Thus, the OD is essential to provide fast trigger information in both $R\Phi$ and z.

The measured resolution $\sigma_{R\Phi} = 110$ μm and $\sigma_z = 4.4$ cm is a significant improvement from the original specification of $\sigma_{R\Phi} = 300$ μm and $\sigma_z = 7$ cm.

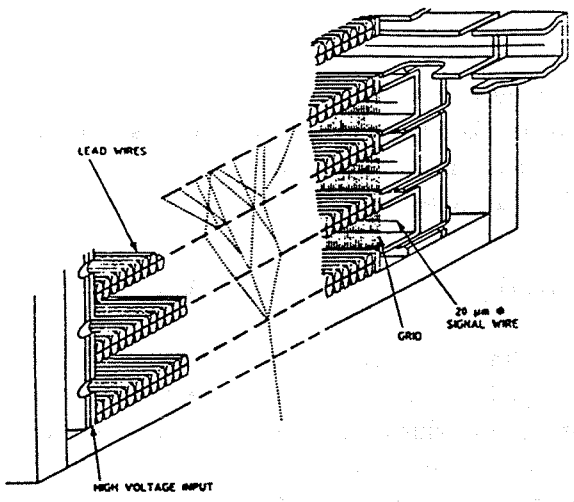

Figure 1.3: Details of a module in the High density Projection Chamber (HPC).

1.2.4 The High-density Projection Chamber, HPC

Combining the time-projection principle with calorimetry enables good energy resolution together with a complete representation of the energy flow. The DELPHI HPC [7] is one of the first large scale applications of this idea. The detector consists of 144 modules arranged as 24 sectors in azimuth of 6 modules each along z. The module, Figure 1.3, is separated in a converter/drift part and a proportional wire chamber. The converter walls are made of thin trapezoidal lead wires glued onto both sides of a flat fiberglass epoxy substrate. The 8 mm spacings between the lead walls constitute the drift chambers, 40 in one module. The drift field is provided by a voltage gradient between neighbouring lead wires in the converter wall. The primary ionization from the showers drift along those narrow sampling slots to the proportional wire chamber. The radial and azimuthal coordinates are sampled by pad readout of the proportional chamber; nine-fold radial and 1° azimuthal sampling. A 4 mm granularity of the drift coordinate z is obtained by 15 MHz 8-bit FADC's with bilinear conversion characteristics.

A study [8] has shown that for the 1990 data the energy resolution of the HPC was given by $\sigma_E/E = 25.3\%/\sqrt{E} + 7\%$ (E in GeV) where the second term is due to energy loss in the material before the HPC, leakage, gas saturation, calibration fluctuations, instabilities etc. An ageing of the readout chambers of the HPC has been observed as a degradation of the response which is proportional to the gas gain. As a consequence it was decided in 1991 to lower the readout voltage from 1300 V to 1200 V. After this change the data show better stability and no further corrections to chamber response were needed [9].

1.2.5 The Forward Electromagnetic Calorimeter, FEMC

The FEMC [10] is a lead glass calorimeter with vacuum phototriode readout. A total of 9064 lead glass blocks in form of truncated pyramids are mounted in a "quasi-pointing" arrangement on two 5 m diameter disks. The detector covers the angular regions $10° < \Theta < 36.5°$ and $143.5° < \Theta < 170°$.

The front face dimension $\sim 5 \times 5$ cm^2 of the lead glass blocks corresponds to an angular resolution of about $1° \times 1°$. The counters are 20 radiation lengths deep. The quasi-pointing geometry ensures that electrons and photons cannot remain undetected due to passing through

passive material between the counters.

At LEP the energy resolution for Bhabhas at 45 GeV has been measured to be 6%, using calibration constants from test beam results. By using part of the data to correct the calibration constants the energy resolution improved to 4%.

1.3 The Data Acquisition System, DAS

The DELPHI DAS is a well defined hierarchy of 6 – 7 (depending on the subdetector) levels of data merging and processing; from the readout of the Front End Buffers of the individual FASTBUS modules up to data monitoring and logging onto mass storage in the Data Acquisition host computer. At all levels both the hardware and software elements are highly standardized. An extensive treatment of the system may be found in [11], here follows a less detailed summary.

1.3.1 Hardware

The basic processor unit in the readout system is a specially designed *Fastbus Intersegment Processor*, FIP. It is a two slots wide FASTBUS module containing a Motorola 68020 processor, 1.5 Mbytes of dynamic RAM and 256 kbytes static RAM. As from 1991 the FIP is equipped with Ethernet-Cheapernet port allowing remote login for software development and maintenance. The operating system, OS9, the communication packages and some development tools are stored in 1 Mbyte of EPROMs. DELPHI uses about 70 FIPs.

From the FASTBUS level and onwards the online cluster comprises thirteen μVAX-II computers and one of each VAX 8700, VAX 4000 and μVAX 3500. In addition there is a growing number of VAXstation 3100 for interactive activities of the individual detector groups. The local area VAX clusters are running the VMS operating system. The data are collected from FASTBUS and entered into the μVAXes or the central VAX 8700 by a CERN FASTBUS Interface (CFI) or a CERN Host Interface (CHI).

1.3.2 Software

The Data Acquisition software is organized around a newly developed CERN written concept called *Model* [12], which consists of several packages each dedicated for a specific task in a large data acquisition system, e.g. buffer handling, error logging and reporting, human interface. The control of the individual partitions and the central run control of the experiment are managed by the *State Managers* [13] which run as independent processes. In its context the individual components of the system, e.g. the CFI servers and the readout supervisors, are represented by abstract final state machines called *objects*. A special language, the State Manager language, and an associated compiler have been developed for specifying the interaction between the various objects in a State Manager domain.

1.3.3 Data readout and flow

Due to obvious differences in measurement tasks the subdetectors need to use their own hardware up to a certain level, e.g. for the shaping and digitization of the analog signals of the TPC described in 1.2.2. The output from the digitization modules of each detector is put into the Front End Buffers (FEB)[1]. From this point the DAS hardware is completely standardized.

[1] In some cases, for the detector with a large number of channels, a second level of buffering has been added called Board Event Buffer (BEB).

The Front End Buffers are read out by the Crate Processors (CP). The CP communicates with the trigger control system in order to coordinate the readout with the LEP beam crossing. It performs data formatting and some first processing, e.g. pedestal subtraction.

The Crate Processors are driven and supervised by the Local Event Supervisor (LES). The LES receives the data from the CPs, merges it and performs a first formatting and linking of the data to its final (ZEBRA-) structure. A decision is taken, according to user defined criteria, whether the event is worth further processing. The subdetectors, or *partitions* in the DAS formalism, run one LES each with a few exceptions e.g. the TPC which consists of two partitions and thus runs two LESs.

The Global Event Supervisor (GES) controls the LESs. It makes a fast transfer of the data from the LESs to its own buffer. The GES performs the final formatting of the data, which now is ready for logging onto mass storage by the main data acquisition host computer, the VAX 8700.

Both the Crate Processors and the Local Event Supervisors run in FASTBUS Intersegment Processors, see 1.3.1, and in some cases they share the same processor. Also the Global Event Supervisor is running on a FIP.

In 1990 the trigger rate was of the order a few Hz with an average event size of about 50 kbytes and a peak size around 200 kbytes.

1.4 Offline Reconstruction and Simulation Software

As DELPHI is a quite complicated detector containing 16 different subdetectors which are dynamically improving for better performance, one cannot expect the offline software to be perfectly structured and fully comprehensible. Many people are involved; each subdetector group provides its own simulation and reconstruction code, the physics teams write their specific tagging code for the production of the Data Summary Tapes (DST). In addition there are a large number of utility packages and stand alone programs. Unavoidably the continuos development together with the necessity of backward compatibility render a top-down programming style in particular for the subdetector dependent code. Non-experts entering into, for instance, the TPC ANAlysis package, TPCANA, may have problems finding their way out again. In contrast more or less static code like the steering skeletons of the standard DELPHI simulation and reconstruction programs DELSIM and DELANA or the Track ANAlysis and GRAphical package (TANAGRA) are very well organized and understandable. Those three will be described in the following sections. An example on how the analysis of DELPHI data can be combined with the powerful and very flexible CERN written program PAW (Physics Analysis Workstation) is given in the last subsection.

1.4.1 The DELPHI simulation program, DELSIM

Contrary to the other LEP experiments, the DELPHI collaboration decided not to use the GEANT simulation package but rather to develop its own simulation program, DELSIM [14]. The program consists of four main parts: the event generation, the detector description, the detector simulation and the output routines. DELSIM is controlled by a large number of run control cards specified by the user in a special *control card file*, which is read at initialization.

The event generation, being the physics part of the program, is maintained by a number of built in standard e^+e^- generators. In addition there exist a single particle generator and a facility to interface user supplied generators. The particular generator and decay channel of interest are selected by run control cards. For each generated event DELSIM calls an user

routine for a decision whether to reject the event or pass it to the time consuming detector simulation.

The detector simulation is essentially the tracking of each generated particle through the various materials in the detector. A number of secondary processes need to be simulated: delta rays, bremsstrahlung, pair production, Compton scattering, decays, nuclear interactions, positron annihilation and photoelectric effect. Particles produced in secondary processes are followed in the same way as the generated particles. For hadronic showers DELPHI recently adapted to the GEISHA simulation program. The detector description (geometry and calibration constants) is kept on a structured data base which is continuously updated according to the actual detector conditions. Since the data base contains the full history of the detector, the user may freely select (through run control cards) the date and time in the past to be simulated.

In the full simulation of individual detector modules, space points or showers are determined and converted to final electronic channel pulse heights with realistic noise and background signals added. Each subdetector group prepares its own simulation code which DELSIM refers to through five entry points:

- The beginning of the program execution, e.g. initialization of detector constants, histogram booking.
- Preparation for new event, e.g. reserve temporary buffers to hold the track information.
- Full simulation for every track entering the module. Simulate electronic response, add noise and background.
- End processing of the event, e.g. save simulated tracks to raw data file.
- End of execution. Print out statistics etc.

The output of DELSIM contains exactly the same raw data structure as the real data from the detector. Optionally one may also choose to output the particle vectors so that later the reconstruction of the raw data can be compared with the "truth".

1.4.2 The DELPHI reconstruction program, DELANA

DELANA [14] is by far the largest DELPHI offline program. Currently the executable image occupies about 21 Mbytes of disk space on the CERN central VAX cluster. It takes as input the raw data from the detector or DELSIM (see section 1.4.1) and performs a full reconstruction of the events. The output normally does not need any further processing before being used in physics analysis.

A schematic program flow chart is shown in Figure 1.4. At start of run the memory resident data storages are initialized, I/O and data base files are opened. The Track ANAlysis and Graphics package, TANAGRA [14], provides a well defined data structure for storing track and vertex information. Since the main event loop essentially reflects the structure of TANAGRA they will both be described in the syntax of the latter.

The standard DELPHI I/O package, UX, reads into the memory the raw data of a new event. The subdetector modules compare the event date and time with those of the current data base information and, if necessary, access the data base for retrieval of updated detector constants. Then the raw data is calibrated and entered into the TANAGRA **Detector data** (TD) banks, which are input to the local track search. The subdetector modules (not all modules are involved) perform a pattern recognition among their TD information and put the resulting

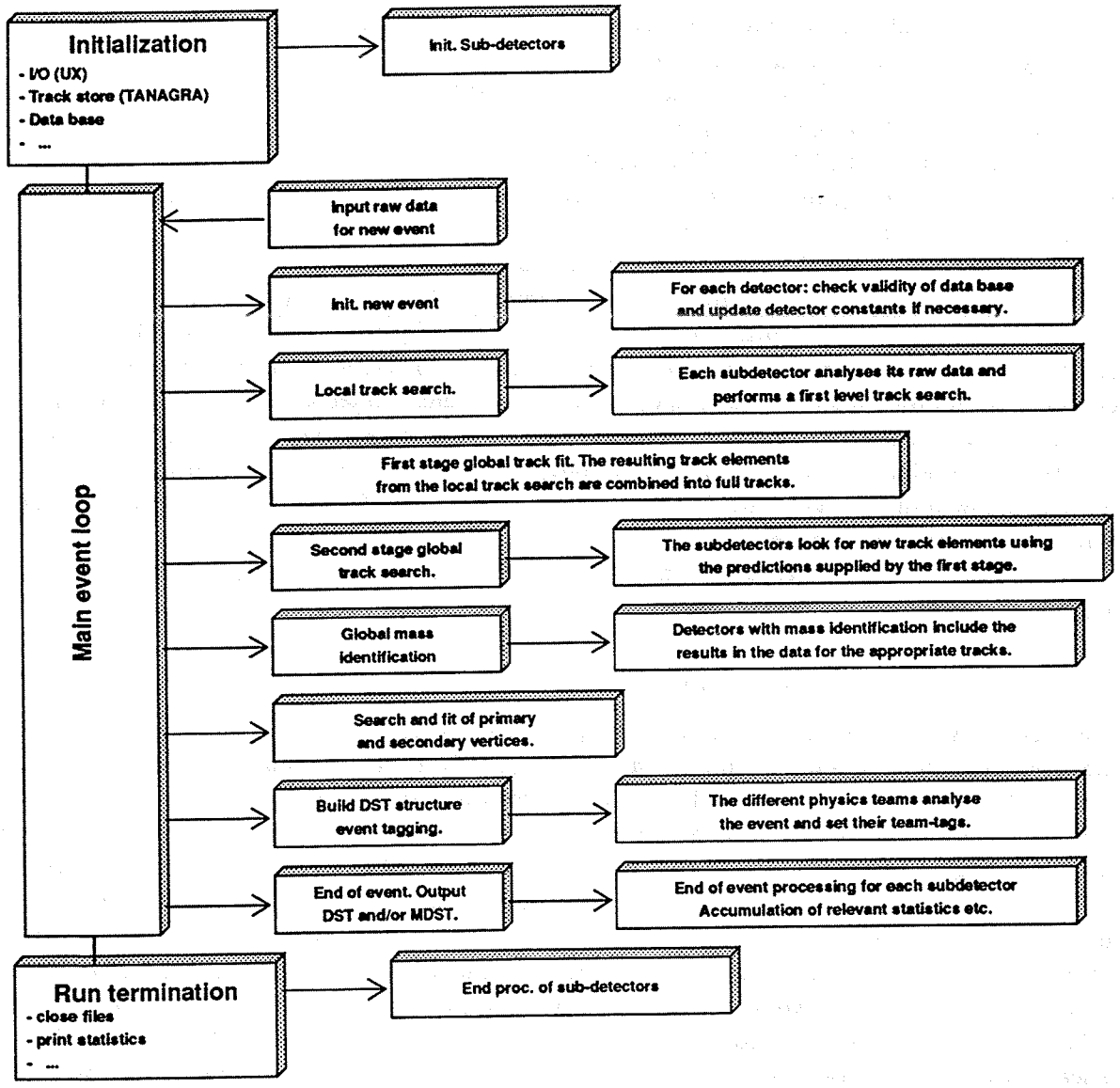

Figure 1.4: The processing stages of DELANA.

Track Elements in TANAGRA (TE) banks. Observe that this process is strictly local; the subdetector modules do not access the information of the others.

A global track search combines the TE informations from the different detector components into candidate **Track Strings** (TS). The full track fit solves the ambiguities and contradictions allowed at the TS level. The resulting tracks (TANAGRA TK banks), extrapolated through the detector, give the impact points and track parameters at the entry of each subdetector as input to the second stage processing. A new local pattern recognition starts for the tracking chambers, using the TK information from the first level track fit. If the detector module finds a new track element which belongs to an extrapolated track, this track is rebuilt and refitted. All newly found tracks are added to the TK banks.

A vertex search **Bundles** the tracks into TANAGRA TB banks that are used by the global vertex fit to build **Vertex** (TV) banks. The TV banks completes the TANAGRA hierarchy of total six levels: TD, TE, TS, TK, TB and TV. Links between the different levels assure a full recovery of the tracking; for a given TV one can always go back in the hierarchy and find out which TDs it is made of and vice versa.

A special package, which may as well run in stand alone, builds up the Data Summary Tapes (DSTs) that contains only the data which is normally relevant for the physicists, e.g. particle vectors, some calorimetry information etc. The different physics teams (Z^0 line shape, particle searches etc.) provide code to analyse the event; if certain criterias on for instance the event topology, are fulfilled a special team flag is set in the event header to facilitate future analysis.

Finally the event is written to the output medium (disk or tape). Normally only the DST is written. The Master DST (MDST), containing raw+TANAGRA+DST data, is usually only written for low multiplicity events like leptonic candidates and for selected two prongs for alignment and calibration purposes.

In 1989 the DST data fitted into three 200 Mbyte IBM 3480 cassettes, in 1990 and 1991 the number of cassettes were 38 and 146 respectively.

1.4.3 Interactive data analysis

The **Physics Analysis Workstation**, PAW [15], is a CERN written system for interactive analysis and presentation of data. It runs as a command driven stand alone program, where each command is associated to a procedure entry point via a special *Command Definition File* at creation time. Thus, it is a simple task to add new commands for specific applications such as the reading and analysis of DELPHI data. Intrinsically PAW already contains a concept for DST data analysis called Ntuple, which is basically a two dimensional array where one entry corresponds to a specific event and the other to the data of that event, e.g. run/event number, total multiplicity and energy, the 4-momentum of all particles, etc. A Ntuple can be regarded as a micro-DST. There are two problems with this concept: firstly in order to be accessable from PAW the Ntuple needs to be stored on a direct access file, which is limited by the available disk space and working quotas. Secondly, it is difficult to logically structure the data on the Ntuple, e.g. it would be preferable to have links between the particles belonging to the same vertex or the same jet. For those reasons a small DELPHI extension to PAW was written in 1989 and has since then been used by members of the Lund group in DELPHI. The data analysis presented in Chapter 3 has been carried out solely using this tool.

In its simplest implementation two basic commands are needed: one for connecting to a DELPHI data file and another for reading the data from the file into the program memory. The actual data analysis takes place in user written FORTRAN routines which are interpreted by the *COMpilation and Interpretation System* COMIS [15]. As interpretation, contrary to re-compilation and linking, allows an online development of the code, this concept becomes

quite powerful, for instance when tuning cuts. An important feature of the COMIS interpreter is the possibility of a controled access to the data and program sections of the loaded image (in this case PAW). In principle a COMIS interpreted routine can access any COMMON field, subroutine or function linked to PAW[2], which is essentially the whole CERNLIB and, in our case, also most of the DELPHI offline libraries.

Evidently an interpreter becomes slow as the code grows in size. At a certain point, usually when the user routines contains a couple of hundred lines, it is preferable to compile and link to PAW the part of the code that can be regarded as stable. In this way, analysis programs of arbitrary complexity can be built up with a minimal amount of effort. Once the user decides the code to be finished he compiles and links it with a small steering program, which will run the analysis in batch.

1.5 The tagging of anomalous charged particles

Confinement is an important but so far not proven feature of *Quantum Chromo Dynamics*, QCD. The potential between two colour charges is believed to include a linear confinement term that prohibit the existence of free partons (quarks and gluons). As this is a large distance phenomena ($\Leftrightarrow$ low energy, $Q \lesssim 1$ GeV) the running coupling constant, α_s, becomes strong and perturbation theory breaks down. Though so far no free quarks (or gluons) have been seen and most people believe in confinement the search for such signals must continue. Consequently, a DELPHI physics team for anomalous charged particle search was formed in late 1989. Unfortunately the attendance at the group meetings has since then steadily decreased and the group is today with its two members (the group leader and the author of this thesis) probably the smallest in DELPHI.

1.5.1 Method

The problem with searching for a free quark is the difficulty to imagine its interaction with the material in the detector. As a first attempt one may assume that the quark traverses the whole detector, or at least the tracking chambers, without being absorbed. The quarks, carrying an electric charge of either $\pm 1/3$ or $\pm 2/3$ of the electron charge, would in that case give an anomalous ionization in the TPC. From the theory of ionization energy loss, see Chapter 2, it follows that the probability for a collision of a given energy transfer from the incoming particle to an electron in the gas is proportional to the square of the charge of the particle. Thus, a 2/3 charged quark in the TPC would induce an ionization of 4/9 times that of a unit charged particle. The ionization from a 1/3 charged quark would probably be too low to be be seen at all in the TPC. However, one can still expect a signal in the streamer tubes of the Outer Detector (OD).

Another effect connected to the charge of the quarks is the mismeasured momentum. The radius of the projection of the helix is proportional to $|\mathbf{p}|/q$. Since unit charge is always assumed by the track fit in DELANA the momentum of a 2/3 charged quark will be overestimated by a factor 3/2. Knowing that a particle in DELPHI never can take more than the beam energy (~ 46 GeV), all tracks with higher momentum must either be badly reconstructed (most likely) or free quarks.

[2] All external references must however be specially declared to COMIS at creation time.

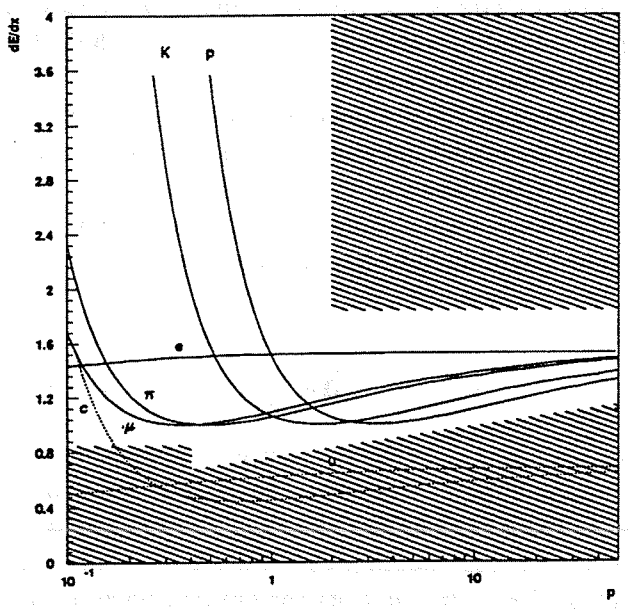

Figure 1.5: Mean energy-loss (80% truncation) versus momentum for the DELPHI TPC. The distributions are normalized to one for a minimum ionizing unit charged particle. Marked as shaded regions are the cuts discussed in the text. The dotted lines shows the expected signals from the 2/3 charged quarks: up (u) and charm (c).

1.5.2 Implementation

The search for the specific effects discussed in section 1.5.1 has been implemented as three separate tags in the tagging code of the *anomalous charge team.* In addition there is a fourth tag based on an unusual event topology rather than any particular effect due to the anomalous charge of the quarks. Both the TANAGRA and the DST data structures, see section 1.4.2, are used.

Tag 1: Detecting 2/3 charged quarks in the TPC. The track elements (TEs) of the TPC coming from the primary vertex ($R_{impact} \leq 5$ cm and $Z_{impact} \leq 10$ cm) and with $|p| \geq 0.5$ GeV/c are searched for anomalous ionization (dE/dx). The following criterias are defined:

$$\frac{dE}{dx} < (0.22 \log_{10} p + 0.76) \times \frac{dE}{dx}(min) \qquad \text{if } \log_{10} p \geq 0.4 \quad \text{or} \tag{1.1}$$

$$\frac{dE}{dx} < 0.85 \times \frac{dE}{dx}(min) \qquad \text{if } \log_{10} p < 0.4 \tag{1.2}$$

where p is the particle momentum in GeV/c and $\frac{dE}{dx}(min)$ is the minimum ionization (normalized to one in the TPC TE data). This tag also signals unusually high dE/dx corresponding to e.g. exotic 4/3 charged mesons like $|uu\rangle$ or four quark baryons. The criteria is then:

$$\frac{dE}{dx} > 1.83 \times \frac{dE}{dx}(min) \; for \; p > 2.0 \; GeV/c \tag{1.3}$$

Figure 1.5 shows a dE/dx plot from the TPC with the defined cuts marked as shaded regions.

Tag 2: Particles with large measured momentum. This tag is quite straight forward: an event is tagged if it contains at least one particle with more than 60 GeV/c momentum or two particles with a momentum of at least 50 GeV/c each. The tracks are required to be in barrel, $40° < \Theta < 140°$, for a reliable momentum measurement.

Tag 3: Search for 1/3 charged particles. This is the most involved of the four criterias; looking for an Outer Detector (OD) TE that is unassociated to a TPC TE via track strings (TS) or fitted tracks (TK). Remember from section 1.5.1 that a 1/3 charge particle will not be seen in the TPC, whereas the OD, working in *limited streamer mode* rather than in *proportional mode* as the TPC, would probably still react.

TANAGRA (see section 1.4.2) stores the full tracking history, i.e. it keeps links between all the information used to built up a track. For instance an OD TE has a link to the fitted track it is used in (if it is used) and that track has in turn links back to its constituents, the OD TE and may also be a TPC TE. The OD TE is associated to a TPC TE if they both belong to the same track or track string.

In order to reduce the cosmic radiation background in the z-region not covered by the TPC (see Figure 1.1), the OD TE is rejected if $R_{OD}|\sin(\Phi_{OD} - \phi_{OD})| \leq 40$ cm, where ϕ_{OD} is the direction of the momentum vector and Φ_{OD} the direction of the point where the momentum vector is defined (reference point of the OD TE). There is no cut on the impact in z since p_z is not always measured.

Possible fake-signals due to noise in the OD are reduced by requiring the candidate to be accompanied by at most two tracks in the same z-hemisphere. The event must not be empty, i.e. there should be at least one track or one back-to-back OD TE candidate in the opposite z-hempispere. A typical signal would be an isolated OD TE candidate due to the free 1/3 charged quark and a jet induced by nuclear interaction of the other quark with the detector material.

Tag 4 and 5: Search for free quarks in the $b\bar{b}$ and $c\bar{c}$ channels. We study the decays sketched in Figure 1.6. The s/d and $\bar{s}/\bar{d}$ are assumed to be free. The two weak decays (only one for the $c\bar{c}$) in one branch are assumed to be semi-leptonic. The other hemisphere may either contain also a semi-leptonic decay or a hadronic decay with at least one jet. This results in a quite unusual event topology, e.g. for $b\bar{b}$ there should be two opposite signed leptons and at most one other track from the free quark in one hemisphere and either a similar signal or at least one jet in the other hemisphere.

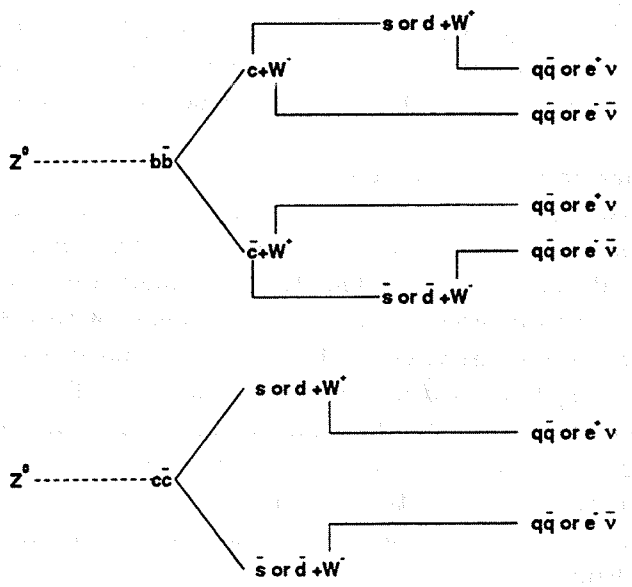

Figure 1.6: The two heavy quark decay channels to be tagged by tag 4 and 5. The s/d and $\bar{s}/\bar{d}$ are assumed to be free.

Chapter 2

Ionization Energy Loss

This chapter is based on the work presented in reference [16]. Considering the brevity of that paper the intention here is to give an introduction for non-experts.

Ionization energy loss, commonly refered to as dE/dx, is the process where an incoming charged particle looses energy in electro-magnetic interaction with the bound atomic electrons of the medium it traverses. An approximation used throughout the text is that the kinetic energy, E, of the particle can be considered unchanged in the process, i.e. the energy-loss Δ is much smaller than E. Only the atomic electrons are assumed to be responsible for the energy loss; interactions with the nuclei are ignored. Those assumptions are valid for high energy particles traversing a low density gaseous medium as is the case for the DELPHI TPC.

In the next section it will be shown how the theory of dE/dx may be separated into two parts: calculation of the *collision cross section differential in energy*, $d\sigma/dE$, and the *convolution*. In the following two sections each part will be treated separately. Finally, the calculations are compared with data from the DELPHI TPC.

2.1 Basic theory

Consider a charged particle traversing a volume filled with, for instance, argon gas. The situation is depicted in Figure 2.1. The moving charge interacts with the bound electrons in the gas molecules. It may be head-on inelastic collisions involving relatively high energy transfers or softer elastic collisions where the energy transfer is comparable with the atomic binding energy. For each collision involving an energy transfer larger than the ionization potential of the medium, at least one electron will leave the atom and an ion-pair is produced. This is called the primary ionization. A secondary ionization is induced if the released electron has sufficient energy to produce new ion-pairs through the same mechanism.

In total, the induced ionization in the volume can be expected to depend on the total number of collisions and the energy transfer in each collision. Thus, in order to calculate the total ionization, two operations are required. Firstly the probability of having a collision with a given energy transfer must be determined. Secondly, the energy transfer in individual collisions should be added up giving the total energy-loss in the volume.

The first points corresponds to calculating the single collision cross section differential in energy. The second point corresponds to a convolution which becomes evident from the following reasoning: let $P(\Delta)d\Delta$ be the probability that a single collision involves an energy transfer between Δ and $\Delta + d\Delta$. Then the probability of having two collisions within the same distance

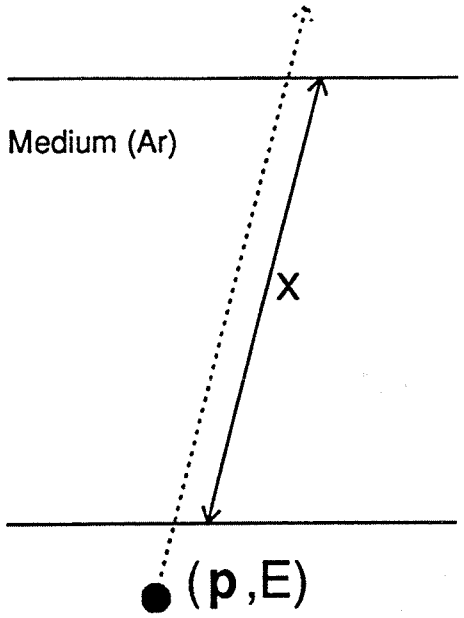

Figure 2.1: A particle with initial 4-momentum $(\mathbf{p}, E)$ travelling a distance x in a gas volume.

is given by:

$$P(\Delta)^{*2}d\Delta = \int_0^\Delta P(E)P(\Delta - E)\,dE\;d\Delta \tag{2.1}$$

The convolution integral sums over all possible combinations of two energy transfers adding up to a total energy $= \Delta$. Similarly the probability for n collisions with a total energy transfer in $[\Delta, \Delta + d\Delta]$ is given by the n-fold convolution:

$$P(\Delta)^{*n}d\Delta = \int_0^\Delta P(E)P(\Delta - E)^{*(n-1)}\,dE\;d\Delta \tag{2.2}$$

$$\text{where} \quad P(\Delta)^{*0} \equiv \delta(\Delta)$$

Finally, assuming successive collisions to be independent, the total number of collisions, n, over a distance x is described by the Poisson distribution:

$$p(n) = \frac{(x\bar{N})^n}{n!}e^{-x\bar{N}} \tag{2.3}$$

where $\bar{N}$ is the average number of collisions per unit distance. Combining (2.2) and (2.3) we get the probability density for the energy-loss over a finite distance x,

$$f(x,\Delta) = \sum_{n=0}^{\infty} \frac{(x\bar{N})^n}{n!}e^{-x\bar{N}}P(\Delta)^{*n} \tag{2.4}$$

2.2 The single collision cross section, $d\sigma/dE$

As pointed out in the preceding section there are two categories of collisions: the short distance Coulomb scattering where the energy transfer is much larger than the atomic binding energy

and the electron can be regarded as essentially free. Consequently one talks about the *quasi-free* region. The second type, the *resonance* regime, is the long distance low energy transfer where the particle interacts with the atom as a whole rather than individual electrons. The excitation of the atom results in photon emission or ionization.

Clearly the second category is by far the most difficult to calculate. In the limit a complete quantum mechanical description of the atom is required, which of course would only be possible for the quite uninteresting case of atomic hydrogen. In the first quantum mechanical treatment of the problem, Bethe and Bloch in the early 1930s used first order perturbation theory to calculate the transition probabilities. The incident particle was approximated by a plane wave. Their result for the average energy-loss of a heavy, spin 0 incident particle can be written

$$\langle \frac{dE}{dx} \rangle = D_e \left(\frac{Z}{\beta}\right)^2 n_e \left\{ \ln \frac{2m_e c^2 \beta^2 \gamma^2}{I} - \beta^2 \right\} \tag{2.5}$$

where $D_e = 4\pi e^4/(m_e c^2) = 5.0989 \times 10^{-25}$ MeVcm^2, n_e is the number of electrons per unit volume and I is the mean ionization potential of the medium. Ze is the charge of the incident particle and $\beta = v/c$ its velocity ($\gamma = 1/\sqrt{1-\beta^2}$). The formula (2.5) was later modified by Fermi for the dielectric screening between the atoms at large distance collisions. This phenomenon, known as the *density* effect, is the origin of the famous Fermi plateau.

Though the energy-loss is most naturally described in QED, it may as well to a large extent be derived from a semi-classical treatment. In that approach, which will be outlined below, all necessary information regarding the actual shell structure of the atoms etc. is contained in a single function, the dielectricity function ϵ. The determination of ϵ would then be derived from quantum mechanics and/or measurements of material properties of the medium.

The average energy-loss per unit distance $\langle \frac{dE}{dx} \rangle$ is simply the change in the particles' kinetic energy due to its own electromagnetic field

$$\langle \frac{dE}{dx} \rangle = F_\beta(t) = q\mathcal{E}(\beta ct, t) \cdot \beta/\beta \tag{2.6}$$

where $F_\beta(t)$ is the work of the electric field $\mathcal{E}$ on the particle itself, which is situated at $(\mathbf{r}, t) = (\beta ct, t)$. βc and q are the particles' velocity and charge respectively. Unfortunately, knowing $\langle \frac{dE}{dx} \rangle$ is usually not sufficient. The wanted quantity is rather the full probability density function $f(x, \Delta)$ describing the fluctuations of the energy loss Δ around the average value $\langle \Delta \rangle = -\langle \frac{dE}{dx} \rangle$. Note the sign convention: $\langle \frac{dE}{dx} \rangle$ is the energy change (≤ 0) of the particle whereas $\langle \Delta \rangle$ is the energy deposited (≥ 0) in the medium. As shown in the preceding section $f(x, \Delta)$ can be calculated provided the single collision cross section $\frac{d\sigma}{dE}$ is known. The two quantities $\langle \frac{dE}{dx} \rangle$ and $\frac{d\sigma}{dE}$ are realted through

$$\langle \frac{dE}{dx} \rangle = -\langle \Delta \rangle = -n_e \int_0^\infty E \frac{d\sigma}{dE}(E)\, dE \tag{2.7}$$

The idea is now to express the electric field in phase coordinates,

$$\mathcal{E}(\mathbf{r}, t) = \int_{\mathbb{R}^4} d^3k\, d\omega\, e^{-i(\mathbf{k}\cdot\mathbf{r} - \omega t)} \widehat{\mathcal{E}}(\mathbf{k}, \omega) \tag{2.8}$$

and reinterpret it, as in semiclassical radiation theory, as an integral over energy-momentum transfer, $\hbar(\mathbf{k}, \omega) = (\mathbf{p}, E)$, i.e.,

$$\langle \frac{dE}{dx} \rangle = \int_{-\infty}^\infty \left\{ \int_{\mathbb{R}^3} e^{-i(\mathbf{p}\cdot\mathbf{r} - Et)/\hbar} q\widehat{\mathcal{E}}(\mathbf{p}/\hbar, E/\hbar) \cdot \beta/\beta \frac{d^3p}{\hbar} \right\} \frac{dE}{\hbar} \tag{2.9}$$

With certain symmetry considerations discussed below, the limits for the integration over E can be changed to $[0,\infty[$ as in (2.7) and $d\sigma/dE$ can be identified by comparing the integrands.

It remains to determine the classical electric field $\mathcal{E}(\mathbf{r},t)$ (or rather its Fourier transform), by solving Maxwell's equations in the medium.

Let Φ and $\mathcal{A}$ be the electrostatic and magnetic vector potentials respectively. Choosing a gauge where $\nabla\cdot\mathcal{A}=0$ the Maxwell's equations are,

$$\triangle\Phi(\mathbf{r},t)=\frac{1}{\epsilon\epsilon_0}\rho(\mathbf{r},t) \tag{2.10}$$

$$(\epsilon_0c^2\triangle-\epsilon\epsilon_0\frac{\partial^2}{\partial t^2})\mathcal{A}(\mathbf{r},t)-\epsilon\epsilon_0\frac{\partial}{\partial t}\nabla\Phi(\mathbf{r},t)=-\jmath(\mathbf{r},t) \tag{2.11}$$

the moving charge represents a charge density $\rho(\mathbf{r},t)=q\delta^3(\mathbf{r}-\beta ct)$ and a current density $\jmath(\mathbf{r},t)=\beta c\rho(\mathbf{r},t)$. Applying the Fourier transform(2.8),

$$-k^2\widehat{\Phi}(\mathbf{k},\omega)=\frac{q}{2\pi\epsilon\epsilon_0}\delta(\omega-\mathbf{k}\cdot\beta c) \tag{2.12}$$

$$(-\epsilon_0c^2k^2+\epsilon\epsilon_0\omega^2)\widehat{\mathcal{A}}(\mathbf{k},\omega)-\epsilon\epsilon_0\omega\mathbf{k}\widehat{\Phi}(\mathbf{k},\omega)=-\beta\frac{qc}{2\pi}\delta(\omega-\mathbf{k}\cdot\beta c) \tag{2.13}$$

or

$$\widehat{\Phi}(\mathbf{k},\omega)=\frac{q}{2\pi\epsilon\epsilon_0k^2}\delta(\omega-\mathbf{k}\cdot\beta c) \tag{2.14}$$

$$\widehat{\mathcal{A}}(\mathbf{k},\omega)=\frac{q}{2\pi}\frac{\epsilon\epsilon_0\omega\mathbf{k}/k^2-\beta c}{\epsilon\epsilon_0\omega^2-\epsilon_0c^2k^2}\delta(\omega-\mathbf{k}\cdot\beta c) \tag{2.15}$$

The electrostatic field $\mathcal{E}(\mathbf{r},t)$ is given by Φ and $\mathcal{A}$ through $\mathcal{E}=-\nabla\Phi-\partial\mathcal{A}/\partial t$ and hence:

$$\mathcal{E}(\mathbf{r},t)=\frac{iq}{(2\pi)^3}\int_{-\infty}^{\infty}d\omega\int_{\Re^3}d^3k\left(\omega\frac{\epsilon\epsilon_0\omega\mathbf{k}/k^2-\beta c}{\epsilon\epsilon_0\omega^2-\epsilon_0c^2k^2}-\frac{\mathbf{k}}{\epsilon\epsilon_0k^2}\right)\delta(\omega-\mathbf{k}\cdot\beta c)e^{i(\mathbf{k}\cdot\mathbf{r}-\omega t)} \tag{2.16}$$

Assuming the medium to be isotropic the dielectric function has only radial k-dependence, $\epsilon(\mathbf{k},\omega)=\epsilon(k,\omega)$, and the angular integration in (2.16) can be performed. Further more general symmetry properties of the real and imaginary parts of ϵ are:

$$\Re(\epsilon)=\epsilon_1(\mathbf{k},-\omega)=\epsilon_1(\mathbf{k},\omega) \tag{2.17}$$

$$\Im(\epsilon)=\epsilon_2(\mathbf{k},-\omega)=-\epsilon_2(\mathbf{k},\omega) \tag{2.18}$$

and only the imaginary part of the integrand in (2.16) will survive[1]. After some algebra one gets:

$$\langle\frac{dE}{dx}\rangle=-2\frac{q^2}{(2\pi)^2\epsilon_0\beta^2}\int_0^{\infty}d\omega\int_{\omega/\beta c}^{\infty}dk\left(\omega k\left(\frac{\omega^2}{k^2c^2}-\beta^2\right)\times\Im\left(\frac{1}{\epsilon\omega^2-k^2c^2}\right)-\frac{\omega}{kc^2}\Im\left(\frac{1}{\epsilon}\right)\right) \tag{2.19}$$

where the lower limit of the k-integration is given by energy-momentum conservation in the soft collision approximation, $\omega=c\mathbf{k}\cdot\beta=ck\beta\cos(\mathbf{k},\beta)\Rightarrow k\geq\omega/(\beta c)$.

[1]This is evident already from the presence of the factor "i" in (2.16) since $\langle\frac{dE}{dx}\rangle$ must be a real quantity.

Finally, comparing (2.19) with (2.7) we identify $\frac{d\sigma}{dE}$. As already stated, all quantum mechanical complications are collected in the function ϵ which in turn is given by the generalized *oscillator strength* density $\vartheta(\mathbf{k},\omega)$,

$$\Im(\epsilon) = \epsilon_2 = \frac{\pi n_e e^2}{2m_e\omega}\vartheta(\mathbf{k},\omega) \tag{2.20}$$

$$\vartheta(\mathbf{k},\omega) = \frac{1}{Z_a}\sum_n \frac{2m_e(E_n - E_0)}{\hbar^2 k^2}\delta\left(\omega - \frac{E_n - E_0}{\hbar}\right)\left|\langle n|\sum_{j=1}^{Z_a} e^{i\mathbf{k}\cdot\mathbf{r}_j}|0\rangle\right|^2 \tag{2.21}$$

Z_a is the atomic number, and n runs through all possible quantum states. In the dipole approximation, $e^{i\mathbf{k}\cdot\mathbf{r}_j} \approx 1 + \mathbf{k}\cdot\mathbf{r}$, ϑ is independent of k and the ω-dependence is given by the atomic photoabsorption cross section $\sigma_\gamma(\omega)$. Performing the k integration in (2.19) we finally get

$$\begin{aligned}\frac{d\sigma}{dE}(\Delta) = \frac{\alpha}{\pi\beta^2}\Bigg\{&\frac{\sigma_\gamma(\Delta)}{Z_a\Delta}\ln\left(\frac{2m_e\beta^2c^2}{\Delta\sqrt{(1-\beta^2\epsilon_1)^2+\beta^4\epsilon_2^2}}\right)\\ &+\frac{1}{\hbar c n_e}\left(\beta^2 - \frac{\epsilon_1}{|\epsilon|}\right)\arg\left(1-\beta^2\epsilon_1 + i\beta^2\epsilon_2\right) + \frac{1}{Z_a\Delta^2}\int_0^\Delta \sigma_\gamma(\Delta')\,d\Delta'\Bigg\}\end{aligned} \tag{2.22}$$

where ϵ_2 is is given by

$$\sigma_\gamma(\omega) \approx \frac{Z_a\omega}{cn_e}\epsilon_2(\omega) \tag{2.23}$$

and ϵ_1 is uniquely determined from ϵ_1 through the Kramer-Kronig relation. α is the fine structure constant $\approx 1/137$.

The photoabsorption cross section σ_γ is a frequently measured function in spectroscopy. For argon the tabulation from [17] is depicted in Figure 2.2.

2.3 The Convolution

The essence of the convolution has already been discussed in the introduction, section 2.1. It remains to examine how the theory applies in practice, in particular as this is the subject of reference [16]. To that extent an alternative formula to (2.4) for the energy-loss probability density is needed

$$f(x,\Delta) = \frac{1}{2\pi i}\int_{\sigma-i\infty}^{\sigma+i\infty}\exp\left\{s\Delta - xn_e\int_0^\infty\left(1-e^{-sE}\right)\frac{d\sigma}{dE}(E)\,dE\right\}ds \tag{2.24}$$

The derivation of (2.24), which originates from Landau [18], can be found in many papers, e.g. reference [16] and it will not be repeated here. Energy loss calculations with this formula are often refered to as being based on the Laplace transform method. In this context it is useful to note that there are actually *two* Laplace transforms. The term

$$\int_0^\infty e^{-sE}\frac{d\sigma}{dE}(E)\,dE \tag{2.25}$$

is a Laplace transform of $\frac{d\sigma}{dE}$ with respect to E but in the derivation of (2.24) it originates from a convolution of $f(x,\Delta)$ and $\frac{d\sigma}{dE}(\Delta)$ in the transport equation for $f(x,\Delta)$.

The two theoretical clarifications in reference [16] can be summarized as:

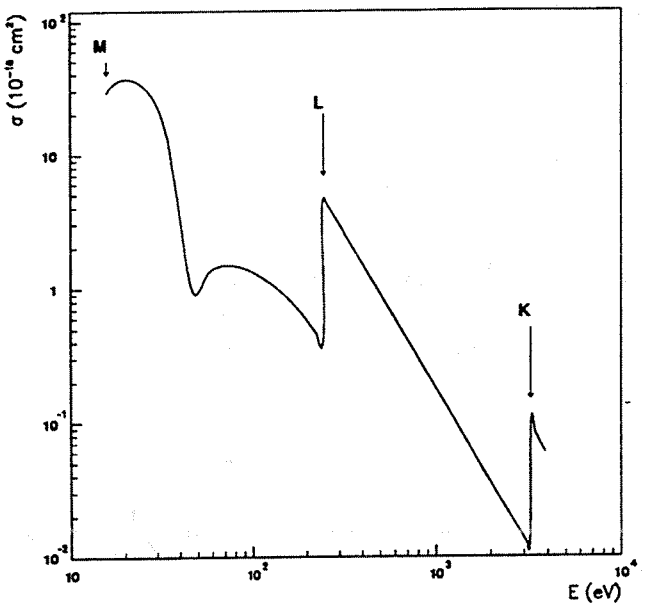

Figure 2.2: The photoabsorption cross section in argon.

- the observation of the presence of the second Laplace transform
- replacing the Laplace transforms with Fourier transforms which makes the expression suitable for numerical calculations.

Rearranging the terms in (2.24) a bit we get

$$f(x,\Delta) = C\mathcal{L}_s^{-1}\left\{\exp\left[xn_e\mathcal{L}_E\left(\frac{d\sigma}{dE}(E)\right)(s)\right]\right\}(\Delta) \tag{2.26}$$

$$C = \exp\left(-xn_e\int_0^\infty \frac{d\sigma}{dE}(E)\,dE\right) = \exp\left(-x(\bar{N})\right). \tag{2.27}$$

$\bar{N}$ is the mean number of collisions per unit distance, see section 2.1. The variable substitution $s \to \sigma + iy$ changes (2.26) into

$$f(x,\Delta) = D(\Delta)\mathcal{F}_y^{-1}\left\{\exp\left[xn_e\mathcal{F}_E\left(e^{-\sigma E}\,\frac{d\sigma}{dE}(E)\right)(y)\right]\right\}(\Delta) \tag{2.28}$$

$$D(\Delta) = \exp\left(\sigma\Delta - xn_e\int_0^\infty \frac{d\sigma}{dE}(E)\,dE\right) = \exp\left(\sigma\Delta - x(\bar{N})\right).$$

The small positive number σ, which defined the integration contour of the Laplace transform can in practice be set equal to zero and hence $D(\Delta) = C$ =constant.

The connection to the formula (2.4) derived in section 2.1 becomes transparent by considering

$$C\mathcal{F}_y^{-1}\left\{\exp\left[xn_e\mathcal{F}_E\left(\frac{d\sigma}{dE}(E)\right)(y)\right]\right\}(\Delta) = \left\{\mathcal{F}\left(\frac{d\sigma}{dE}\right) \equiv \widehat{\frac{d\sigma}{dE}}\right\} \tag{2.29}$$

$$= C\mathcal{F}_y^{-1}\left\{\sum_{n=0}^\infty \frac{1}{n!}\left(xn_e\widehat{\frac{d\sigma}{dE}}(y)\right)^n\right\}(\Delta) = C\sum_{n=0}^\infty \frac{(xn_e)^n}{n!}\left(\frac{d\sigma}{dE}\right)^{*n}$$

where the last step follows, somewhat handwaving, from repeated use of the convolution theorem for Fourier transforms

$$\mathcal{F}^{-1}\left(\hat{g}(y)\hat{g}(y)\right)(x) = \int_{-\infty}^{\infty} g(x-y)g(y)\,dy \equiv g(x)^{*2}. \tag{2.30}$$

Observe that in equation (2.4) the $P(\Delta)^{*n}$ functions are proper probability densities, i.e. normalized to unity, whereas in (2.29) the $\frac{d\sigma}{dE}(E)^{*n}$ are cross sections. Equality can be established by considering the conditional probability for a single collision; that is, given a collision what is the probability that the energy transfer was in $[\Delta, \Delta + d\Delta]$? The answer is given by the probability density

$$P(\Delta) = n_e \frac{d\sigma}{dE}(\Delta) \Big/ \left(n_e \int_0^{\infty} \frac{d\sigma}{dE}(E)\,dE\right) = n_e \frac{d\sigma}{dE}(\Delta) \Big/ \bar{N} \tag{2.31}$$

and similarly $P(\Delta)^{*2} = n_e^2 \frac{d\sigma}{dE}(\Delta)^{*2} \Big/ \bar{N}^2$ etc. Thus, equation (2.29) can be written

$$f(x,\Delta) = C \sum_{n=0}^{\infty} \frac{(x\bar{N})^n}{n!} \left(n_e \frac{d\sigma}{dE}(\Delta)^* \Big/ \bar{N}\right)^n = e^{-x\bar{N}} \sum_{0}^{\infty} \frac{(x\bar{N})^n}{n!} P(\Delta)^{*n} \tag{2.32}$$

whereby we have completely recovered equation (2.4).

The implementation of (2.28) with Fast Fourier Transform (FFT) routines in a computer program is straight forward; a program flow chart is given in reference [16]. The formula (2.28) provides a convenient way to smear the calculated energy-loss distribution since a convolution reduces to a simple multiplication of Fourier transforms. There are then two levels where the smearing can be introduced:

$$\begin{aligned} \tilde{f}(x,\Delta) &= \int f(x,\Delta - E)g(E)\,dE \\ &= C\mathcal{F}_y^{-1}\left\{\hat{g}(y)\exp\left[\mathcal{F}_E\left(xn_e\frac{d\sigma}{dE}(E)\right)(y)\right]\right\}(\Delta) \end{aligned} \tag{2.33}$$

or

$$\tilde{f}(x,\Delta) = C\mathcal{F}_y^{-1}\left\{\exp\left[\hat{g}(y)\mathcal{F}_E\left(xn_e\frac{d\sigma}{dE}(E)\right)(y)\right]\right\}(\Delta) \tag{2.34}$$

In (2.33) the energy-loss distribution itself is smeared with a function $g(\Delta)$. It could for instance correspond to avalanche fluctuations or electronic noise. The second case is a smearing of the single collision cross section $\frac{d\sigma}{dE}$, which may be harder to relate to reality and therefore is of limited use. If $g(\Delta)$ is a Gaussian the calculation becomes particularly easy as its Fourier transform is known analytically.

As with most numerical calculations there are certain limitations with the method outlined in this section. Firstly, the exponential factor in (2.28) becomes big for small β due to the $1/\beta^2$ behaviour in $\frac{d\sigma}{dE}$, see (2.22). For $\beta\gamma \lesssim 0.3$ the calculation breaks down on most machines. Fortunately this region is usually not very interesting since such a high ionization would probably saturate the readout electronics. Secondly, as the infinite continuous Fourier transforms are approximated with finite discrete ones, peculiar edge effects may occur due to the periodic behaviour of the finite Fourier transform. In this case it is usually sufficient to expand the energy interval. A third problem, which is not connected to the method however, is the difficulty of doing accurate calculations for very thin samples (small x). This will be discussed in the next section.

2.4 Energy-loss calculations versus reality

The equations (2.22,2.28) together with the cross section in Figure 2.2 have been put into a computer program. The results from calculations with this program are shown in Figures 1 and 2 of reference [16]. Since then, the DELPHI TPC has been operating for more than three years and the program has been used in simulation and reconstruction of the TPC data during all that period. However, the reconstruction of the particle identity with $\frac{dE}{dx}$ has proven to be a much more difficult task than foreseen. The initial attempt to use the full measured energy-loss distribution and calculate the Kolmogorov distance to the theoretical curve, had to be abandoned. One reason is the structures appearing in the calculated distributions in Figure 2 of reference [16] which are not be visible in the data. Though this in principle can be corrected for by introducing a smearing as discussed in the end of section 2.3, there is still a need for major corrections to the data before any adequate measurement at all can be done. Therefore we decided, at least until all problems are understood, to use the simplest possible estimator, the *truncated mean*; the long tail of the distribution is cut off and only 80% of the lowest amplitudes are kept. For the remaining distribution, which can be roughly approximated by a Gaussian, the arithmetic mean is taken and compared with the corresponding quantity from the theoretical calculations.

A recent, quite extensive study [19] describes in detail all the corrections so far implemented in the reconstruction of the TPC data. A subsample of the corrections are:

- Track isolation. In hadronic events there are a high probability of having two or several tracks associated to the same wire clusters. Those clusters cannot be used in the dE/dx measurement.
- Gain variations in the chamber as a function of the distance to the sector edges. The response of a wire varies with the position on the wire where the avalanche took place.
- Gain variations with the gas pressure. A correction of more than 4% is needed for a 1% variation in the pressure.
- Charge accumulation. In high multiplicity (hadronic) events the wire response for a given cluster depends on the number of preceding clusters (the accumulated charge) on that wire. This effect is due to a 1% undershoot in the response function of the shaper, i.e. for each shaped pulse the zero level of the shaper becomes about 1% lower.

After all corrections the TPC gives a decent $\frac{dE}{dx}$ measurement which can be used for particle identification, though the efficiency is quite low; after the track isolation cut there remains only about 30-50% of the tracks with $p \in [2, 20]$ GeV/c. The Figures 2.3 and 2.4, which correspond to 6.1 and 6.9 in [19], show a comparison between the corrected data and the simulation. It should be stressed that the simulation contains more than just a simple smearing of the theoretical curve. For instance, the diffusion is dependent on the drift distance, which varies over a track.

The problem of calculating accurate $\frac{dE}{dx}$-distribution for thin layers is well known and is widely discussed in the literature [20]. As xP, where P is the pressure, becomes smaller the more important it is to have an adequate description of $\frac{d\sigma}{dE}$ and hence of the dielectricity function $\epsilon(\mathbf{k}, \omega)$. Indeed, in the limit $xP \to 0$ we are left with the single collision cross-section; keeping only up to first order x-terms in equation (2.28) $f(x, \Delta) \approx \delta(\Delta)(1 - x\bar{N}) + xn_e \frac{d\sigma}{dE}(\Delta)$. What usually is refered to as a *very thin* gas layer, $xP \simeq$1–10 cm atm, should be compared with the $xP \simeq$0.4–0.6 cm atm of the DELPHI TPC. It might then be justified to ask whether our $\epsilon(\mathbf{k}, \omega)$ is accurate enough. On the other hand, trying to improve ϵ by going to higher orders is not very appealing. An alternative solution, perfectly plausible and so far not totally excluded,

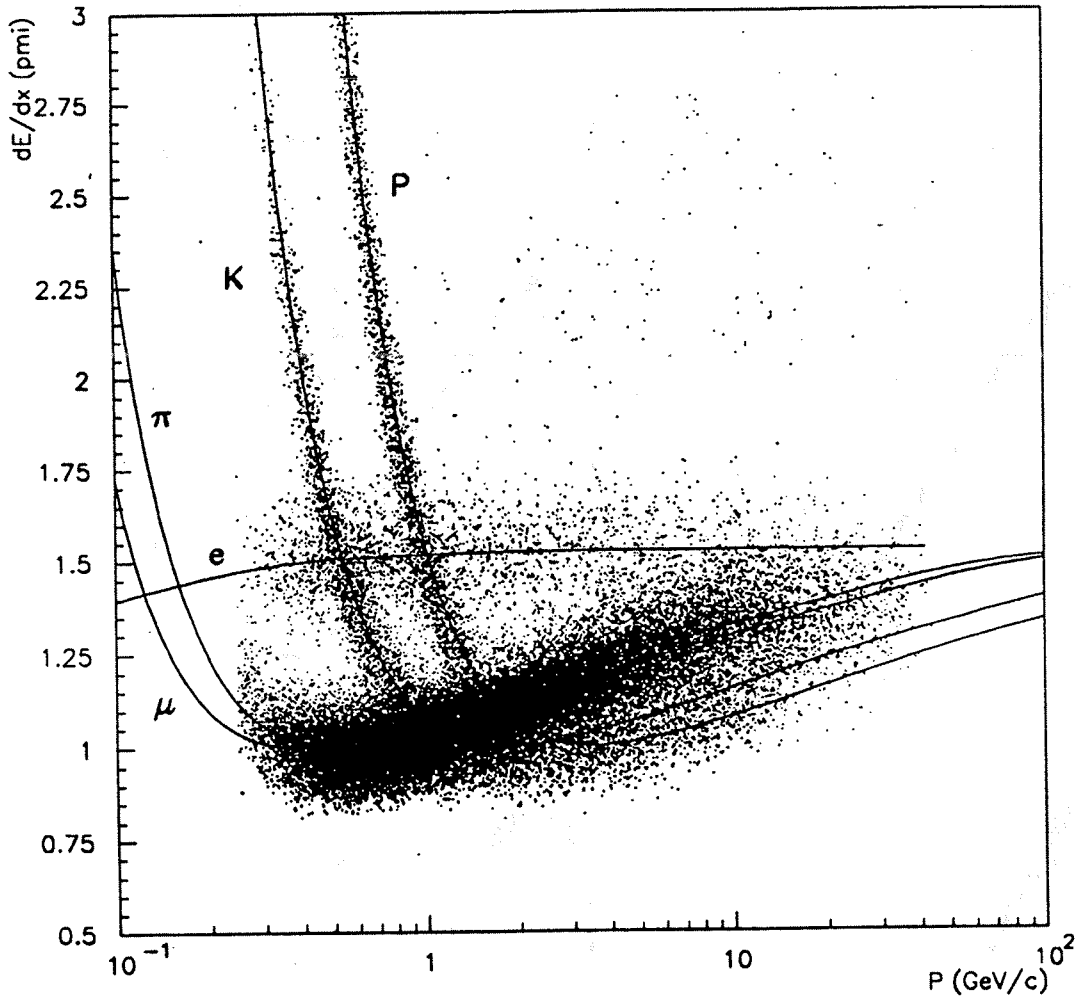

Figure 2.3: The Figure 6.1 in [19]. Truncated mean as function of the particle momentum. Only tracks with more than 135 samplings (wires) are used.

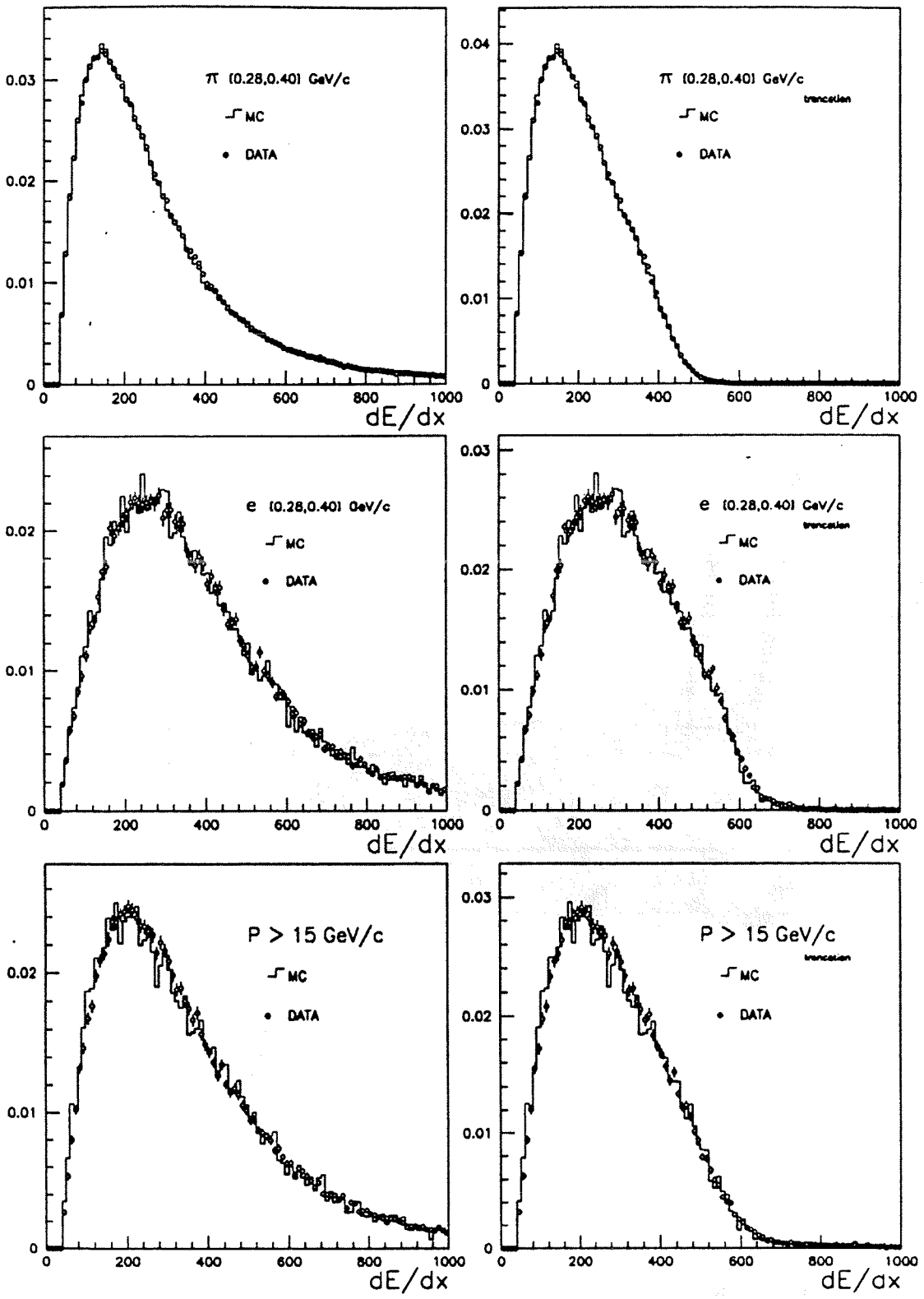

Figure 2.4: The Figure 6.9 in [19]. The full and truncated $\frac{dE}{dx}$ distribution for data and Monte-Carlo.

would be to invert the problem: given a very clean $\frac{dE}{dx}$ distribution extract $\epsilon(\omega)$ by inverting the equations (2.22,2.28). At LEP a clean energy-loss spectrum can be obtained from $Z^0 \rightarrow \mu^+\mu^-$ events. The most difficult step is to invert the equation (2.28), which turns out to be an ill defined numerical problem. It must probably be done analytically by choosing a suitable parametrization of the measured distribution. The inversion of (2.22) reduces to solving a first order highly non-linear differential equation, which can probably be done with some standard numerical method.

Chapter 3

Jet Identification and The Triple Gluon Vertex

The analysis presented in this chapter consists of two basically different parts: quark/gluon jet classification based on fragmentation differences and the measurement of the triple-gluon vertex. The latter, which is fully contained in the framework of [21, 22] apart from the jet identification, was presented as an addendum [23] to the DELPHI contribution [22] at the Dallas conference 1992. The jet classification has been presented in two separate DELPHI internal notes [24, 25] and it is used in [23].

The aim has been construct a jet identification, which, contrary to most other methods, does not use the jet energy, i.e. it is only sensitive to the fragmentation of the partons. Within this scope the non-perturbative phase of the jet evolution is used and the method is therefore suitable for measurements of perturbative effects like e.g. angular correlations between the jets. It should in this connection be emphasized that throughout this analysis the jet classification is only applied to one jet at the time; we never use information from the whole event. We decided to concentrate on angular correlations in four-jet events, primarily because one such study already had been successfully worked out at DELPHI using another jet identification but also because this is a domain where a better jet identification can highly improve the results.

After a short introduction to the physics, the jet identification method will be described. Then follows a discussion on the four-jet analysis in general and in particular how my jet identification is applied. Finally the preliminary results are presented together with a discussion on possible error sources introduced by the jet classification method and how those can be corrected for.

3.1 An Introduction to the Physics

The ruling theory in particle physics is suitably named the *Standard Model.* It emerges from the general idea that the interactions can be deduced from the invariance of the theory under a certain class of transformations, called local phase transformations. A *gauge* theory is a theory, which exhibit this property and correspondingly such a theory is *gauge invariant* with respect to the considered phase– or gauge transformation. The term gauge invariance stems originally from H.Weyl (or rather in the English translation of his German manuscript) who unsuccessfully tried to interpret the electromagnetic field as a consequence of invariance under local scale transformations. Later, in 1927 it was realized, amongst others by Weyl himself, that quantum electrodynamics (QED) is related to a symmetry in which the electron's wavefunction undergoes a local phase change. Thus, Weyl's original idea of invariance under local scale

transformations had become invariance under local phase transformations but the word *gauge* was retained. By *local* one means that the transformations are space-time dependent in contrary to *global* transformations where the phases are constant, independent of the space-time.

Among the four known fundamental forces in nature, three have been successfully included in the Standard Model. Those are, the weak, electromagnetic and strong interactions. So far all attempts to encompass the fourth interaction, the gravitation, have failed. The analysis described in the following sections is devoted to the measurement of two important parameters concerning the strong interaction or, more specifically, the corresponding gauge theory, *Quantum CromoDynamics* (QCD). In contrast to the gauge theory of the electromagnetic interaction, QED, perturbation theory is generally not applicable in QCD. Only in the high energy limit, where the quarks behave as essentially free, can the perturbative calculations be valid. In the other limit, where the quarks are confined into hadrons, only semi-empirical models exists.

The concepts of perturbative and non-perturbative QCD will be shortly discussed in the following two subsections. There is no pretension whatsoever that the presentation should be a complete review of QCD. The theory is far too involved and in fact only its general concepts are known to the author. Some salient aspects of QCD relevant for the forthcoming analysis are given and if appropriate, followed by a brief motivation. The last subsection outlines the theoretical incentive for analysing four-jet events.

3.1.1 Perturbative QCD

Principally one can distinguish between two fundamentally different perturbative approaches in QCD. One being the ordinary power expansion in terms of the coupling constant, α_s, characteristic for the theory. Currently such *matrix element* calculations only exist up to second order. The other method is a resummation of the power expansion taking only the leading and possibly next to leading terms in each order. The former has the advantage of containing all information in a given order. As we are interested in measuring angular correlations between the jets in four-jet events, the assumption that jets originate from hard partons in the final state of a Z^0 decay implies we should study four parton distributions. Thus, it appears sufficient to consider only second order (α_s^2) terms in the power expansion corresponding to the diagrams shown in Figure 3.1a. Unfortunately this argument does not hold in general due to the soft gluon radiation, which necessarily gives contributions in between the different orders of the power expansion. As the jet resolution parameter, y, decreases (finer resolution) soft gluons give rise to large logarithmic terms in each order of the power expansion. Consequently the truncated power expansion will suffer from large higher order corrections and the results will not be reliable.

In the second perturbation method above the leading logarithms are summed over to all orders whereas the subleading terms in each order are ignored. This is best picturized in the *Parton Shower* scheme, see Figure 3.1b. The parton showers evolve by an iterative use of the basic $q \to qg$, $g \to gg$ and $g \to q\bar{q}$ branchings determined by the Altarelli-Parisi equations. This procedure corresponds to a leading-log approximation, although subleading coherence effects and angular ordering usually are included in the existing implementations. Today, a main theoretical concern is to include the next to leading term in the summation. For some global event variables such calculations have already been successfully performed.

The dilemma of choosing perturbation method cannot generally be solved. It depends on the type of measurement performed. As for the study of four-jet events the opinion seems to be that the second order perturbation approach is the most appropriate [26]. One conclusion in [22] states indeed that the data is better described by the second order matrix element than the parton shower for the particular variables studied. Finally, an argument concerning

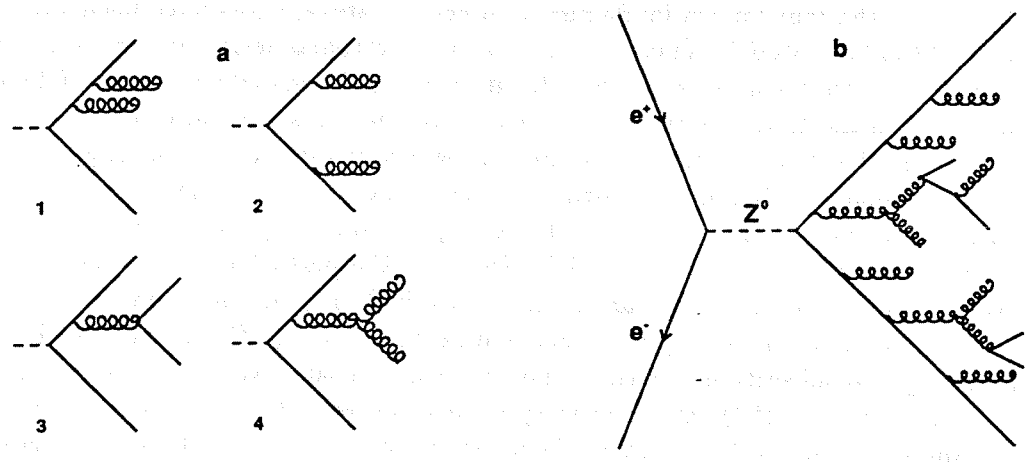

Figure 3.1: (a) The four parton final state in QCD. 1-2. Double bremsstrahlung, 3. Gluon splitting into two quarks, 4. The triple gluon vertex. (b) A parton shower. At LEP energies one can expect about 10 final partons.

the measurement of N_c/C_f and T_R/C_f in section 3.3: an ambiguity may arise in the parton shower when trying to classify a simulated event, e.g. Figure 3.1b, as one of the types shown in Figure 3.1a. It should be emphasized here that those are very subtle arguments; the parton shower method has been supremely successful in describing the data at LEP and lower energies, whereas the second order matrix element failed already at PETRA/PEP energies.

3.1.2 Fragmentation models

As pointed out already in the introduction, the fragmentation of the partons into final observable hadrons cannot be treated by perturbation calculations. The running coupling constant α_s becomes large at the low energies in question and the perturbative expansion in powers of α_s will not converge. Although methods have been proposed and are being developed for non-perturbative calculations, we will probably need to continue to rely on phenomenological models for a long while.

One particularly successful model is the Lund string fragmentation. Conceptually it is founded on a few consistency requirements on a cascade model for fragmentation. Its basic ingredient is that a massless relativistic string approximates the linear confining colour flux tube expected in QCD (already mentioned in section 1.5). The string is stretched between a quark and an antiquark which move apart with large energies. As the separation becomes large the string breaks and a new $q\bar{q}$-pair is created at the breaking point and this process continues iteratively as depicted in Figure 3.2a. Whenever a system breaks into two parts it is assumed that these will further fragment independently. Because the breakpoints are causally disconnected the time-ordering in the iterative procedure is Lorentz frame dependent with the consequence that all breakpoints must be treated equally. It should not matter from which vertex the production process is started. This "independence principle" puts an important constraint on the model. In [27] the independence principle together with an assumption, which implies a central rapidity plateau in the final meson spectrum, were sufficient to pinpoint the stochastic process

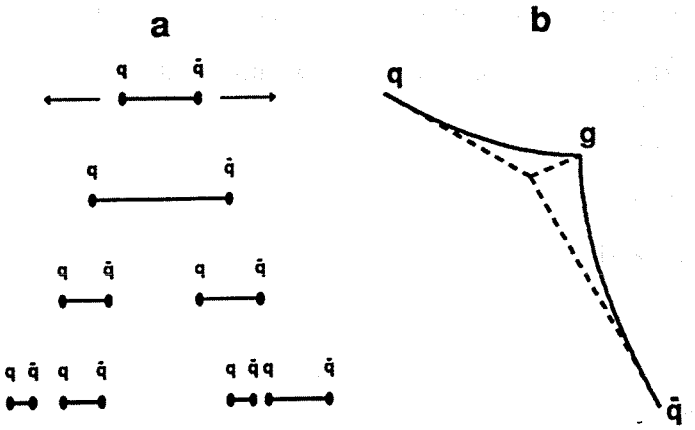

Figure 3.2: (a) A $q\bar{q}$ pair moving apart in the Lund string picture. When the string tension becomes too high the string breaks and two new $q\bar{q}$ systems are created. (b) The string arrangement in a $q\bar{q}g$ event.

governing the cascade. For the simplified case, with only one quark flavour, one type of meson and when the transverse dimension can be neglected, the model has only two free parameters.

The gluons are associated with energy and momentum carrying kinks on the string. Thus, in a $q\bar{q}g$ configuration the string is stretched from the q via the g to the $\bar{q}$ (or vice versa), see Figure 3.2b. With this arrangement there are string pieces qg and $g\bar{q}$ but none between the quark and the antiquark. After hadronization there will then be an enhancement of particles in the qg and $g\bar{q}$ regions compared to the $q\bar{q}$ region. This phenomenon is commonly refered to as the *string effect.*

3.1.3 Motivation for studying four-jet events

An important difference between the gauge theories for the electromagnetic interaction (QED) and the strong interaction (QCD) is that the former is *Abelian* whereas the latter is not. The very meaning of a group not being Abelian is that its elements do not commute, i.e. in the binary operation defined for the group the order of the elements is important. For instance, consider the group of 2×2 matrices with the binary operation defined as ordinary matrix multiplication, then in general $AB \neq BA$, where A and B are two elements in the group. In QCD the practical consequence of this abstraction is that the gluon field couples to itself whereas the photon field in QED does not; in addition to the "QED"-like graphs 1,2 and 3 in Figure 3.1a there exists in QCD a fourth graph, 4, which is absent in QED. We call this vertex, where a gluon radiates another gluon, the *triple-gluon* vertex. In addition there is a four gluon vertex, which does not concern us here.

Although there are many indirect evidences for the gluon self coupling, a measurement of its strength in the clean conditions of Z^0 multihadronic events constitutes an important test of QCD. In e^+e^- annihilation the triple-gluon vertex enters in second and higher orders of the strong coupling constant. The four parton final state has been calculated in order α_s^2 by Ellis, Ross and Terrano (ERT) [28]. Their result for $q\bar{q}gg$ falls into three classes:

A planar double-bremsstrahlung graphs with group weight C_F^2;

B non-planar double-bremsstrahlung graphs with group weight $C_F(C_F - \frac{1}{2}N_C)$;

C graphs involving the triple-gluon vertex with group weight $C_F N_C$;

and similarly for the $q\bar{q}q\bar{q}$:

D planar graphs with group weight $C_F T_R$;

E non-planar graphs with group weight $C_F(C_F - \frac{1}{2}N_C)$;

F graphs with group weight C_F;

C_F is the fermionic Casimir factor, N_C the number of colours and $T_R = \frac{1}{2}n_f$ where n_f is the number of quark flavours. In QCD their values are: $C_F = 4/3$, $N_C = 3$ and $T_R = 5/2$ (five flavours). The class F gives no contribution in an experiment where the charge of the partons is undetected [28].

Evidently it is the contribution of class C which distinguishes QCD from an Abelian theory and by measuring its group weight we can prove the existence of the triple-gluon vertex.

3.2 Jet Identification

Traditionally, whenever the knowledge whether a jet is of quark or gluon origin has been required, the jets in a multijet event have been classified according to their energy. A three jet event in an e^+e^- annihilation must contain two quark jets and one gluon jet. The gluon has been produced through bremsstrahlung from one of the quarks and has therefore most probably the smallest energy of the three jets. The QCD matrix element suppresses gluon jet production as $1/E_{gluon}$. Ordering the jets in energy gives a correct identification of the gluon and hence the whole event, with about 67% probability in detector simulated events [25] if both neutral and charged particles are used.

Methods have been proposed to improve the identification and in this section a new approach will be presented. It is based on a set of variables suggested in [29] but with the jet energy dependence divided out. Thus, the method is essentially complementary to the jet-energy classification.

The input to the method is a set of about ten variables and some means for pattern recognition in this multivariable space is needed. One suitable technique, *Artificial Neural Networks* (ANN), will be introduced in the first subsection. Then follows a presentation of the variables and finally the performance of the method will be summarized. As most of the material is already contained in [23, 24, 25] the presentation here will be kept quite short.

3.2.1 Feed Forward Artificial Neural Networks

The idea of using ANN for identifying jets in hadronic events was first raised by L.Lönnblad et al. [30]. Basically it constitutes a possible method for feature extraction in large variable spaces. There are other such methods, e.g. statistical discrimination, but these often have constrains on the distribution of the input variables for optimal performance. The ANN technique does not have any limitation in that sense; the input variables do not need to be Gaussian distributed nor does it matter if they are strongly correlated. The price for this "liberty" is that the user has no control over the process. The ANN detects correlations and anti-correlations

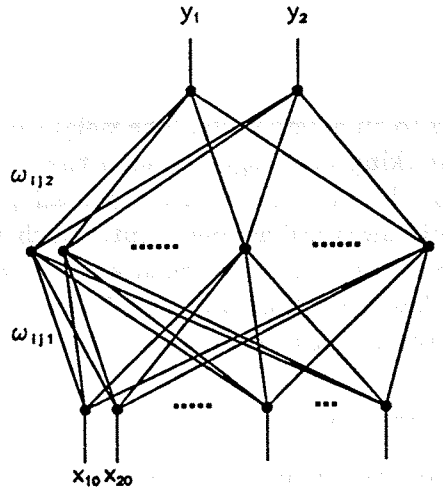

Figure 3.3: A feed forward ANN with one layer of hidden units.

among the variables and their linear and nonlinear combinations. Consequently it is in general impossible to reconstruct what the ANN actually does with the data – it works as a black box.

The feed forward ANN, which will be consider here, is a layered structure of interconnected nodes as depicted in Figure 3.3. Note that there are only connectors between the layers; there is no communication between the nodes in one layer. The information flow is unidirectional from the input layer foward through the network to the output layer; there is no feedback from higher (closer to output) to lower layers. The layers between the input and output layers are called *hidden*. To the connectors are associated weights, ω_{ijk}, which constitute the internal representation of the input patterns, or, more popularly, the memory of the ANN. The function of the nodes is to map nonlinearly the weighted total output from the preceding layer $(k-1)$ and feed it forward to the neurons in the next layer $(k+1)$, formally:

$$x_{jk} = f\Big(\sum_{i=1}^{N_{k-1}} \omega_{ij(k-1)} x_{i(k-1)}\Big) \tag{3.1}$$

where f is the nonlinear function, N_{k-1} is the number of nodes in layer $k-1$ and x_{jk} is the output of node j in layer k.

The *learning* of a feed forward ANN is a minimization process, with respect to the weights, of the distance between the network output, y_j, and the desired output, t_j, for a given input pattern, x_{i0}. The *back-propagation* algorithm is probably the most commonly known learning method. The distance measure is the error function,

$$E = \frac{1}{2}\sum_{j=1}^{N_m} (t_j - y_j)^2 \tag{3.2}$$

$$(y_j = x_{jm}) \tag{3.3}$$

where m refers to the output layer. The minimization is a recursive gradient descent starting from the output nodes and propagating backward through the network to the input layer. For more mathematical details refer to [31]

The implementation of a feed forward ANN with back-propagation learning does not require too much effort. A set of totally six FORTRAN-77 subroutines was written and the code amounts to a few hundred lines including the comments. The organization is according to the operations expected on an ANN: initialization, feed forward, back-propagation, change of weights, writing

and reading of the weight matrix to an external file. The weight matrix (ω_{ijk}), the network state matrix (x_{ik}) and an auxiliary working field together with the entry addresses for the function f and its derivative (needed for the gradient descent) are all passed as actual arguments in the call sequence. This seemingly awkward arrangement, which leads to quite long parameter lists, has the advantage of allowing for any network size and layout without changing the six basic routines. This would not had been the case if COMMON fields were used instead. The subroutine package is linked to the DELPHI extended PAW version described in section 1.4.3.

3.2.2 Jet Classification Variables

In [24] the input to the Artificial Neural Network, ANN, was the four-momentum vectors of the four leading charged particles in the jet. The fact that, among those rather raw and non-organized variables, the ANN was able to do a hard selection on the fragmentation function (see Figure 8 in the same reference) is a striking demonstration of its capabilities. The hard "cut" not allowing any jet containing particles with $z > 0.5$ ($z = p_L/p_{jet}$) to be identified as a gluon jet, can hardly be explained from energy selection alone. The ANN must have calculated some kind of jet-axis and projected the particles onto it. In one sense this subtle penetration of the given information is discouraging: it would be difficult hide the fragmentation information from the ANN. Therefore, all measurements of fragmentation effects like e.g. the *string effect* will be biased. On the other hand, if it would be possible to eliminate the jet energy dependence, the method is sensitive to the more intrinsic differences between quarks and gluons and not just the trivial fact that the gluon happens to be created in a radiation process whereas the quark is not.

Note, however, that the method used in [24] exaggerates the effects; we classified all jets within a certain distance from the two target values, 0 and 1, as being quark and gluon jets respectively. All jets that happened not to fall into any of those two regions were "undefined" and not used. Not surprisingly, such strong cuts on the ANN output show up as cuts on the input information. Nevertheless the study served an instructive purpose. In practice, the fact that exactly one of the jets in a three jet event has a gluon ancestor should be exploited by ordering the jets in ANN response just as in the energy ordering of the jets.

There are two ways to eliminate the jet energy dependence of the method: using input variables that can be proven to be independent of the jet energy or using a set of ANNs, each allocated to a specific energy interval. The former approach will be discussed here. The starting point is a set of moments suggested in [29]:

$$M_{nm}(E_j) = \sum \left(\frac{p_t}{E_j}\right)^n \eta^m \tag{3.4}$$

where the sum is taken over all particles assigned to the jet. p_t and η are the transverse momentum and pseudorapidity of the particle with respect to the jet-axis. E_j is the jet energy. By construction these moments are expected to be sensitive to the the softer fragmentation, higher multiplicity and broader transverse momentum of the gluon jets as compared to the quark jets. From a study of the 7×7 first moments M_{10}, M_{11}, M_{14}, M_{15}, M_{16}, M_{25}, M_{26} and M_{27} proved to give the best separation between quarks and gluons. The average jet energy (E_j) dependences of eight selected moments are shown in Figure 1 of [23, 25]. At least the first six of them exhibit a non-negligible energy dependence. Since the quarks (gluons) are more likely to populate the high (low) energy region in those moments we would still indirectly use the jet energy as a classifier. However, the average energy dependence might be divided out because the quark and gluon lines in each diagram are nearly parallel. Formally a new set of variables

is defined:

$$F_{nm}(E_j) = \frac{M_{nm}(E_j)}{\overline{M_{nm}(E_j)}} \tag{3.5}$$

The mean value indicated in the denominator is taken over all the jets with energy E_j. As expected the new variables F_{nm} show significantly less energy dependence than M_{nm}, see Figure 2 in [23, 25].

There is an appealing feature in the construction of F_{nm}; they measure only the relative behaviour of quarks and gluons in the moments M_{nm}. The dependences on the absolute values have been divided out by the normalization to $\overline{M_{nm}}$. Intuitively one would expect such variables to be less sensitive to systematic differences in the quantitative description of the fragmentation as long as the qualitative features, e.g. the gluon jets have higher multiplicity etc., are retained. Indeed, in [25] the jet classification proved to be rather insensitive to up to 50% variations in some of the fragmentation parameters of the Lund string fragmentation model.

3.2.3 Performance of the Jet Identification

A thorough comparison of the method presented in this section and the ordinary jet energy ordering can be found in [25]. One important change has been made since then which slightly disfavours the jet energy ordering; it is well known that angles of the jet-axis are in general better measured than the jet energies. Thus, combining the measured jet angles with the constraint of total four-momentum conservation $((\mathbf{p}_{tot}, E_{tot}) = (0, 0, 0, \sqrt{s}))$ a more reliable value on the jet energy can be calculated. For four-jet events this works fine as long as the events are non-planar. When all four jet-axes happen to be in the same plane only three of the four equations are linearly independent and the system is undefined. Another possibility is a large missing momentum, e.g. a fifth undetected jet in the extreme forward. In both those cases the constrained fit will give unphysical jet energies and in [25] such events were skipped. In order to avoid a bias in the four-jet event selection we do now use the measured jet energy instead.

In a four-jet $q\bar{q}gg$ event all four jets are correctly classified if, for instance, both the quark jets are found. By randomly picking two of the jets there is about 17% probability for success $(\frac{1}{2} \times \frac{1}{3} = \frac{1}{6} \approx 0.17)$. In detector simulated (see section 1.4.1) parton shower events the jet energy ordering gives the correct assignment in $\sim 37\%$ of the cases whereas the corresponding number for our best trained ANN is $\sim 46\%$. The results are summarized in table 3.1. Note, that if the neutral particles are not used, as is the case in [21, 22], the quoted value (37%) for the jet energy ordering will presumably decrease significantly.

3.3 Four jet analysis

In this section the four-jet analysis in [23] will be presented. The necessary cuts on data and Monte Carlo are listed in the first subsection. Then follows a description of the method and how the jet classification from the previous section is applied. Finally the results from [23] are given together with a discussion on the determination of the systematic errors.

3.3.1 Track and Event selection

Charged particle cuts. The accepted charged tracks have

- been detected in the TPC
- been extrapolated to within 5 cm from the beam axis

	Detector		Generator	
	ANN	E_{jet}	ANN	E_{jet}
q_1	80.6%	72.5%	85.0%	77.1%
q_2	61.6%	57.6%	62.8%	58.0%
g_2	64.1%	60.1%	67.7%	61.9%
g_1	78.1%	70.0%	80.0%	73.2%
q_1 and q_2	45.9%	37.1%	51.3%	41.3%

Table 3.1: Jet identification probabilities in four-jet events. q_1 and g_1 are the most quark and gluon like jets respectively. In addition to the detector simulated data the results on generator level (no detector simulation) are shown. The number of simulated events were about 13000.

- been extrapolated to within 10 cm from the nominal crossing point in z
- a polar angle $25° \leq \Theta \leq 155°$
- a measured momentum $0.1 \leq p \leq 45$ GeV/c
- a measured length > 50 cm
- $\frac{\delta p}{p^2} < 0.02$ for $p \leq 1$ GeV/c and $\frac{\delta p}{p} < 0.02$ for $p < 1$ GeV/c.

In order to have reasonable statistics in the sum (3.4) the neutral particles are needed as well. This is one of the major differences, apart from the jet identification, between the analysis in [21, 22] and the one in [23]. For the neutral particles the momentum is required to be $0.5 < p < 45$ GeV/c.

Hadronic event selection. An event is accepted as hadronic if

- there is > 3 GeV visible energy in each z-hemisphere
- there is > 15 GeV total visible energy
- there is more than four tracks with $p > 0.2$ GeV/c
- the polar angle of the sphericity axis is in $[40°, 140°]$
- the total momentum imbalance is below 20 GeV/c

Jets are defined with the LUCLUS algorithm [32]. The jet resolution parameter d_{join} is fixed to 4 GeV. The event must contain exactly four jets. After the clusterization an additional cut requires the invariant mass of any jet pair to be greater than 9.1 GeV in order to comply with the invariant mass cut-off in the matrix element Monte Carlo. This latter cut together with the high d_{join} practically eliminates all the background to the four-jet events from fragmentation fluctuations of three and two parton events. From simulation we estimate this background to be less than one per mille.

Finally, each individual jet must have:

- a minimum multiplicity of four particles

- a measured energy of at least 7 GeV

Totally 6230 events in the DELPHI 1991 data sample were accepted. We did not include the 1990 data since we found a discrepancy the data and the Monte Carlo in the reconstruction of the neutrals. In principle one could of course use two different Monte Carlo samples for the correction of the 1990 and 1991 data respectively but that would make the analysis significantly more difficult.

3.3.2 Method

The following observation constitutes the foundation of the measurements in [21, 22, 23]: The grouping of the 4-parton graphs into the classes A,B,C,D and E at the end of section 3.1.3 is done in a gauge invariant way and hence one can determine the individual contribution from these classes. Given an arbitrary observable, ξ, the second order QCD prediction of its distribution reads:

$$\text{(3.6)} \qquad \begin{aligned}\text{Theo}(\xi) = \text{Norm} \times \alpha_s^2 \times [&C_F^2 A(\xi) + C_F(C_F - \frac{1}{2}N_C)B(\xi) + C_F N_C C(\xi) + \\ &+ C_F T_R D(\xi) + C_F(C_F - \frac{1}{2}N_C)E(\xi)]\end{aligned}$$

where "Norm" is the overall normalization factor. Allowing the factors Norm, C_F, N_C and T_R to vary freely one may fit the QCD prediction to the corresponding distribution for data "Data(ξ)". The fitted value for N_C is then a direct measurement of the triple-gluon vertex contribution. We eliminate one variable by substituting $X_1 = \text{Norm} \times \alpha_s^2 \times C_F^2$, $X_2 = \frac{N_C}{C_F}$ and $X_3 = \frac{T_R}{C_F}$:

$$\text{(3.7)} \quad \text{Theo}(\xi) = X_1 \times [A(\xi) + (1 - \frac{1}{2}X_2)B(\xi) + X_2 C(\xi) + + X_3 D(\xi) + (1 - \frac{1}{2}X_2)E(\xi)]$$

In [21, 22, 23] "Theo" and "Data" are two-dimensional distributions in the variables $|\cos\Theta^*_{NR}|$ and $\cos\alpha_{34}$. The (generalized) Nachmann-Reiter angle, Θ^*_{NR}, is defined as the angle between the vectors $(\mathbf{p}_1 - \mathbf{p}_2)$ and $(\mathbf{p}_3 - \mathbf{p}_4)$ where $(\mathbf{p}_1, \mathbf{p}_2)$ and $(\mathbf{p}_3, \mathbf{p}_4)$ are the momentum vectors of the primary $q\bar{q}$ and the secondary partons respectively. α_{34} is the angle between the secondary partons. $|\cos\Theta^*_{NR}|$ is sensitive to the fraction of $q\bar{q}q\bar{q}$ events but the triple-gluon vertex distribution does not differ significantly from that of double bremsstrahlung in this variable. $\cos\alpha_{34}$ is essentially complementary; it is sensitive to the difference between the triple-gluon vertex and the double bremsstrahlung, whereas the $q\bar{q}q\bar{q}$ distribution is similar to that of the triple-gluon vertex.

The primary $q\bar{q}$ jets are identified as the two most "quark like" jets, i.e. the two most energetic in [21, 22] and the two jets giving an ANN output closest to the quark target value in [23]. This, together with the use of neutral particles, are the essential differences between the two studies [21, 22] and [23].

To extract the distributions in $|\cos\Theta^*_{NR}|$ and $\cos\alpha_{34}$ for the different classes A-E we use the Lund JETSET 7.3 matrix element Monte Carlo [32]. It is not possible to generate the classes B and E separately since, for some values of the kinematical variables, their contribution to the cross-section become negative. Only the class C and the combined distributions A,B and D,E can be generated directly. With some "tricks" (changing the JETSET code slightly) it is also possible to generate the classes A and D separately and hence one may extract B and E from (A+B)-A and (D+E)-D respectively. A more "legal" way to obtain the classes B and E, used in both [21, 22] and [23], is to use the Abelian QCD toy-model, which exists as an option in

JETSET. This toy-model does not preserve the property of asymptotic freedom and therefore never can be a realistic alternative to QCD, but the rôle is limited to confronting the QCD predictions when comparing with data. The existence of such models is crucial for disentangling trivial kinematical effects from dynamical ones. The fact that the model can be ruled out by other measurements is in this connection irrelevant. The Abelian QCD model is designed to reproduce the ordinary QCD results for the total e^+e^- annihilation cross-section to hadrons as well as for the 2- and 3-jet rates. The distributions A-E are the same as in QCD but the weights are different: $C_F^{Abel} = 1$, $N_C^{Abel} = 0$ and $T_R^{Abel} = 3n_f$. Thus, the classes A and B can be extracted from the system:

$$\mathrm{Theo}_{AB}^{QCD}(\Theta^*_{NR}, \alpha_{34}) = C_F^{QCD} A(\Theta^*_{NR}, \alpha_{34}) + (C_F^{QCD} - \frac{1}{2} N_C^{QCD}) B(\Theta^*_{NR}, \alpha_{34})$$

$$\mathrm{Theo}_{AB}^{Abel}(\Theta^*_{NR}, \alpha_{34}) = N_{scale}\Big(C_F^{Abel} A(\Theta^*_{NR}, \alpha_{34}) + (C_F^{Abel} - \frac{1}{2} N_C^{Abel}) B(\Theta^*_{NR}, \alpha_{34})\Big)$$

where $N_{scale} \approx 0.68$ is a relative normalization factor which takes into account the different total 4-parton cross-sections in the two theories together with possible differences in detection acceptances. Its value (0.68) has been determined from large simulations with the JETSET 7.3 generator. The classes D and E are extracted from a similar system for "$\mathrm{Theo}_{DE}^{QCD}(\Theta^*_{NR}, \alpha_{34})$" and "$\mathrm{Theo}_{DE}^{Abel}(\Theta^*_{NR}, \alpha_{34})$".

It was realised in [22] that low statistics in the distributions for the different classes A-E introduces a bias in the final result. A study [33] showed that about 1.200.000 accepted (i.e. passed all cuts in section 3.3.1) generated events are needed. That enormous amount of events, corresponding to more than 10.000.000 before cuts, would never be feasible with full detector simulation as one DELPHI simulated four-jet event requires about 2 CPU minutes on an IBM 3090. The alternative is then to do the simulation on generator level and correct the data for detector effects before performing the fit. The number of detector simulated events needed for the correction function is not too large. In [22] the available statistics of DELPHI detector simulated parton-shower plus matrix-element events were used. However, for the analysis in [23] we were forced to generate our own subsample of detector simulated events. The reason was that for the neutral particles the available detector simulated data did not satisfactory describe the latest reprocessing of the 1991 data. A total of $\sim$ 55.000 parton-shower plus detector simulated events were generated on two HP-9000/730 machines in Lund. The CPU time amounts to about 38 CPU-days per machine plus some extra time for uncompleted jobs. Even though the preselection on the generator level was optimized, only about 14.000 of the 55.000 events passed the cuts defined in section 3.3.1. Tighter preselection would have introduced a bias. The final correction function, which is relatively flat, is parametrized by a second order polynomial in order to smooth out local fluctuations induced by the limited statistics. This procedure is in complete accordance with [22].

Also for the reference distribution A-E a separate generation was needed in [23] because of the same reason as for the detector simulated data. This was done on the *Central Simulation Facility* (CSF) at CERN. CSF is a cluster of 26 HP-9000/720 machines intended as a platform for running CPU intensive applications. About 20.000.000 events were generated to produce 2.000.000 and 1.200.000 accepted QCD and Abelian events respectively. The required $\sim$ 600 CPU hours could in real time be reduced to a few days by running 10 jobs in parallel.

The distributions obtained for the data, the correction function and the classes A-E are shown in Figure 3 and 4 in [23].

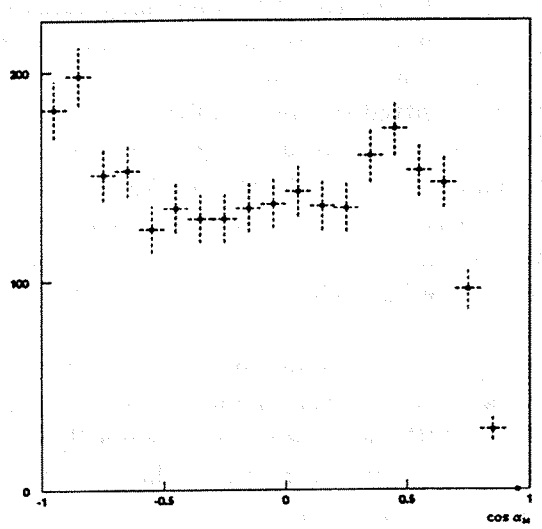

Figure 3.4: Projection of $\cos\alpha_{34}$ for $|\cos\Theta^*_{NR}| < 0.5$. The excess in the region $\cos\alpha_{34} \approx 0.4$ is a direct consequence of the existence of the triple-gluon vertex.

3.3.3 Results

The results from the free fit (3.7) to the data are:

$$\frac{N_C}{C_F} = 2.53 \pm 0.08(stat.) \qquad \text{(QCD value: 2.25)} \tag{3.8}$$

and

$$\frac{T_R}{C_F} = 1.62 \pm 0.41(stat.) \qquad \text{(QCD value: 1.875)} \tag{3.9}$$

The statistical errors are small relative to the analysis [22], which reflects the fact that the jet identification is better. In particular a structure in $\cos\alpha_{34}$, which originates from the triple-gluon vertex, has become visible in the data, see projection shown in Figure 3.4. The effect might be argued from the fact that the in case of the triple-gluon vertex the bremsstrahlung spectrum of daughter gluons in $g \to g + \ldots$ is governed by a $1/E_g$ pole for low energies. Thus, the two gluons are likely to be close together. In the case of double bremsstrahlung (class A and B) the gluons do not have any such reason to be close to each other. Note, that the effect is only visible when the gluons are well separated from the quarks ($|\cos\Theta^*_{NR}| \to 0$), see Figure 3 (*class c*) in reference [23]. When ($|\cos\Theta^*_{NR}| \to 1$) the bremsstrahlung process $q \to qg$, i.e. the production of the first gluon, dominates and the effect is washed out. The decrease for $\cos\alpha_{34} > 0.5$ is due to the finite jet resolution; the gluons are too close to be resolved.

Evidently, as the jet identification is based on the feature of fragmentation the model dependence must be estimated. As stated in section 3.2.2 the variables F_{nm} should by construction be rather insensitive to fluctuations in a model. This was confirmed in [25] where up to 50% variations in some of the fragmentations parameters in the Lund model did not significantly change the ANN performance. In [23] we investigated the influence on the results N_C/C_F and

T_R/C_F using the following procedure: twenty ANNs are independently trained with data samples generated with JETSET 7.3 parton shower plus string fragmentation. Each data sample is generated with an unique set of values on the three most important fragmentation parameters in the JETSET model. The parameter values are picked randomly within $\pm 10\%$ from their default values. All ANNs are subjected to the *same* matrix element QCD and Abelian generator data. The classes A-E are extracted and fitted to the data for each ANN. Thus, we obtain 20 different values on N_C/C_F and T_R/C_F which are shown in Figure 5 of reference [23]. The 10% variations in the model parameters give about 5% fluctuations in N_C/C_F. Note, that we do only vary the ANNs whereas the matrix element generator data is kept fixed. This ensures that only effects arising from the jet classification are accounted for. The influence of fragmentation variations in the matrix element data sample have already been studied and is quoted in [22] to give an error of 0.1 on N_C/C_F.

The 5% fluctuations in N_C/C_F also include possible differences in the learning of the ANNs. Such differences are unavoidable due to the random initialization of the ANN weights. No extensive check of the individual ANNs were performed primarily because it is rather meaningless to attempt to define a criteria for equal learning as the ANNs are all trained with different input data. In any case, the variation in the learning of an ANN should also contribute as a systematic error and there is no reason to try to disentangle this source from the fragmentation model dependence.

The found variation of 5% cannot serve as a true systematic error and it was never claimed to be one in [23]. The 10% variation in the fragmentation parameters was chosen arbitrarily. In a more complete study the fragmentation parameters should be varied to give for instance an one sigma change in a few important jet variable distributions like p_t to jet axis, number of particles in the jet, etc.. Obviously, such a study would be quite CPU time consuming especially since all the three fragmentation parameters must be allowed to vary freely at the same time.

Acknowledgement

In a large experiment like DELPHI the success depends heavily on the efforts of a large number of people. I therefore wish to thank the whole collaboration for making the present thesis possible at all. To my colleagues in the TPC group I owe a debt of gratitude for pleasant co-operation during meetings, detector shifts and private discussions.

To my supervisors Professor Göran Jarlskog and Dr. Bengt Lörstad I am greatly indebted for patient support and advice. It was Bengt who first introduced me to the ionization energy loss in the summer 1987. Dr. Torsten Åkesson deserves a special thanks for more than two and a half year of supervision. Without his support the analysis in Chapter 3 would not exist.

Many thanks to my friends and colleagues in the Lund and Orsay group at DELPHI. In particular Jonas, Lars and Ivan for many good laughs.

I wish to thank The Supercomputer Center North (SDCN) who put to my disposal an excellent computer environment where a large part of the analysis in chapter 3 was performed.

Financial support from The University of Lund and The Swedish Natural Science Research Council (NFR) is gratefully acknowledged.

Appendix A

The DELPHI time projection chamber

Nuclear Instruments and Methods in Physics Research A283 (1989) 567–572
North-Holland, Amsterdam

THE DELPHI TIME PROJECTION CHAMBER

C. BRAND, S. CAIRANTI, P. CHARPENTIER, D. DELIKARIS *, P. DELPIERRE *, H. FOETH, B.W. HECK, H.J. HILKE, A. SANCHO and J. WILDMAN

European Organization for Nuclear Research (CERN), Geneva, Switzerland

C. AUBRET, P. BILLOIR, C. BOUTONNET, P. COURTY, M. CROZON, A. DIACZEK, J. MAS, L. MATHIS, G. SAGET, A. TILQUIN, J.P. TURLOT and P. VERGEZAC

Collège de France, Paris, France

P. ANTILOGUS, J.E. AUGUSTIN, M. GAILLARD, M.H. GROS, A. HRISOHO, B. JEAN-MARIE, V. LEPELTIER, J.M. NOPPE, F. RICHARD and K. TRUONG

Laboratoire de l'Accélérateur Linéaire, Orsay, France

T. BOLOGNESE, P. BORGEAUD, M. DEBEER, G. GOUJON, M. GROS, P. JARRY, M. MUR, J.C. RAOUL, V. RUHLMANN, Y. SACQUIN, P. SIEGRIST, G. SMADJA, M. TURLUER and D. VILANOVA

CEN-Saclay, Gif-sur-Yvette, France

G. DARBO

INFN, Genoa, Italy

O. BÄRRING, G. JARLSKOG, S. KÄCK, B. LORSTADT and U. MJÖRNMARK

University of Lund, Sweden

The DELPHI TPC was under test, using cosmic rays and UV laser beams, for about one year, and is now being installed in the LEP tunnel. The construction is shortly reviewed, the data acquisition and the triggers based on the TPC information are described, and the measured performance is presented.

1. Introduction

The central detector of the DELPHI experiment at LEP is a large-volume time-projection chamber (TPC) working at atmospheric pressure, and designed with the following aims: good two-track separation with three-dimensional localization, efficient e/π separation (completed) by hadron identification with the RICH ring-imaging Cherenkov), and good momentum measurement (by combining TPC, vertex, inner and outer detectors' information) [1,2]. The arrangement of the DELPHI components is shown in fig. 1.

2. Mechanics

2.1. Main characteristics of the TPC

- active length: 2×134 cm;
- radius: 32.5–116 cm;
- volume: ~ 14 m^3;
- gas: 80% argon +20% CH_4 at atmospheric pressure;
- electric field: 150 V/cm;
- drift velocity: ~ 64 μm/ns;

* Permanent address: Collège de France, Paris, France

0168-9002/89/$03.50

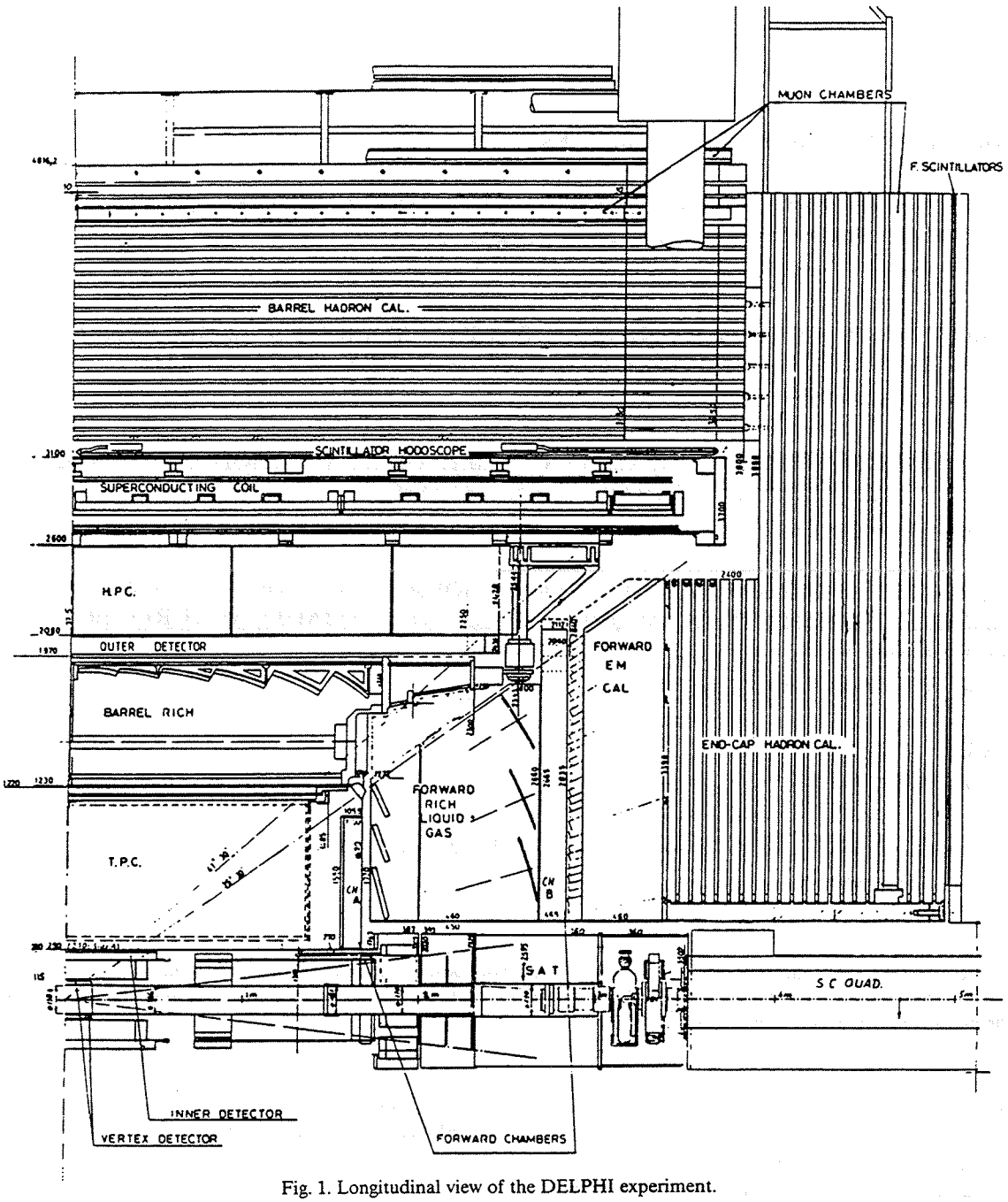

Fig. 1. Longitudinal view of the DELPHI experiment.

- maximum drift time: ~ 20 μs;
- magnetic field: 1.2 T;
- number of chambers: 2 × 6, each one with 192 sense wires and 16 pad rows.

2.2. Vessel

The inner and outer cylindrical walls are made of carbon-fibre composite, with a respective thickness of 1.7% and 2.2% of X_0, and are designed to support vacuum, thus allowing fast outgasing and refilling. The output signal connectors and the service lines (for gas, cooling water, HVs, ···) are arranged on both sides around an aluminium conical ring, which supports also the carbon-fibre end plate.

2.3. Field cage

The internal and external field cages are made from G-10 foils (1 mm and 2 mm thick), kapton-coated and

covered on both sides with 3 mm Cu strips 1 mm apart. The respective thicknesses are 1.6% and 2.1% of X_0.

The central anode is a 1 cm Al-honeycomb disk. The 20 kV high voltage is degraded through 4 MΩ resistors (333 per field cage) with a possible adjustment on the last two in order to correct possible small field distortions close to the chambers.

2.4. Proportional chambers

The 1680 pads of each chamber are arranged into 16 equidistant circular rows, so that the particle trajectory projections are nearly orthogonal to them. All the pads have the same area, and their positions are known to ±10 μm.

The plate is a G-10 sandwich of 2 + 4 mm thickness, coated with 70 μm copper, with a total flatness tolerance of 20 μm.

The distance from the pad plane to the three wire planes (sense + field wires, cathode grid and gate grid) is 4, 8 and 14 mm respectively. The gate wire spacing is 1 mm. To avoid ion feedback in the TPC, the gate wires are biased alternatively to ±100 V. This bias is switched off at each beam crossing for 3 μs, and during the full drift time on a positive answer from the first-level trigger.

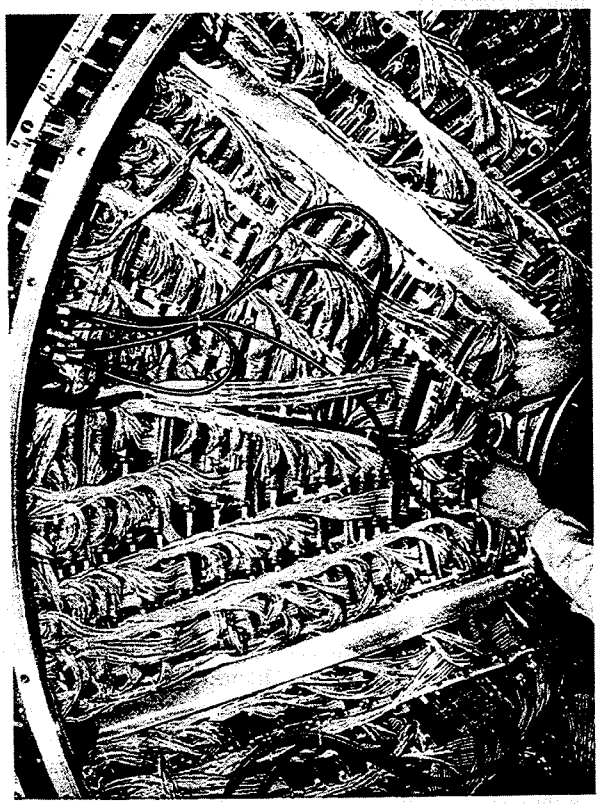

Fig. 2. View of the external side of a TPC sector.

The 12 chambers are now installed on the TPC; fig. 2 shows the cabling and the water cooling pipes.

3. Electronics

3.1. Channel electronics chain

The electronics chain has been described in previous papers [2]. In short, there are hybridized FET preamplifiers (EN < 600 e^-) on the chamber, two-stage shapers on FASTBUS boards (32 channels in one slot) and FADC digitizers (96 channels in three slots).

For the pads (12 × 1680 channels), the sampling frequency is 14 MHz for a shaping time of 170 ns fwhm. The digitizers are 8-bit FADCs working with a broken characteristic to have an equivalent 9-bit resolution in the minimum ionizing region. The digitizer boards include zero suppression and a four-event buffer.

For the wires the electronic chain is similar, but the sampling frequency is increased to 45 MHz to improve the two-track resolution.

3.2. Data acquisition system

The FADC memories are organized to record four events of 511 time slices. The event pointer is incremented only on a positive answer of the second-level trigger. The digitizer boards include a zero suppress processor which takes only the signals above a programmed threshold, but with the two adjacent ones. These data are read by a Fastbus crate processor (a FIP, Fastbus Intersegment Processor, based on a Motorola 68020) [3]. In the FIP, the data are corrected by a calibration table and processed for clustering. The FIPs are master on the back-plane and slave on the cable segment. The data in the FIPs (9 FIPs for 15 crates per half TPC) are read on the cable segments by the Local Event Supervisor (LES) and put in a multievent buffer. The third-level trigger processor (which is also a FIP) takes the data in this buffer and tries to confirm the tracks found by the second level trigger. On a negative answer, the event is killed (for all the detectors) in the multievent buffer, otherwise it is delivered to a set of emulators (fourth level trigger) which will tag the event before recording on tape (cartridge) via a VAX 8700 computer.

3.3. Trigger systems

The DELPHI track trigger uses the TPC information in the forward region (θ in the range from 0° to 32° and 148° to 180°) for the first level (up to 3 μs) and in the barrel region for the second level (up to 36 μs).

The forward track trigger is based on a correlation of the TPC "end-plate trigger" (EPT) with the trigger from

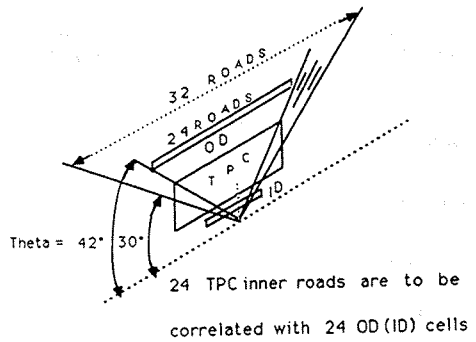

Fig. 3. Barrel Track Subtrigger acceptance.

the forward drift chambers (A and B, see fig. 1). The EPT samples signals from groups of wires (between 2 and 8 wires per group) at a frequency of 10 MHz. Tracks coming from the vertex will then be detected in fourfold coincidences made from the outputs of the registers [4].

The DELPHI Barrel Track Subtrigger (BTS) (see fig. 3) is a correlation between the TPC trigger data and the Inner and Outer Detector second-level trigger data (ID + OD, see the fig. 1) [5].

The TPC barrel subtrigger is made of two separate components: the $R-Z$ trigger [6] which looks for tracks pointing to the vertex inside 32 routes for each $R-Z$ region defined by the TPC sectors, and the Contiguity Trigger (CT) [4] which looks for clusters of points (16×24 per TPC sector) inside $R-\varphi$ regions defined by 16 cones pointing to the vertex.

The CT is made of 12 Fastbus modules (Contiguity Processor Slices – CPS), one for each sector. Each CPS receives its data from 16×24 pad groups of a TPC sector and works under the control of a 40-bit instruction word (its assembler defines a set of 60 instructions). The instructions that are executed at a rate of 10 MHz and are synchronized by the LEP timing, control the acquisition of an event (first 25 μs of the TPC drift time), the trigger algorithm (5–6 μs in addition) and the filter program that writes useful track information to the front-end buffer (FEB) for further processing in the following trigger levels. CPSs are based on an array of 16×24 processing elements, each one connected to its 4 neighbours. They execute the "contiguity mask algorithms".

The $R-Z$ trigger is simpler. The pads of a full pad row are grouped, giving a segmentation of only 60° in φ, but 32 cones in θ, the angle with the beam line. The principle is to read a RAM with a 10 MHz clock during the drift time and to make coincidences between the pad signals and the output of this memory. The RAM is loaded to give output pulses which correspond to a trajectory coming from the interaction region.

In order to join the forward track trigger, the barrel track trigger should have an acceptance in θ between 30° and 150°. This is done by software for the two TPC trigger systems. For the OD (ID) we receive a 24-bit word per pair of sectors, corresponding to 42° to 138°. The correlation is first done on the basis of a 60° segmentation in φ, between the OD (ID) words and the 24 internal bits of the $R-Z$ trigger words (32 bits) [5]. Then the result (32 cones per pair of sectors) is correlated with the 16 cones of four sector parts from the contiguity trigger, giving an answer with 32 cells in θ and 24 cells in $R-\varphi$ for the whole detector. The hit cells are then counted and the trigger answer is: 0 track, 1 track, 2 tracks or more than 2 tracks, coded in two bits. All the row data words are stored in a four-event buffer.

The data corresponding to the detector tracks are then read via Fastbus by the third-level processor (Motorola 68020) which will try to confirm those tracks.

4. Performances

4.1. Gain measurements

The dE/dX measurement on the wires requires a very good knowledge of the wire gain.

For the gain calibration each chamber is equipped at its end-plate with three switchable ^{55}Fe sources under each wire, and for the temperature monitoring with eight Pt resistors.

In addition, full gain maps have been registered at Saclay for each chamber [7], with all electronics operating, using a continuously rotating radial ^{55}Fe source. The very good gain homogeneity (better than 1% in the major part of the sector) reflects the quality of the mechanical construction.

4.2. Laser calibrations

A miniature nitrogen laser, developed at NIKHEF, is used to monitor the TPC, with the following features:
- wavelength: 337 mm;
- pulse energy: ~ 70 μJ;
- pulse length: 0.8 ns (FWHM);
- divergence: diffraction limit.

Each chamber is equipped with a laser, following the arrangement shown on fig. 4a. The corresponding TPC volume is crossed in its median plane by three laser beams, the first one parallel to the wire plane, the two others sloped with an angle of about 60°.

Fig. 4b shows the mean drift velocity in the TPC, obtained from the measured time difference between inclined and parallel tracks. The variation near the field cage could be due to the laser mirror assembly near this one. The relative variation of drift velocity, due to gas pressure, composition or temperature variations, or contamination, is measured with a precision of 10^{-3}, but some remaining uncertainties on the geometrical posi-

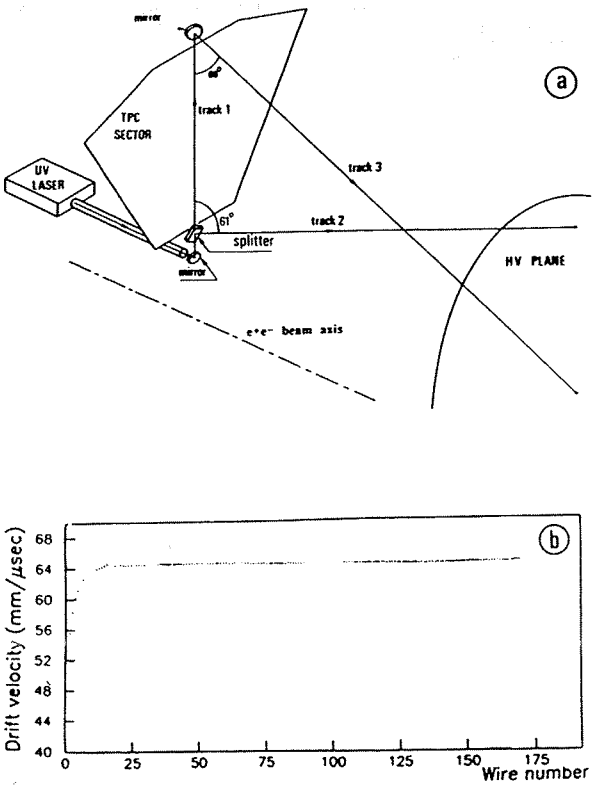

Fig. 4. Laser arrangement (a) and drift velocity (b) in the TPC versus Y (wire number).

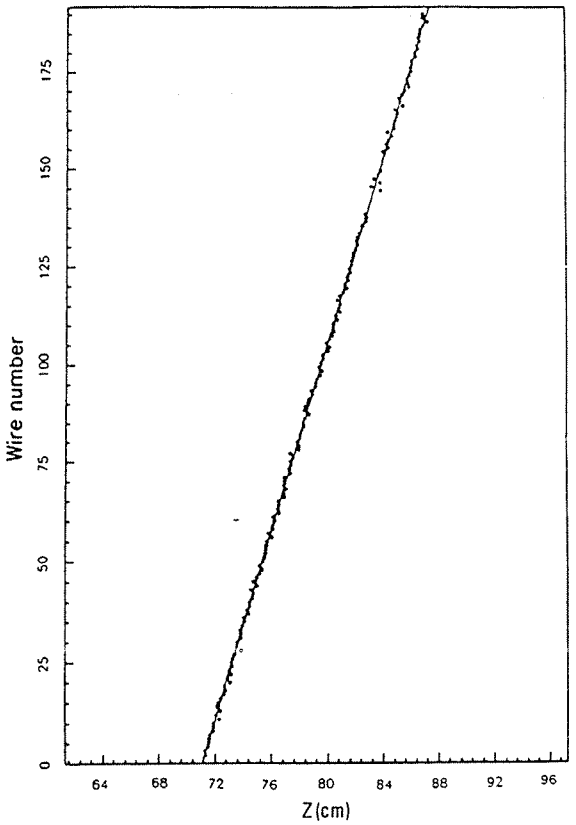

Fig. 5. Cosmic ray event in the $Z-Y$ projection.

tions of the laser beams limit up to now the absolute measurement of the drift speed to a few times 10^{-3}.

4.3. Cosmic rays tests

Each chamber has been successively triggered for long periods with cosmic rays crossing the corresponding drift space. Fig. 5 shows an event in the $Z(=vt)-Y$(wire) projection. Preliminary analysis gives a longitudinal resolution between 0.75 and 1.2 mm depending upon the angle θ. The resolution in the $X-Y$ plane perpendicular to the Z-axis could not be measured in these tests since we had no magnetic field. From a measurement performed on a prototype with a 1.2 T magnetic field using a pion beam, we got a transverse resolution between 100 and 300 μm, depending upon the angle between the particule trajectory and the pad row.

4.4. Particle identification

From a test in a 20 GeV pion beam, we have measured the dE/dX resolution: $\sigma(dE/dX) = (5.5 \pm 0.5)\%$, after truncation of the upper half of the wire signals.

To improve this value, more sophisticated statistical methods have been developed: the first one taking into account the correlation between the truncated mean value of the energy distribution and its variance, and the second using the shape of the Landau energy distribution for a Kolmogorov test.

5. Conclusion

The one-year test at CERN using cosmic rays and laser beams was very fruitful to debug mechanical and electronical problems on the TPC, and to check its good behaviour, but without magnetic field it was not possible to get final performances.

References

[1] DELPHI Technical Proposal, CERN/LEPC 83-3, LEPC/P2 (17 May 1988).
[2] C. Brand et al., IEEE Trans. Nucl. Sci. NS-36 (1989) 122.

[3] P. Charpentier et al., IEEE Trans. Nucl. Sci. NS-34 (1987) 137.
[4] G. Darbo et al., IEEE Trans. Nucl. Sci. NS-34 (1987) 227.
[5] The Barrel Track Subtrigger, DELPHI Internal Note, to be published.
[6] The TPC R-Z Trigger, DELPHI Internal Note, to be published.
[7] P. Antilogus, Thèse LAL 88/19 (1988).

Appendix B

Energy loss calculations with fast Fourier transform routines

Nuclear Instruments and Methods in Physics Research A284 (1989) 459–463
North-Holland, Amsterdam

ENERGY LOSS CALCULATIONS WITH FAST FOURIER TRANSFORM ROUTINES

O. BÄRRING

Physics Department, University of Lund, Sölvegatan 14, S-22362 Lund, Sweden

Received 22 June 1989

The efficiency of particle identification by energy loss analysis is improved with the availability of a fast and accurate method for calculation of the energy loss spectrum. In this paper a simple algorithm based on the Laplace transform method will be given. The algorithm differs from earlier approaches with this method in that it makes use of Fast Fourier Transform routines instead of numerical integration or series expansion. This makes it possible to speed up the calculations without any significant loss of information, i.e. the cross section differential in energy does not need to be approximated.

1. Introduction

In order to determine the energy loss of a charged particle traversing a finite layer, mainly three different methods have been used:

(1) The Monte Carlo simulation method which has been described by for example Lapique–Piuz [1] and Lynch [2].
(2) The convolution method, see for example Allison–Cobb [3] or Allison–Wright [4].
(3) The Laplace transform method introduced by Landau [5] and later used by Talman [6].

The Laplace transform method, which solely will be discussed here, is based on an exact integral formula, due to Landau [5], for the energy loss distribution. The next section concerns a short derivation of the Landau formula and how it can be reformulated to an expression which is easily implemented in a computer program. A simple way of convoluting a known distribution and the energy loss spectrum, to take into account smearing effects like transversal diffusion, concludes section 2. In section 3 calculated results are compared with data from two different wire chambers. An interesting effect at small sample lengths, discussed by Allison–Wright [4], is recovered. There will also be a discussion of the performance of the method and how to chose the free parameters. One Appendix treats the calculation of the cross section differential in energy for an argon/methane mixture.

2. Theory

In the notation of Landau [5] $f(x, \Delta)\,\mathrm{d}\Delta$ denotes the probability that a particle, with some initial energy E, will lose an amount of energy lying between Δ and $\Delta + \mathrm{d}\Delta$ when it traverses a layer x. It is assumed that $\Delta \ll E$, which simply means that the kinetic energy of the particle is considered to be unchanged in the process.

With $(\partial^2 N/\partial x \partial E)(E)\,\mathrm{d}E$ as the probability of a collision involving an energy transfer between E and $E + \mathrm{d}E$ from the incoming particle to the medium per unit distance, the probability distribution of an energy loss $E_{\mathrm{d}x}$ in the layer $\mathrm{d}x$ is given by

$$P_{\mathrm{d}x}(E_{\mathrm{d}x}) = \delta(E_{\mathrm{d}x})\left(1 - \mathrm{d}x\int_0^\infty \frac{\partial^2 N}{\partial x\,\partial E}(E)\,\mathrm{d}E\right) + \mathrm{d}x\frac{\partial^2 N}{\partial x\,\partial E}(E_{\mathrm{d}x}).$$

The first term describes the probability of zero energy loss. $\mathrm{d}x$ is assumed to be so small that the probability of multiple collision is negligible. If $f(x,\Delta - E_{\mathrm{d}x})$ and $P_{\mathrm{d}x}(E_{\mathrm{d}x})$ are known for $E_{\mathrm{d}x} \leqslant \Delta$ it follows that

$$\begin{aligned} f(x + \mathrm{d}x, \Delta) &= \int_0^\Delta f(x, \Delta - E_{\mathrm{d}x})\,P_{\mathrm{d}x}(E_{\mathrm{d}x})\,\mathrm{d}E_{\mathrm{d}x} \\ &= f(x, \Delta)\left(1 - \mathrm{d}x\int_0^\infty \frac{\partial^2 N}{\partial x\,\partial E}(E)\,\mathrm{d}E\right) \\ &\quad + \mathrm{d}x\int_0^\Delta f(x, \Delta - E_{\mathrm{d}x})\frac{\partial^2 N}{\partial x\,\partial E}(E_{\mathrm{d}x})\,\mathrm{d}E_{\mathrm{d}x}. \end{aligned}$$

The upper limit of the second integral can be changed to infinity, as $f(x, \Delta - E_{\mathrm{d}x}) = 0$ for $E_{\mathrm{d}x} > \Delta$, i.e. the probability of negative energy loss is zero. Hence

$$\begin{aligned} &f(x + \mathrm{d}x, \Delta) - f(x, \Delta) \\ &= \mathrm{d}x\int_0^\infty [f(x, \Delta - E) - f(x, \Delta)]\frac{\partial^2 N}{\partial x\,\partial E}(E)\,\mathrm{d}E \end{aligned}$$

or

$$\frac{\partial f}{\partial x}(x, \Delta) = \int_0^\infty [f(x, \Delta - E) - F(x, \Delta)] \frac{\partial^2 N}{\partial x\, \partial E}\, \mathrm{d}E.$$

This equation can be solved by taking the Laplace transform of both sides

$$\frac{\partial \tilde{f}}{\partial x}(x, s) = \int_0^\infty [\tilde{f}(x, s)\, \mathrm{e}^{-sE} - \tilde{f}(x, s)] \frac{\partial^2 N}{\partial x\, \partial E}(E)\, \mathrm{d}E$$

$$\rightarrow \tilde{f}(x, s) = \tilde{f}(0, s) \times \exp\left[-x \int_0^\infty (1 - \mathrm{e}^{-sE}) \frac{\partial^2 N}{\partial x\, \partial E}(E)\, \mathrm{d}E \right].$$

The boundary condition is $f(0, \Delta) = \delta(\Delta) \rightarrow \tilde{f}(0, s) = 1$. Finally we obtain $f(x, \Delta)$ by inverting the Laplace transform

$$f(x, \Delta) = \frac{1}{2\pi \mathrm{i}} \int_{\sigma - \mathrm{i}\infty}^{\sigma + \mathrm{i}\infty} \times \exp\left[s\Delta - x \int_0^\infty (1 - \mathrm{e}^{-sE}) \frac{\partial^2 N}{\partial x\, \partial E}(E)\, \mathrm{d}E \right] \mathrm{d}s, \tag{1}$$

where the contour of integration is along a line parallel to the imaginary axis and displaced a distance σ to the right. With a simple change of variables ($s \rightarrow \sigma + \mathrm{i}y$) the formula (1) can be rewritten as

$$f(x, \Delta) = \frac{1}{2\pi} \exp\left\{ \sigma\Delta - x \int_0^\infty \frac{\partial^2 N}{\partial x\, \partial E}(E)\, \mathrm{d}E \right\} \int_{-\infty}^\infty \mathrm{e}^{\mathrm{i}y\Delta} \times \exp\left[\int_0^\infty \mathrm{e}^{-\mathrm{i}yE} \left(x\, \mathrm{e}^{-\sigma E} \frac{\partial^2 N}{\partial x\, \partial E}(E) \right) \mathrm{d}E \right] \mathrm{d}y$$

or

$$f(x, \Delta) = \exp\left\{ \sigma\Delta - x \frac{\partial N}{\partial x} \right\} \boldsymbol{F}^{-1} \times \left\{ \exp\left[\boldsymbol{F}\left(x\, \mathrm{e}^{-\sigma E} \frac{\partial^2 N}{\partial x\, \partial E}(E) \right)(y) \right] \right\}(\Delta), \tag{2}$$

where $\boldsymbol{F}$ denotes the Fourier transform. σ that defines the contour of integration in the Laplace transform should be a small but finite positive number which in numerical calculations can be set equal to zero.

In the form of expression (2), the implementation with FFT-routines is straightforward. A program flow chart can have the following structure:

(1) Input: x (sample length), $\beta\gamma$ (p/mc) and P (pressure)

(2) Calculate

$$x \frac{\partial^2 N}{\partial x\, \partial E}\left(\frac{kE_{\max}}{n} \right) \quad \text{for } k = 0, 1, \ldots, n-1$$

and put the result in an array $\mathrm{Re}(0 : n-1)$. Initialize another array $\mathrm{Im}(0 : n-1) = 0$.

(3) Execute a Fast Fourier routine and put the image function in Re and Im.

(4) Let $\mathrm{Re}(l) = (E_{\max}/n) \exp(\mathrm{Re}(l)) \cos(\mathrm{Im}(l))$ and $\mathrm{Im}(l) = (E_{\max}/n) \exp(\mathrm{Re}(l)) \sin(\mathrm{Im}(l))$.

(5) Execute a routine for inverse Fourier transforms and put the result in Re and Im.

(6) Normalize Re.

(7) Output: Re.

$E_{\max}$ is an upper cut-off energy above which $\partial^2 N/\partial x \partial E = 0$ (see discussion in the end of section 3).

The output from this algorithm is a vector $\mathrm{Re}(0 : n-1)$ where $\mathrm{Re}(j)$ is the probability of an energy loss $\Delta = jE_{\max}/n$. Observe that $\mathrm{Im}(0 : n-1) = 0$ within numerical errors.

Formulae (2) gives the intrinsic energy loss, i.e. the energy lost by the particle when it traverses a layer x. Since the measured quantity is usually the ionization induced by this intrinsic energy loss it would be preferable to also include the unavoidable smearing of the energy loss distribution due to, e.g. transversal diffusion of the electrons drifting to the sensing device. The convolution of $f(x, \Delta)$ and a function $g(\Delta)$ describing the smearing can be performed using:

$$\int_{-\infty}^\infty g(\Delta - E) f(x, E)\, \mathrm{d}E = \boldsymbol{F}^{-1}(\hat{f}(x, y) \hat{g}(y))(\Delta), \tag{3}$$

where $\hat{f}$ and $\hat{g}$ denotes the corresponding Fourier transforms to f and g. Thus (2) becomes ($\sigma = 0$)

$$f(x, \Delta) = \exp\left(-x \frac{\partial N}{\partial x} \right) \boldsymbol{F}^{-1} \times \left\{ \hat{g}(y) \exp\left[\boldsymbol{F}\left(x \frac{\partial^2 N}{\partial x\, \partial E}(E) \right)(y) \right] \right\}(\Delta). \tag{4}$$

In some cases, e.g. describing fluctuations in the ionization for a certain energy loss Δ, it seems more logical to introduce the smearing at level of $\partial^2 N/\partial x\, \partial E$:

$$f(x, \Delta) = \exp\left(-x \frac{\partial N}{\partial x} \right) \boldsymbol{F}^{-1} \times \left\{ \exp\left[\hat{g}(y) \boldsymbol{F}\left(x \frac{\partial^2 N}{\partial x\, \partial E}(E) \right)(y) \right] \right\}(\Delta). \tag{5}$$

Despite their formal simplicity (4) and (5) involves some practical difficulties: firstly it should be noted that they are only approximately valid when going over to numerical calculations. However, it seems possible to suppress the error in most cases. Secondly, the formula-

tion of many different smearing effects (e.g. diffusion, avalanche, electronic noise) into one single function $g(\Delta)$ is far from trivial. A practical solution would be to choose a well known function (e.g. a Gaussian) with one or two free parameters which can be tuned to data.

3. Results

A program, in the following called the FFT-program, based on the flow chart given in previous section (no smearing) has been tested against the result from two different wire chambers: the Berkeley Time Projecting Chamber (TPC) [9] and the External Particle Identifier (EPI) at CERN [10]. Both groups used a truncated mean as an estimate of the most probable energy loss (see table 1).

Table 1

Detector	*Conditions*
Berkeley TPC	layer thickness 0.4 cm pressure 8.5 atm mixture $\nu_{Ar} = 0.8$, $\nu_{CH_4} = 0.2$ truncation [a] 65%
EPI	layer thickness 6 cm pressure 1 atm mixture $\nu_{Ar} = 0.95$, $\nu_{CH_4} = 0.05$ truncation [a] 40%

[a] Truncation has here the meaning of the remaining part after truncation e.g. truncation = 65% means that only the lowest 65% of the samples are used to calculate the mean.

Fig. 1 shows the measured relative mean ionization I/I_{min} versus $\log_{10}(\beta\gamma)$ together with the same quantity calculated by the FFT-program. Since no smearing was included in the program the good agreement between data and calculations implies that the truncated mean is rather insensitive to the smearing effects discussed in the previous section. On the other hand if an accurate energy loss spectrum is available for all possible $\beta\gamma$ it seems rather inefficient to use just the truncated mean in the particle identification. The TPC group in the DELPHI experiment at LEP, CERN [11], has decided to exploit the full energy loss distribution in the particle identification. In order to do that the output from the FFT-program is compared to the measured pulseheight spectrum using some statistical method (in this case the Kolmogorov test). Five different mass hypotheses (e, μ, π, K and p) are tested for each track.

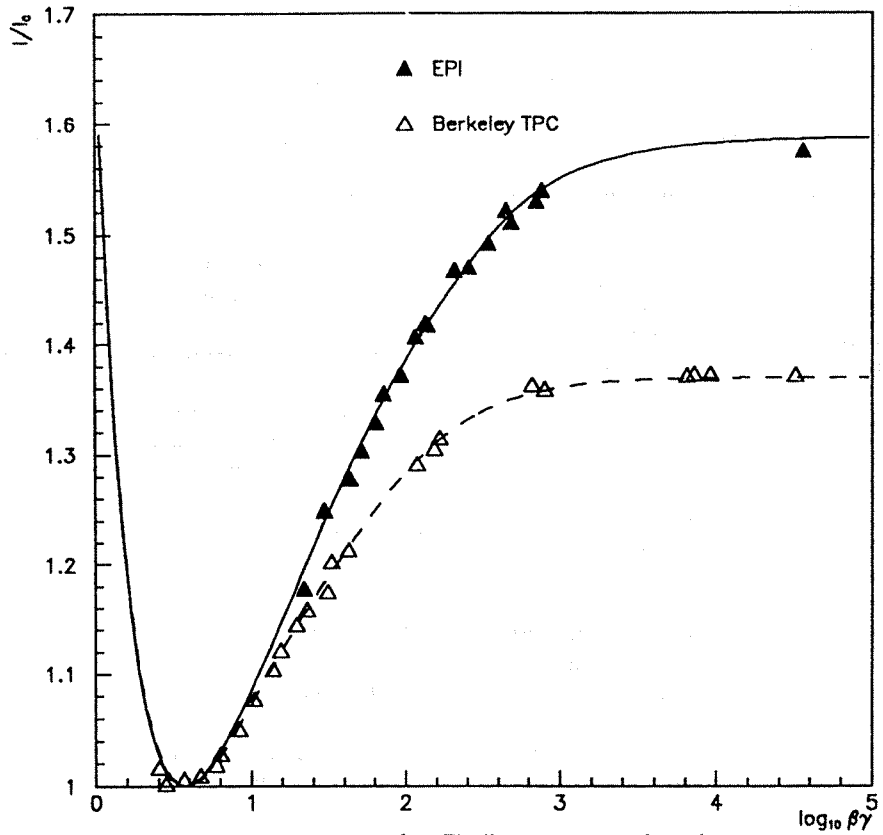

Fig. 1. Truncated mean $\log_{10}(\beta\gamma)$. The lines are outputs from the program.

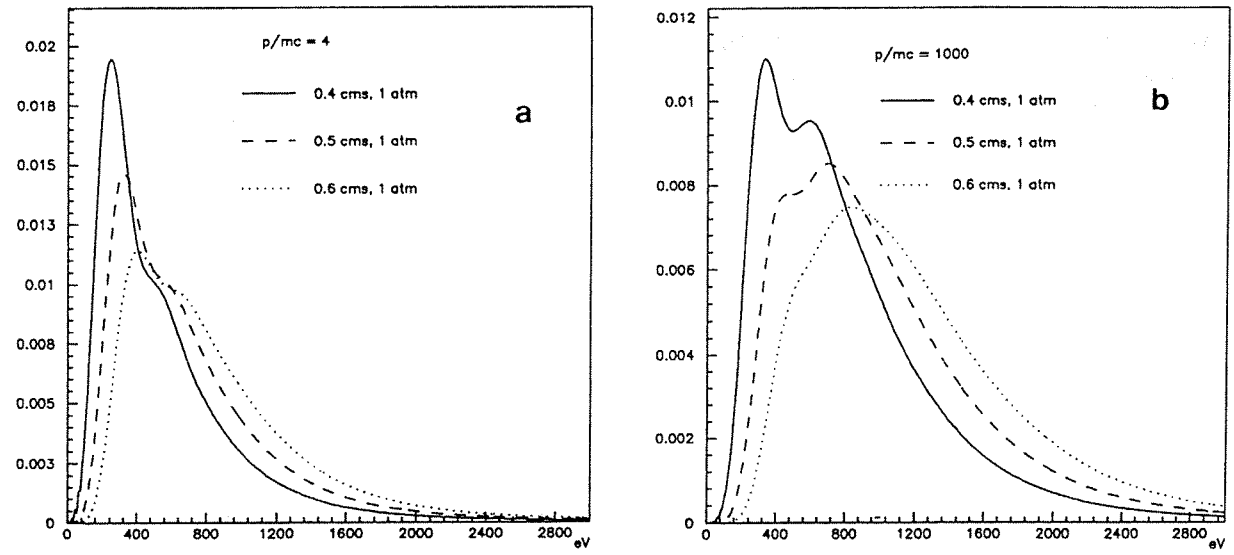

Fig. 2. dE/dx distributions for different sample lengths. $\nu_{CH_4} = 20\%$.

A description of this method will probably be published elsewhere.

The shape of the energy loss (Landau) distribution has more structure for small values of xP, such as the 0.4 (cm atm) in the DELPHI TPC, which can be seen in fig. 2. This behaviour has already been predicted by Allison–Wright [4], who explain it as a *vestigial effect of the shell structure*. The fine structure, i.e. the knee for $\beta\gamma = 4$ and the split into two maxima for $\beta\gamma = 1000$, in the shape will probably not be seen under experimental conditions because of smearing. The uncertainty in the model for the oscillator strength density of methane may also give discrepancies between the real and the predicted shape. As seen from fig. 2 the split has almost disappeared for $xP = 0.6$ cm atm which implies that if the effect should be seen in the DELPHI TPC it has to be for a track parallel to the wire-plane and perpendicular to the wires.

Finally a short discussion about the timing and the choice of parameters. As the program was written, the CPU time for producing one energy loss distribution goes approximately as $0.8n$ ms on a VAX 8650 (there is in addition also a weak variation with xP) where n is the number of slices in energy. The necessary size of n depends on the parameter E_{max} which is the maximum energy transfer in one interaction. Once E_{max} has been chosen it is easy to test different n in increasing order until the shape of the output distribution does not seem to change any more. How should E_{max} be chosen? Actually the theoretical value of this parameter is $2m_e c^2\beta^2\gamma^2$ but this value (numerically in the MeV region) cannot be accurate for thin samples since an electron receiving that energy would probably escape from the layer. The value that Lapique–Piuz [1] used for 1 cm layers at 1 atm was 15 keV. With $E_{max} = 15$ keV an n value of around 3000 would be sufficient which gives a CPU time of 2.4 s.

4. Conclusions

dE/dx calculations with the FFT-method give results on the truncated mean that agrees well with data. A simple facility exists to take into account smearing (due to e.g. transversal diffusion) of the calculated spectrum. This is probably necessary when using more refined entities than just the truncated mean in the analysis.

The time to produce one energy loss distribution with n slices in energy goes approximately as $0.8n$ (ms) on a VAX 8650. One free parameter E_{max} corresponding to the maximum energy transfer in one collision needs to be determined. The choice of this parameter is not very crucial as long as it is far out on the Landau tail (several keV).

Appendix A

The cross section differential in energy

The two wire chambers referred to in the text (Berkeley TPC and EPI at CERN) were both filled with an argon/methane mixture. Here follows a brief treatment of $\partial^2 N/\partial x \partial E$ for this gas mixture.

The cross section differential in energy $\partial^2 N/\partial x\,\partial E$ can be approximated by:

$$\frac{\partial^2 N}{\partial x\,\partial E} = \frac{\alpha F(E)}{\beta^2 E}\left[\ln\left(\frac{2m_e c^2\eta^2}{E\,|1+\eta^2(1-\epsilon)\,|}\right) - \beta^2\epsilon_1\right] + \frac{\alpha\left(1-\beta^2 E/E_{\max}\right)}{\beta^2 E^2}\int_0^E F(E')\,\mathrm{d}E', \qquad (6)$$

where

$\eta = \beta\gamma$,

$\epsilon = \epsilon_1 + i\epsilon_2$ is the complex refractive index,

m_e = electron mass,

and

$F(E)$ oscillator strength density,

α is proportional to the electron density of the medium. For pure argon it takes the value $123.3P$ (P = pressure in atm). Hence, since argon and methane have 18 and 10 electrons, respectively,

$$\alpha = 123.3\,P\frac{18\nu_{\mathrm{Ar}} + 10\nu_{\mathrm{CH_4}}}{18}$$

for a mixture with the fraction ν_{Ar} of argon and $\nu_{\mathrm{CH_4}}$ of methane.

The derivation of (6) is achieved in many papers, see for instance Allison–Cobb [3] and it will not be repeated here. A correction factor $(1-\beta^2 E/E_{\max})$ in the Rutherford term has been included in accordance with Talman [6] and Lynch [2]. The Cherenkov term is excluded in formula (6) because it is negligible in comparison with the other terms.

$F(E)$, the oscillator strength density, is within the dipole approximation, proportional to the photo-ionization cross section σ_γ. A tabulation of σ_γ for argon is given in [8]. A tabulation of σ_γ for methane cannot be found in the literature but the parametrisation given in [9] is accurate enough for our purpose.

$\epsilon = \epsilon_1 + i\epsilon_2$, the complex refractive index, is related to $F(E)$ through:

$$\epsilon_2(E) = \frac{\pi}{2}E_p^2\frac{F(E)}{E}$$

and

$$\epsilon_1(E) = 1 + E_p^2 \boldsymbol{P}\int_0^\infty \frac{F(E')}{E'^2 - E^2}\,\mathrm{d}E' \approx 1 - \left(\frac{E_p}{E}\right)^2\int_0^E F(E')\,\mathrm{d}E',$$

where $\boldsymbol{P}$ denotes the Cauchy principal value. E_p is the plasma frequency of the medium, which for argon is 0.82 eV at 1 atm. The square of the plasma frequency is proportional to the electron density of the medium or, similar, to the mean number of electrons per molecule and the pressure. Thus for an argon/methane mixture:

$$E_p^2 = (0.82)^2 P\frac{18\nu_{\mathrm{Ar}} + 10\nu_{\mathrm{CH_4}}}{18}$$

with P in atmospheres and E_p in eV.

References

[1] F. Lapique and F. Piuz, Nucl. Instr. and Meth. 175 (1980) 297.

[2] G. Lynch, TPC Internal Note TPC-LBL-81-6, unpublished.

[3] W.W.M. Allison and J.H. Cobb, Ann. Rev. Nucl. Part. Sci. 30 (1980) 253.

[4] W.W.M. Allison and P.R.S. Wright, Formulae And Methods In Experimental Data Evaluation (1984), vol. 2, part E.

[5] L. Landau, J. Phys. USSR 8 (1944) 201.

[6] R. Talman, Nucl. Instr. and Meth. 159 (1979) 189.

[7] T. Lindelof and H. Renshall, Memorandum CERN program library DD/TL/81/9, rev. 4 (1981).

[8] G.V. Marr and J.B. West, At. Data Nucl. Data Tables 18 (1976).

[9] M. Shapiro, PhD Thesis, LBL – 18820 (1984), unpublished.

[10] I. Lehraus, R. Matthewson, W. Tejessy and M. Anderholz, Nucl. Instr. and Meth. 153 (1978) 347.

[11] C. Brand et al., The DELPHI Time Projection Chamber, IEEE Trans. Nucl. Sci. NS-36 (1) (1989) 122.

Appendix C

Jet Classification with a neural network

DELPHI Collaboration

DELPHI 90-59 PHYS 78
12 December 1990

JET CLASSIFICATION WITH A NEURAL NETWORK

T. Akesson, O. Bärring

University of Lund

Jet Classification With a Neural Network

T.Åkesson O.Bärring [1]

Department of Particle Physics
University of Lund
Sölvegatan 14
S-223 62 Lund
Sweden

Abstract

A recently proposed method for jet classification with neural network technics is reviewed. We apply this method to separate gluon from quark jets in DELPHI detector simulated data. Showing one jet at a time we require the neural network to determine whether this jet has a gluon or a quark as origin parton. The performance is discussed emphasizing the relation between efficiency and purety of the selection. The neural network distinguishes gluon from quark jets on quantities such as E and z, e.g. high energy jets with hard fragmentation are most likely to be assigned as quark jets.

[1] E-mail akesson@quark.lu.se, barring@quark.lu.se

1 Introduction

Various applications of Neural Networks, NNw, in jet physics were originally proposed by [1, 2]. At generator level they successfully separate gluon from quark jets and heavy flavour quark jets from lighter. In most cases this was done on a jet by jet basis, i.e. the NNw never saw the full structure of the event. Despite the small amount of information given to the NNw it performed surprisingly good. E.g. with 16 input signals, p_x, p_y, p_z and E of the four leading particles in a jet, they reached a quark/gluon separation efficiency of 85-90%.

The present paper is an analysis on how the above technique applies to DELPHI detector simulation data. The aim is to investigate the method as such, no actual physics results will be given. The MC used is "parton shower" + full detector simulation. In order to minimize the ambiguity when assigning jets to partons, only 3-jet events are considered. The first section briefly introduces NNw for those not familiar to them. Then follows a discussion of the necessary cuts on data—it is obviously quite important that real data and MC look alike if a NNw trained on the latter is expected to give sensible results with the first. Section 4 is devoted to practical details in the training of the NNw. Finally some results are given comparing the NNw classified jets with jets were the origin parton is known.

2 Neural Networks

This section is meant to give a short introduction to NNw. For a more detailed treatment of the "back-propagation" learning rule we recommend [3] and [4].

A NNw may be considered as a simple imitation of the human neural system. In resemblance with its biological analogue, a NNw distributes complicated calculations over several processing entities, the "neurons". The task of the neurons varies between different types of NNw. During a training period, the NNw should learn to associate given input and feature patterns. When the NNw has learned enough for a particular application, the training is terminated. The NNw should then be able to, for a given input, present an answer resonably close to the feature pattern. This is required even if the NNw has not seen exactly the same input pattern during the training.

There are several types of NNw, here we only consider the "layered feed forward" NNw, which is depicted in figure 1. It consists of neurons arranged in a layered structure. The neurons are connected between the layers. To each pair (ij) of connected neurons is associated a weight ω_{ij}, which is an important ingredient in this type of NNw. The output of a neuron j is a function f of the net total output, a_j:

$$a_j = \sum_i \omega_{ij} x_i$$

where x_i are the input signals to the neuron. The requirements on f is that it

is a nondecreasing and differentiable function. We have used a soft threshold function,

$$f(a) = \frac{1}{1+e^{-a}}$$

shown in figure 1.

During the training, the NNw output o_p for a given input pattern x_p is compared with the desired output t_p. If the difference is nonzero the weights ω_{ij} are changed to reduce this difference. The "back-propagation" learning rule is a recursive procedure to accomplish this. In principle it is a minimization of an error function,

$$E_p = \frac{1}{2}\sum_j (t_{pj} - o_{pj})^2$$

where the sum is over all nodes in the output layer. We refer to [3] for a description and mathematical derivation of the back-propagation learning rule (called generalized delta rule in [3]).

After the training a test phase takes place. The network previously trained is tested on data it has not seen before. Thus, its ability of generalization is tested.

3 Event and track selection

For the track selection we have used the following cuts [5]:

- Charged track extrapolation to within 5 cm of the beam axis in R and to within 10 cm in z of the nominal crossing point in z.
- $0.1 < p_{charged} < 45.0$ GeV/c
- Measured track length > 50 cm.
- Polar angle cut $25° < \Theta < 155°$.

In addition to those more or less standard cuts we had to require,

- $\frac{\delta p}{p^2} < 0.02$ for $p > 1$ GeV/c and $\frac{\delta p}{p} < 0.02$ for $p < 1$ GeV/c.
- $0.5 < p_{neutral} < 45$ GeV/c.

Since the NNw is fed with the four leading particles of the jet, we believe it is rather important that the high momentum particles are well described in the Monte Carlo. That this is indeed the case can be seen from the p distributions in figure 2.

For the selection of hadronic events we use [5],

- > 3 GeV visible energy in each z hemisphere.

- $>$ 15 GeV total visible energy.
- $>$ 4 tracks with $p > 0.2$ GeV/c.
- Cut on the polar angle of the sphericity axis $40° < \Theta_{sph} < 140°$.

The clustering is done by LUCLUS (version 6.3) with a cut on relative p_T of two particles set to 3.5 GeV. The event is then accepted if LUCLUS assigns it as a 3-jet event and it fulfils,

- Multiplicity in smallest jet $>$ 4.
- $E_{jet} > 10.0$ GeV for least energetic jet.
- Smallest angle between two jets $> 30°$.
- $Q_2 > 0.01$ where Q_2 is the second largest normalized eigenvalue to the sphericity tensor.
- $|\hat{j}_1 \cdot (\hat{j}_2 \times \hat{j}_3)| < 0.25$ where $\hat{j}_1$ etc. are unit vectors in the jet directions.

The last and second last cuts are the same as AMY [6] used to select planar events, and to reduce the two-jet type events, respectively.

4 Training of the neural network

For the purpose of testing the performance of NNw in jet analysis we decided to concentrate on one particular network architecture; 16 input nodes $(\vec{p}, E)$ of the four leading particles in a jet and one output node taking the value "0" if the input jet originates from a quark and "1" if it is a gluon. Supplementary to the input and output layer we use one "hidden" layer with 9 nodes, which have the task of building up an internal representation of the pattern to be learned. This NNw, shown in figure 3, was proposed in [1, 2] for studying e.g. the string effect. It should be noted that the NNw never sees the total structure of the event, just one single jet at a time is presented. Thus, even though we concentrate on 3-jet events here, the network could easily be applied to separate jets in multi-jet events[2].

A training set of 1381 3-jet events, using parton shower + DELSIM35 [7], was selected. The necessary information, i.e. the 4-momentum of the four leading particles, was written to two separate files; one for each type (quark/gluon) of jet. As there are twice as many quark as gluon jets in a 3-jet event, only the first half of the quark file was used in order to avoid suppression of the gluon learning. Defining one training *epoch* as when the NNw has seen the full training set, the training was interrupted after about 20-30 such epochs. No more improvements in the learning could then be seen.

[2]Then the training set should also contain jets from multi-jet events.

One problem using parton shower generated events is the ambiguity arising in the parton-jet assignment. A typical shower is illustrated in figure 4. It is likely that the gluon jet originates from the most energetic of the first two radiated gluons g_1 or g_2, for instance g_1. The three partons $(q', g_1, \overline{q})$ shall then be coupled to the tree jets (j_1, j_2, j_3) found by LUCLUS. One way to accomplish this is to simply use the angles between the jet and parton directions, see figure 4. However, it can be the case that two partons have the same closest jet. We avoid this problem by taking the parton-jet association given by the smallest of the following six sums:

$$\begin{aligned}
&\Theta_{q'j1} + \Theta_{g1j2} + \Theta_{\overline{q}j3} \\
&\Theta_{q'j2} + \Theta_{g1j3} + \Theta_{\overline{q}j1} \\
&\Theta_{q'j3} + \Theta_{g1j1} + \Theta_{\overline{q}j2} \\
&\Theta_{q'j1} + \Theta_{g1j3} + \Theta_{\overline{q}j2} \\
&\Theta_{q'j3} + \Theta_{g1j2} + \Theta_{\overline{q}j1} \\
&\Theta_{q'j2} + \Theta_{g1j1} + \Theta_{\overline{q}j3}
\end{aligned}$$

where $\Theta_{q'j1}, \ldots$ denotes the angle between q' and j_1 etc. .

The method described is by no means the only way to associate partons to jets nor do we claim it is the best but from figure 5 we conclude it works fairly well.

5 Results

The trained NNw was tested on 2608 3-jet events (PS+DELSIM35), which it had not seen before. The upper diagram of figure 6 shows the output value of the NNw for quark and gluon jets. From those distributions it is possible to deduce the efficiency (success rate) and purity of the jets selection, see lower diagram in figure 6. In [1, 2] the jet was interpreted as quark jet if the NNw output was < 0.5 else as a gluon jet. This "strict middle point" success condition would in our case give a large quark contamination of the selected gluons since the output distributions in figure 6 are slightly shifted towards 1. Quite arbitrarily we chose to interpret a jet as a gluon jet if NNw output > 0.82 and as a quark jet if the output is < 0.4, which gives an efficiency of about 40% for both types. All answers between 0.4 and 0.82 are taken to be undefined.

The NNw distinguishes gluon from quark jets on quantities such as E_{jet} and z, which are illustrated in the two next figures. The solid lines are the distributions where the original parton of the jet is known from the parton-jet association discussed in previous section. The dashed line in figure 7 shows the jet energy distribution of the jets selected by the NNw. It is clear that the jet energy is used to a large extent in the selection. The NNw has learned that the energy of the gluon jet is usually low and, to be on the safe side, it selects only the lowest energy jets. Although the NNw is trained with single jets, it is using the jet energy information since it has grown up in a world where $\sqrt{s} = 90$ GeV.

An interesting observation is the NNw sensitivity to the fragmentation function. The NNw has detected the harder fragmentation of the quarks. Jets containing particles with $z > 0.5$ are exclusively selected as quarks.

In general some care has to be taken when extracting physical results from the jets classified by a NNw; the input should not contain information of the quantities to be measured. Obviously E and z are used in the classification of our NNw and hence not very suitable for physics analysis. However, the string effect can be measured quite independently if the four leading particles are excluded, since the NNw classifies the jets without knowing the full structure of the event.

6 Conclusions

We have here a new tool for classifying jets. A neural network exploits all the differences it can find in the information shown to it. In particular for our application it recognizes the differences in jet energy and fragmentation between gluon and quark jets.

Though a similar performance might be achived with other methods, there are some predominant advantages with NNw. The simplicity of the method makes it an attractive alternative to some other efficient but intricate procedures. There are several existing programs for the handling of neural networks and writing one's own is not difficult. Once having a program, the training is practically automatic. The only interference from the user is when interpreting the output of the NNw. Diagrams like in figure 6 are then a good help. Another advantage is that the jets can be classified independently of the rest of the event. This is in contrary to the common method of ordering the jets in energy, whereby the kinematic of the whole event is used.

The particular NNw we have studied is probably not suitable for direct measurements of the fragmentation functions. On the other hand, since the NNw knows very little of the global event structure we think that the string effect could be measured in a new way. We aim to continue with such a study.

7 Acknowledgements

We wish to thank Carten Petterson, Leif Lönnblad and Thorsteinn Rögnvaldsson for introducing us to the concept of neural networks and their use in high energy physics and Torbjörn Sjöstrand for valuable help with the method of associating partons to jets. We would also like to thank Göran Jarlskog, Bengt Lörstad and Lars Jönsson for fruitful discussions and comments on the manuscript.

References

[1] L.Lönnblad, C.Peterson and T.Rögnvaldsson, **Finding Gluon Jets with a Neural Trigger**, *Physical Review Letters 65* (1990) 1321.

[2] L.Lönnblad, C.Peterson and T.Rögnvaldsson, **Using Neural Networks to Identify Jets**, *Nuclear Physics B349* (1991) 675.

[3] D.E.Rumelhart, G.E.Hinton and R.J.Williams, **Learning Internal Representation by Error Propagation** in D.E.Rumelhart and J.L.McClelland (Eds.) *Parallell Distributed Processing: Explorations in the Microstructure of Cognition (Vol. 1)*, MIT Press (1986).

[4] J.Dayhoff, *Neural Network Architectures: An Introduction*, Van Nostrand Reinhold(1990).

[5] The DELPHI collaboration, **Study of hadronic decays of the Z^0 boson**, *Physical Review Letters B240* (1990) 271.

[6] The AMY Collaboration, **The Physics of Jets Produced in Electron-Positron Collisions at Center of Mass Energies from 50 GeV to 56 GeV**, KEK Preprint 88-45, AMY 88-08, (1988).

[7] The DELPHI Collaboration, **DELSIM User's Guide**, DELPHI 89-67 PROG 142, 10 July 1989.

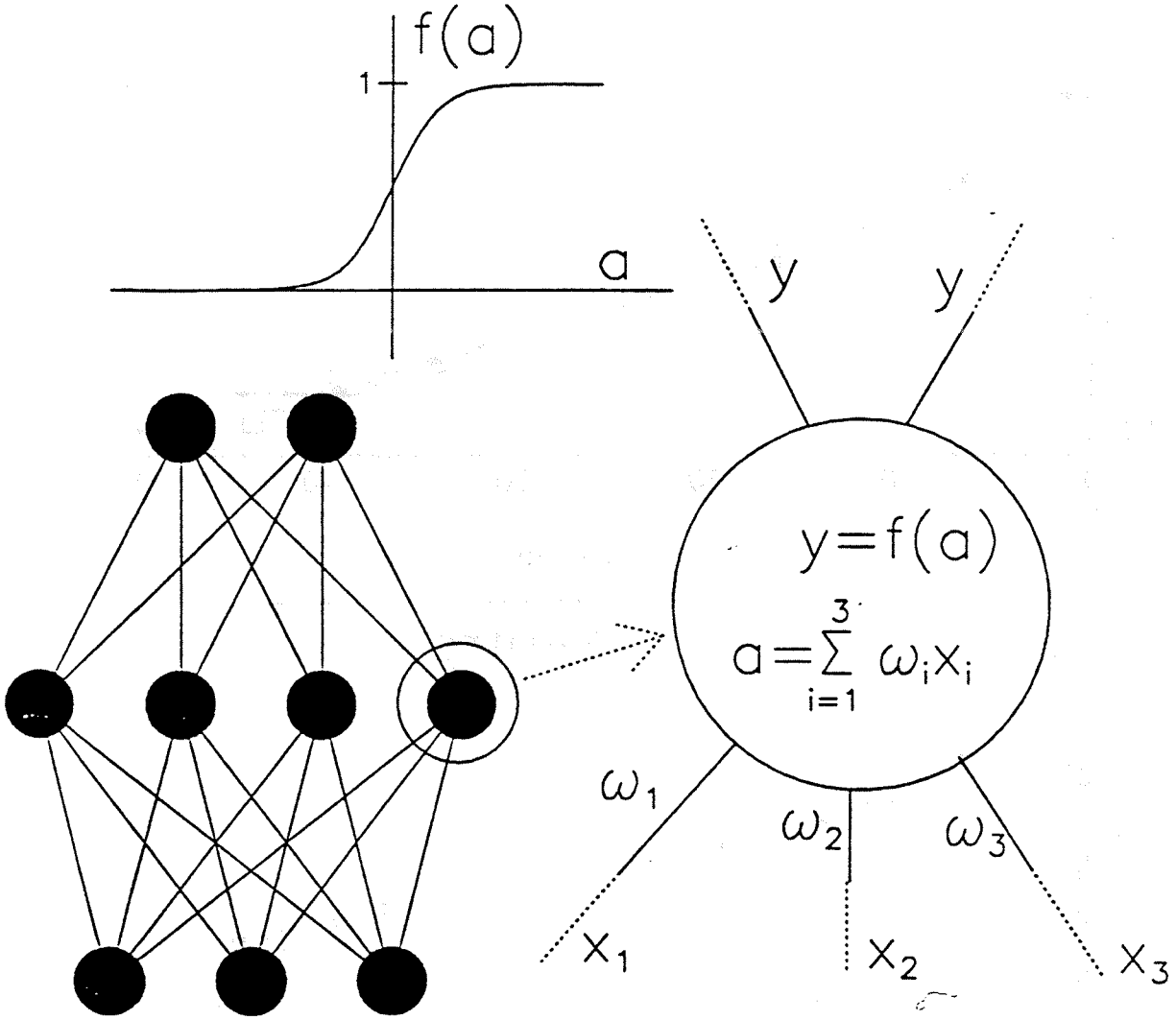

Figure 1: Neural network with 3 input, 4 hidden and 2 output neuron. To the right a magnified neuron is shown. The output of the neuron is a function f of the weighted sum of the input signals (x_1, x_2, x_3). In this paper f is a "sigmoid" function, which is depicted above the NNw.

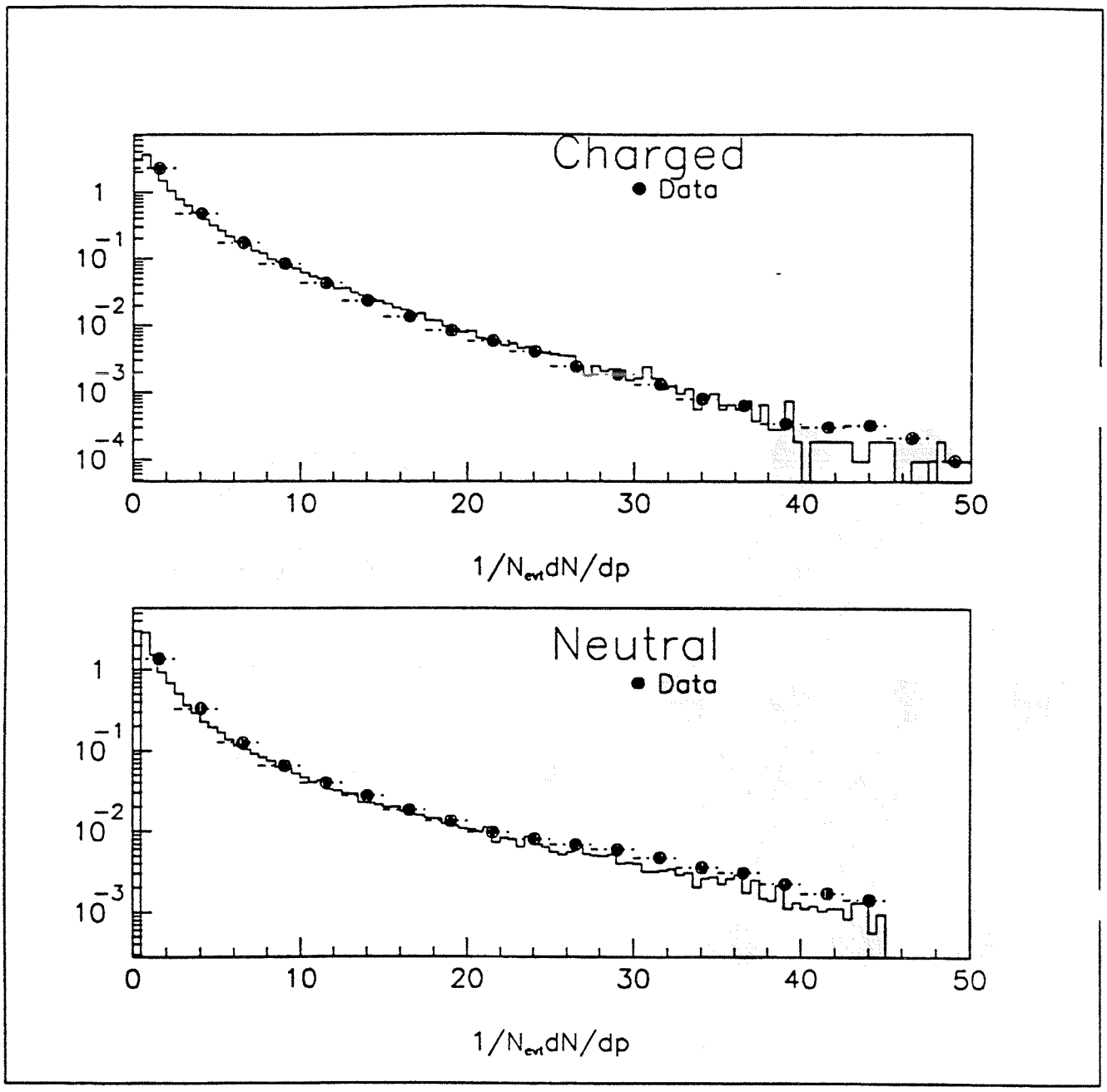

Figure 2: p distributions for charged and neutral particles. Comparison between data and Monte Carlo.

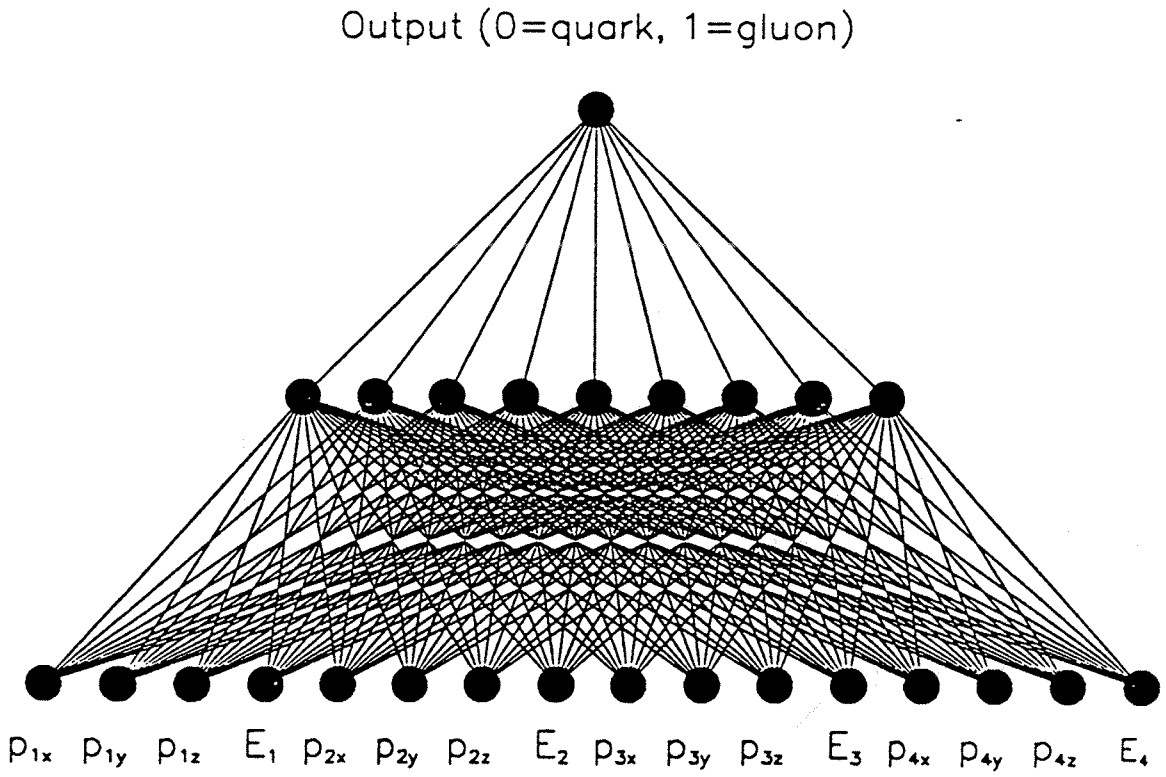

Figure 3: Neural network for quark/gluon classification. The four momentum vectors of the four leading particles are input to the NNw. The desired output values are "0" or "1" if the jet originates from a quark or a gluon respectively.

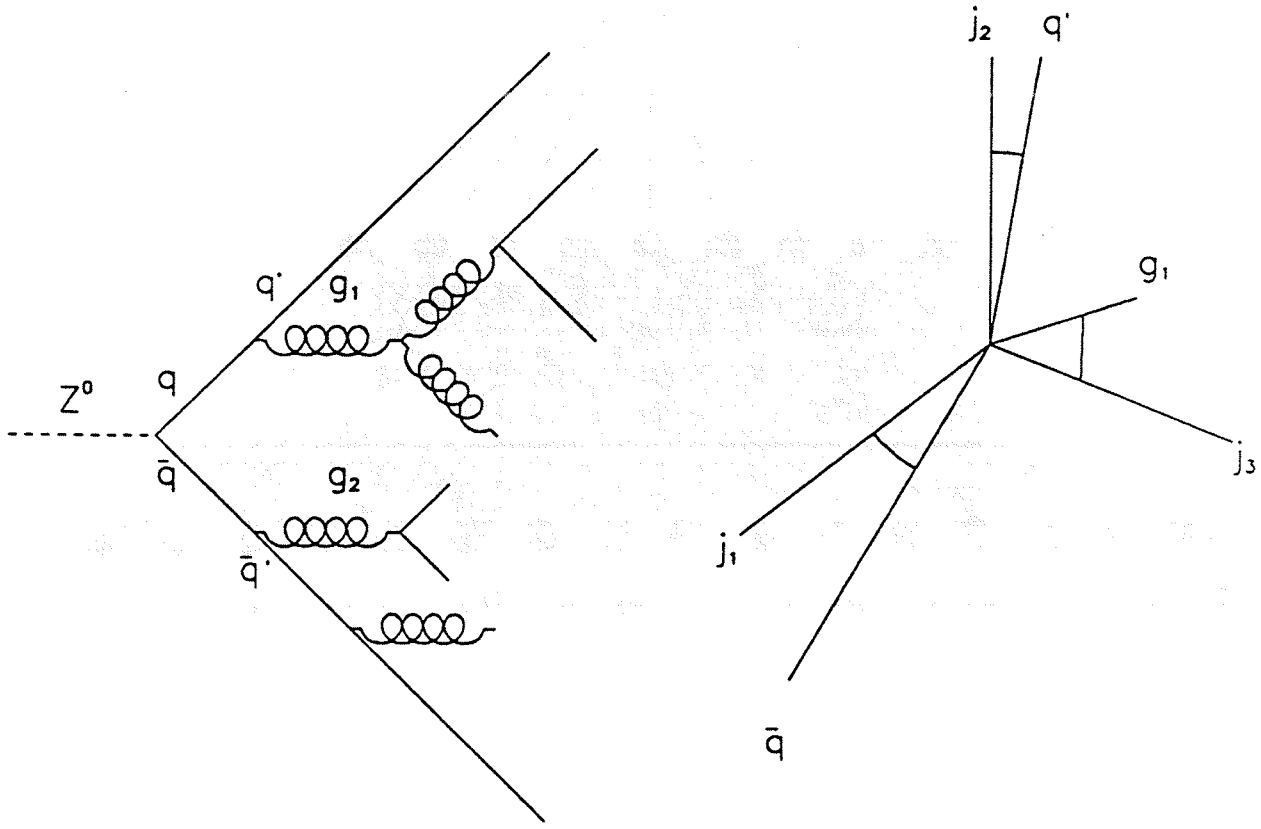

Figure 4: (Left) A cascade of a parton shower generated event. In the text it is assumed that $E_{g1} > E_{g2}$. (Right) The angles between partons and jets.

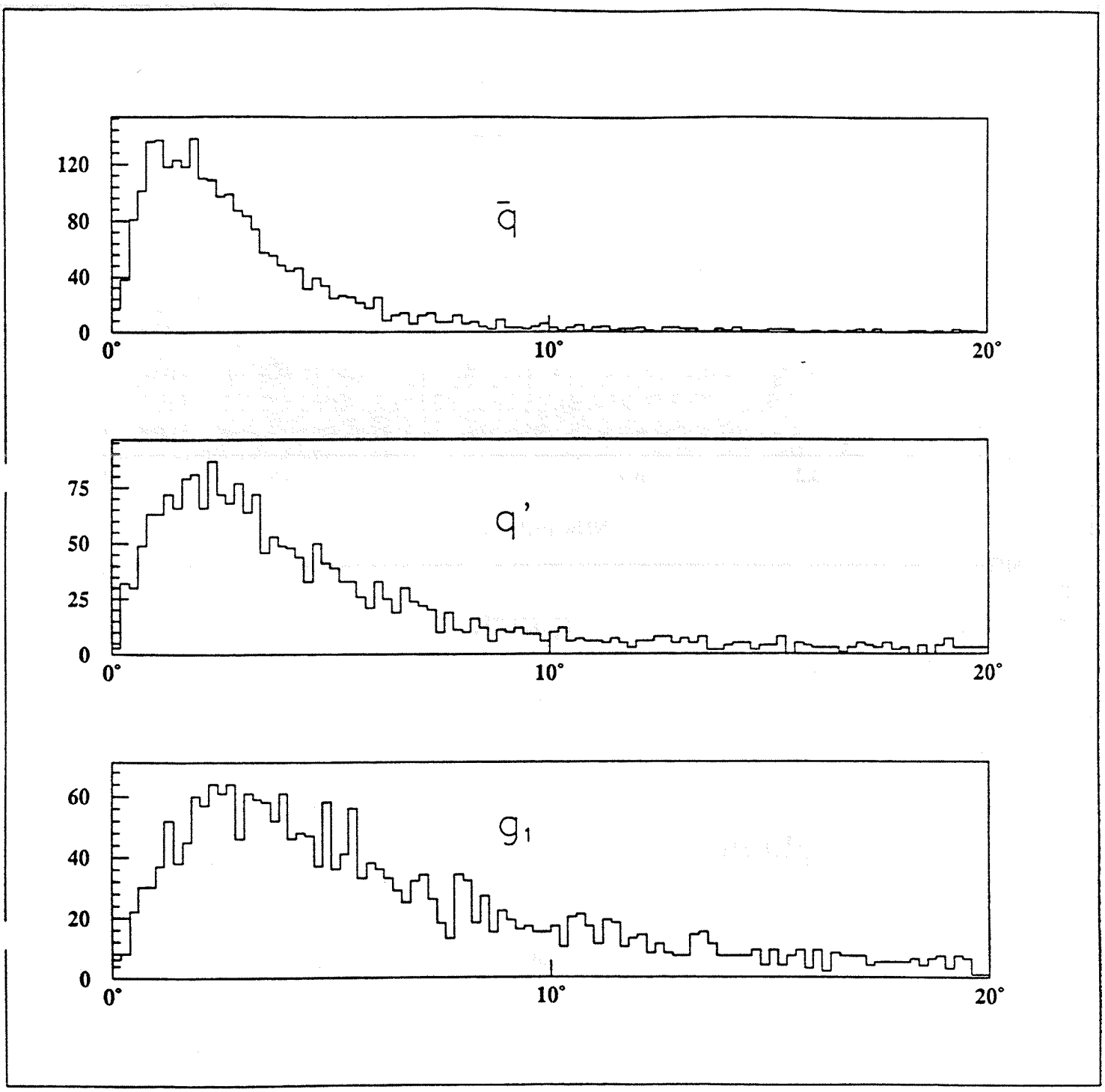

Figure 5: Parton-jet angles for the associated pairs.

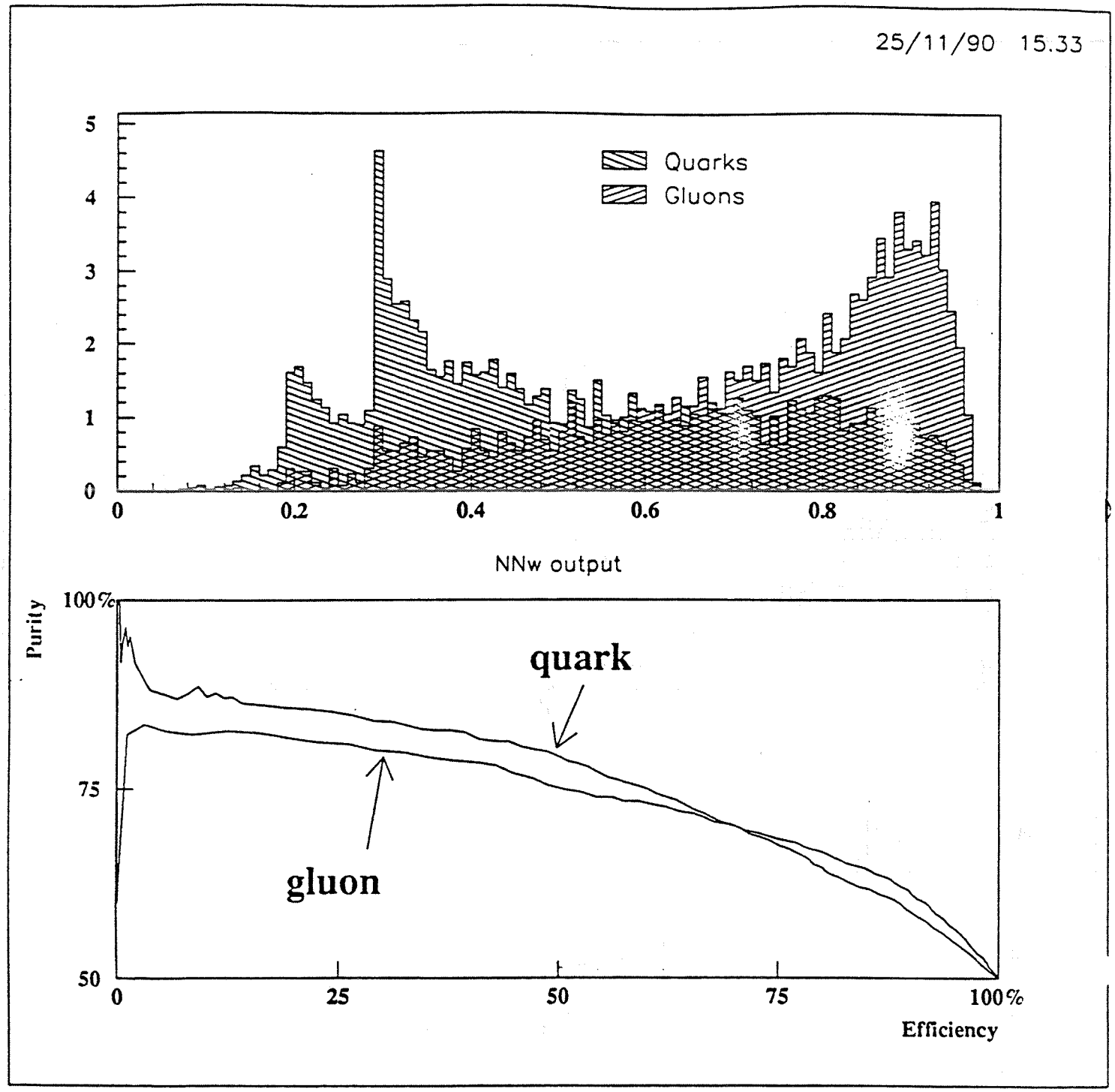

Figure 6: (Upper) The value on the NNw output node for quark and gluon jet input. (Lower) Efficiency purity deduced from the upper diagram.

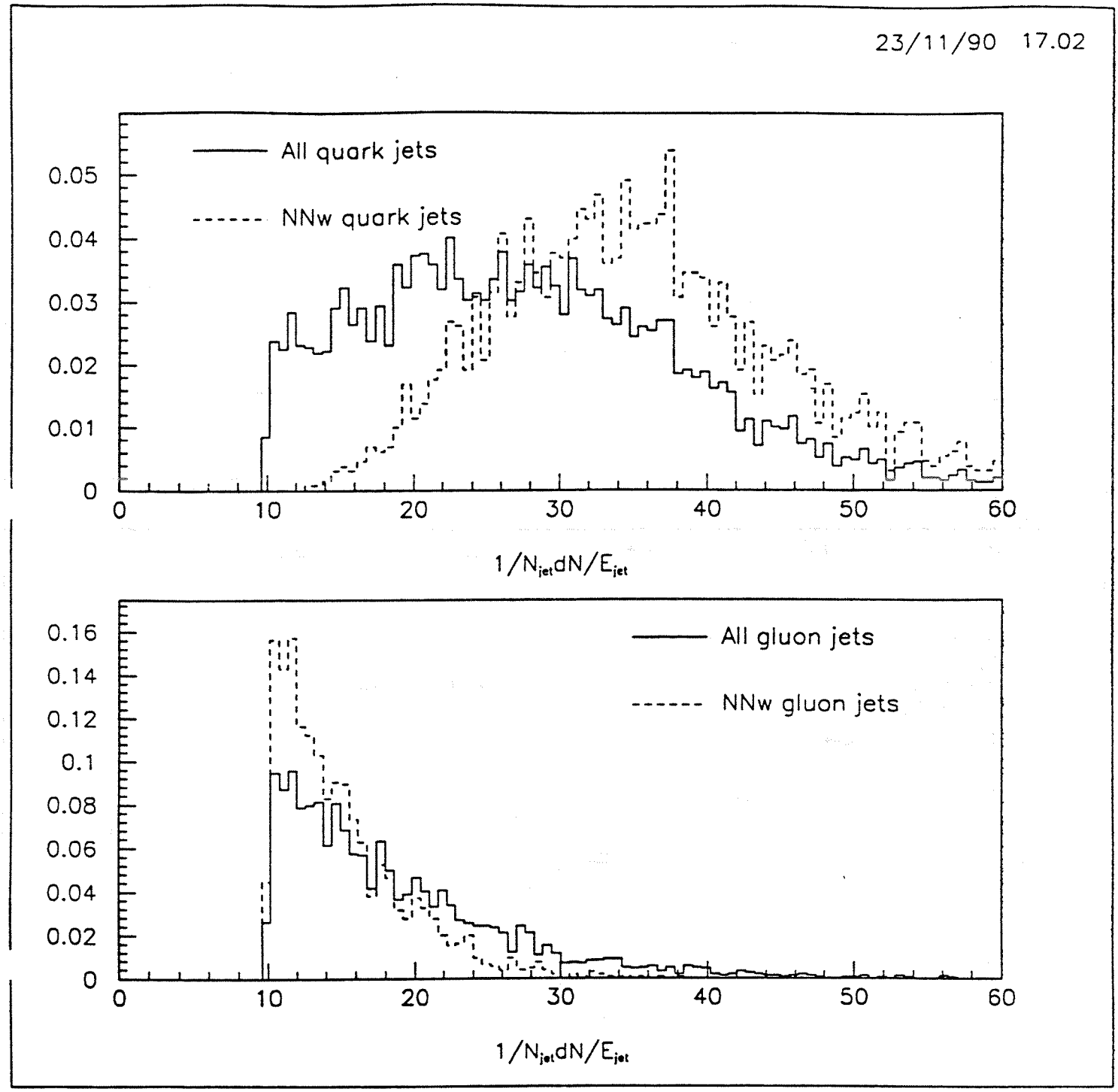

Figure 7: Jet energy distribution. The solid lines are the distributions where the original parton of the jet is known from the parton-jet association. The dashed lines are the jets selected by the neural network.

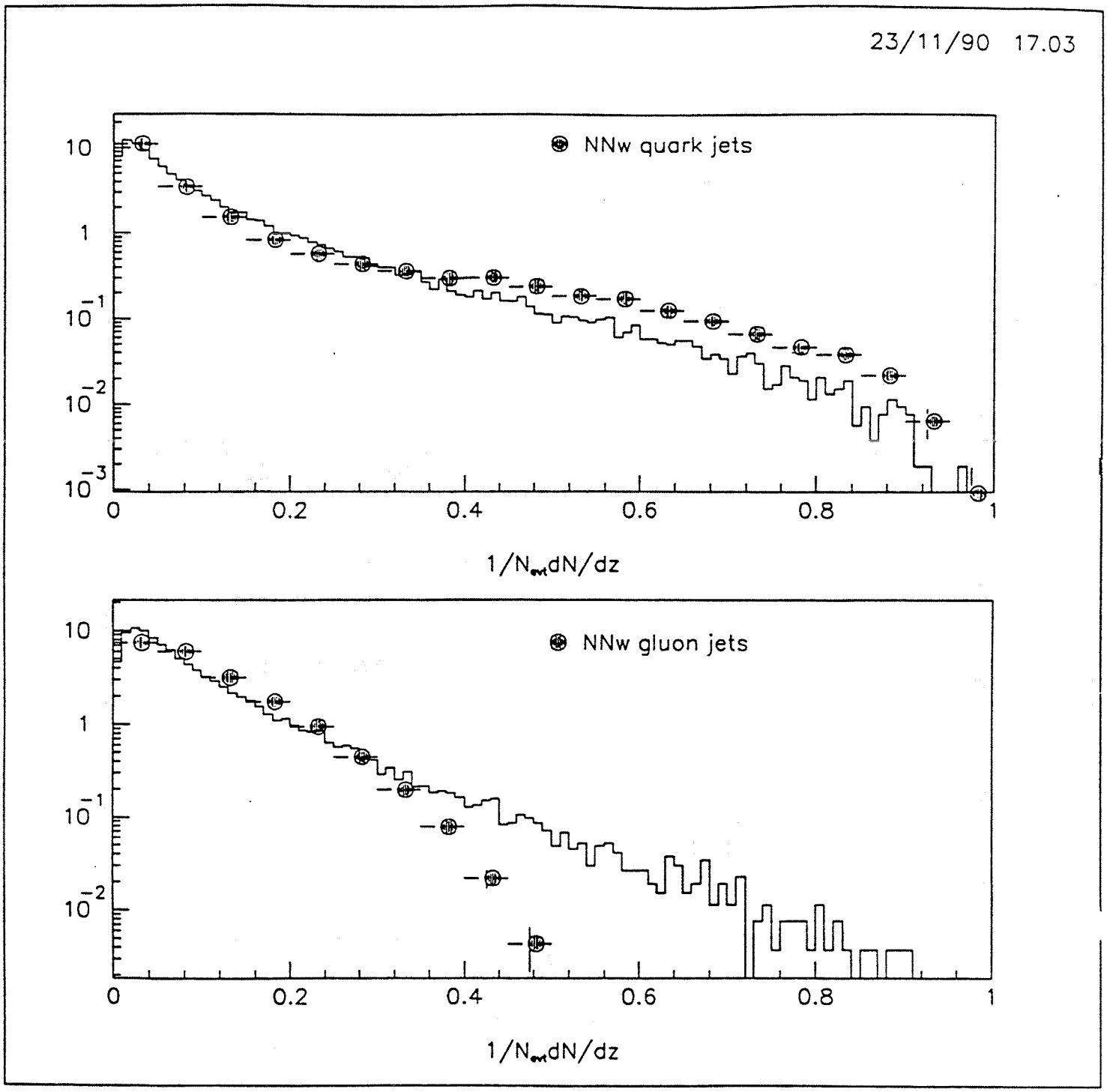

Figure 8: Fragmentation function of quarks and gluons. The solid lines are the distributions where the original parton of the jet is known from the parton-jet association. The dots are the jets selected by the neural network.

Appendix D

Quark/gluon jet classification with fragmentation sensitive variables

DELPHI Collaboration

DELPHI 92-70 PHYS 181
17 June 1992

Evidence for the Triple-Gluon Vertex from 4-Jet Events at LEP

DELPHI Collaboration

Paper submitted to the XXVI International Conference in High Energy Physics
DALLAS, Texas, USA, **August 5-12 1992**

DELPHI Collaboration

DELPHI 92-38 PHYS 170
19 March, 1992

Quark/gluon jet classification with fragmentation sensitive variables

O. Bärring

Abstract

As an alternative and/or complementary to the standard jet-energy classification of quark and gluon jets, we present a set of fragmentation sensitive variables. Neural network technique is applied to achieve optimal separation. The resulting efficiency and purity are at least as good as that of the standard method. Since the exact mechanism of fragmentation is not well understood, systematic effects coming from the Monte Carlo are expected and discussed. Finally the method is applied to real data giving a qualitative feeling of its performance.

Quark/gluon jet classification with fragmentation sensitive variables

O.Bärring

Abstract

As an alternative and/or complementary to the standard jet-energy classification of quark and gluon jets, we present a set of fragmentation sensitive variables. Neural network technique is applied to achieve optimal separation. The resulting efficiency and purity are at least as good as that of the standard method. Since the exact mechanism of fragmentation is not well understood, systematic effects coming from the Monte Carlo are expected and discussed. Finally the method is applied to real data giving a qualitative feeling of its performance.

1 Introduction

Many interresting experimental tests of QCD require at least a fair knowledge of the parton origin of a hadronic jet. In some cases, e.g. measurement of the string effect in 3-jet events or the gluon-gluon coupling in multijet events, it is sufficient to distinguish gluon from quark jets, whereas in e.g. heavy quark physics it is also necessary to know the flavour of the quarks. It is a paradox that the latter case turns out to be the simpler in the sens that it is possible to reach high purity. In fact, with the rapidly increasing amount of Z^0 events at LEP it has been proposed [1, 2, 3] that at least one of the quark jets in 3 or 4 jet events, can be tagged from the semileptonic decay of heavy quarks. Thus, the certainty of assigning the gluon jet is highly improved. Such an analysis has already been carried out by the OPAL collaboration [3].

This paper reviews a set of variables sensitive to the fragmentation differences between quarks and gluons. Possible differences between the quark flavours will not be treated here. Evidently the variables are not suitable for measuring fragmentation dependent effects like the string effect. However, they are appropriate for measuring "hard" QCD e.g. the triple gluon vertex in 4-jet events. The variables are introduced in the next section together with a brief description of the neural network. The resulting performance on Monte Carlo and data is discussed in the following section. The sensitivity to variations in the Monte Carlo description of fragmentation is considered in the last section.

2 Classification Variables

We aim to find variables which are sensitive to the fragmentation and completely independent of the jet-energy. Thus, two uncorrelated classifications are possible simultaneously with variables from "hard" (jet-energy) and "soft" QCD (fragmentation variables) respectively. Whenever a high efficiency-purity is needed the two methods can of course be combined.

In [1] the following moments were suggested:

$$M_{nm}(E_j) = \sum (\frac{p_t}{E_j})^n \eta^m \tag{1}$$

where the sum is taken over all particles assigned to the jet. p_t and η are the transverse momentum and pseudo rapidity of the particle with respect to the jet-axis. E_j is the jet energy. As pointed out by [1] these moments are sensitive to the softer fragmentation, higher multiplicity and broader p_t of the gluon jets as compared to the quark jets. An analysis of the first 7×7 moments concluded that M_{10}, M_{11}, M_{14}, M_{15}, M_{16}, M_{25}, M_{26} and M_{27}, depicted in Figure 1, give best separation between quark and gluon jets. In Figure 1 the jet-energy dependence of some moments is quite significant; larger than the separation between the two curves, implying a selection on energy rather than fragmentation. This is because quarks (gluons) are more likely to populate the high (low) jet-energy region. A neural network would certainly benefit from such information unless a training sample is prepared with quark and gluon jets equally distributed in jet energy. Here we present a different strategy.

Since the energy dependence of the average moments, $\overline{M_{nm}(E_j)}$, is about the same for quark and gluon jets (the curves in Figure 1 are nearly parallel), it can be divided out. Formally a set of new variables is defined:

$$F_{nm}^{(q,g)}(E_j) = \frac{M_{nm}^{(q,g)}(E_j)}{(\overline{M_{nm}^{q}}(E_j) + \overline{M_{nm}^{g}}(E_j))/2} \tag{2}$$

where the superfixes q, g denote quark and gluon respectively. As expected, the separation between $F_{nm}^{q}(E_j)$ and $F_{nm}^{g}(E_j)$ is larger than their E_j dependence, see Figure 2.

Two samples of a few thousand JETSET 7.2 parton shower + detector simulated events are prepared for the neural network (NNw). One sample is used for training and the other for testing the generalizability of the NNw. Hadronic events are selected according to the standard DELPHI cuts [5]. In addition we use neutral particles in $0.5 \leq E \leq 45$ (GeV). The jet search algorithm LUCLUS [6] defines our jets with the resolution parameter $djoin = 4$ (GeV). In order to have reasonable statistics in the sum (eq. 1) a jet is required to have a minimum multiplicity of 4 particles and a measured energy of at least 7 GeV. We restrict our analysis to three and four jet events.

The parton ancestor of a jet is decided in same way as in [4]: by varying the resolution parameter (d_{join} or y_{cut}), the number of jets at parton level is forced to be the same as the number of jets found in the detector. The parton jets are assigned to the hadron jets using the same distance measure as the jet clustering algorithm (p_t or invariant mass). Parton jets containing an odd number of quarks are assigned as quark jets and all the others as gluon jets. Thus, a quark jet contains either a primary quark or a resolved secondary quark + possible unresolved quark pairs from $g \rightarrow q\bar{q}$. This procedure works unambiguously on more than 96% of the 3 and 4-jet events.

The NNw together with its output distribution on the test sample are shown in Figure 3. The target values are 0 for a quark and 1 for a gluon jet.

3 Results

Using the obvious condition of having only one gluon jet in 3-jet events, the NNw gives a correct answer with 70% probability for the gluon. The jet with a NNw output closest to the quark target value is to 91% a quark jet. The second quark jet is correctly identified in 76% of the cases. A similar exercise on 4-jet events – assigning the jet with a NNW output closest to the quark target value as a quark jet, the second also as a quark, the third and fourth as gluon jets – yields 82%, 63%, 60% and 72% respectively. The 5-10% background from $q\bar{q}q\bar{q}$ events is neglected. In 3-jet events, the least energetic jet has 67% probability of being a gluon jet and the leading and second leading jets are of quark origin to 94% and 71% respectively. Thus,

Method	q_1	q_2	g
E_{jet}	94%	71%	67%
NNw	91%	76%	70%
NNw $+E_{jet}$	94%	77%	72%

Table 1: Jet identification purities in 3-jet events. q_1 and q_2 are the leading and second quark respectively.

the classification with the fragmentation sensitive variables presented in the previous section works slightly better than the jet-energy method for the gluon and second quark jet whereas the leading quark is better identified using the latter method. Table 1 summarizes the classification capabilities of the two methods. As expected one gains a few percent by adding the jet energy as an extra input node to the NNw.

As a test on real data we choose to study angular distributions in 4-jet events. Since the jet type is identified from fragmentation differences only, jet orientations can be expected to be measured in an unbiased way. Note that the intention is not to give quantitative conclusions on the non-abelian structure of QCD. The qualitative agreement between data and theory merely serves as an indirect evidence of that the jet classification works.

To believe any result at all from this analysis it is necessary to check that data and Monte Carlo show a reasonable agreement on the moments (eq. 1). That this is indeed the case can be seen from Figure 4.

An essential feature of QCD is the existence of the gluon self-coupling. In e^+e^- annihilation the triple-gluon vertex enters in second and higher orders of the strong coupling constant. A direct consequence of the triple-gluon vertex is the smallness of the ratio $q\bar{q}q'\bar{q}'$ over $q\bar{q}gg$ final states in 4-jet events. This is due to more colour combinations for octet gluons than the triplet quarks as well as the bremsstrahlung characteristics in $g \rightarrow gg$ in contrast to the splitting $g \rightarrow q\bar{q}$ [2].

Several more or less elaborate observables for measuring angular correlations in 4-jet events have been proposed [7]. The two angles Θ_{NR} and α_{34}, shown in Figure 5, were used in a nice study [8] to extract $\frac{N_c}{C_f}$ and $\frac{T_R}{C_f}$, which are of fundamental importance to QCD. The (generalized) Nachtmann-Reiter angle, Θ_{NR}, is essentially the angle between the vectors $(\mathbf{p_1} - \mathbf{p_2})$ and $(\mathbf{p_3} - \mathbf{p_4})$ where $(\mathbf{p_1}, \mathbf{p_2})$ and $(\mathbf{p_3}, \mathbf{p_4})$ are the momentum vectors of the primary $q\bar{q}$ and the secondary partons respectively. α_{34} is the angle between the secondary partons. We take the two jets with the most "quark like" NNw response, i.e. closest to the quark target value 0, as the primary $q\bar{q}$. As in [8] we conclude from Figure 5 that the data is better described by QCD than the Abelian theory. The χ^2 values for $|cos\Theta_{NR}|$ and $cos\alpha_{34}$ are 4.8 and 2.7 (10 bins) respectively for QCD compared to 19.8 and 6.6 for the abelian theory. From $|cos\Theta_{NR}|$ alone we can exclude the abelian theory to more than 97% confidence level. Inversely, if QCD is believed to be the correct theory, the agreement with data indicates that our jet identification indeed has more into it than just being a fancy way to extract physics out of nothing.

Diagram	JETSET 7.2 param.	Value (D)	Comments
1	PARJ(41)	0.15 (0.20)	"a" in the symmetric Lund
2		0.25 (0.20)	fragmentation function.
3	PARJ(82)	0.9 (1.0)	The invariant mass cutoff
4		1.5 (1.0)	of parton showers.
5	PARJ(21)	0.3 (0.4)	Width in the Gaussian
6		0.5 (0.4)	transverse momentum distr. for primary hadrons.
7	JETSET Matrix Element + string fragm. (ME)		
8	JETSET Independent Fragmentation (IF)		

Table 2: JETSET parton shower parameter values corresponding to the diagram pairs in Figure 6. The values in parenthesis are the DELPHI tuning for those parameters.

4 Sensitivity to the fragmentation description

Exact theoretical calculations of the parton cascade and the hadronisation are not likely to appear within the nearest future. Thus, a phenomenological description is needed for the calculation of the observables (eq. 2). Even though the JETSET parton shower + string fragmentation does well describe the data for quarks and gluons together in Figure 4, this is not necessary true for the two classes separately. Ways out of this model dependence have been proposed [1] using the fact that two jet events in e^+e^- contain quark jets only. However, in order to extract the energy dependence of the moments (eq. 1) this requires several experiments at different centre of mass energies. No such data is available. Another possibility would be to tag quark jets from the semileptonic decay of heavy quarks in three jet events. In this paper we limit ourselves to study the variation of the NNw response on test samples from different Monte Carlos.

A NNw was trained on JETSET parton shower + string fragmentation (PS) 4 jet events with the DELPHI tuning [9]. No detector simulation was used for this study. In Figure 6 the NNw performance is presented as efficiency-purity plots for quark (left) and gluon (right) jets. The solid lines represent the response for a test sample with the same tuning as the training sample. In the first 6 diagram pairs some of the most important PS parameters influencing the fragmentation have been varied up to about 50%, see Table 2. The only significant deviation is found in 3 where the invariant mass cutoff of parton showers, m_{min}, equals 0.9 GeV. This parameter, PARJ(82) in JETSET 7.2, is close to its limit value of 2*PARJ(81)=0.8 GeV, below which α_s may become infinite.

The matrix element (ME) option of JETSET, diagram 7, has a similar NNw response as PS. The method, proposed in section 3, of assigning the two most quark like jets as of quark ancestors and the other two as gluon jets does not show any discrepancy between ME and PS nor does the jet-energy ordering, see Table 3. We can be confident that with respect to different Monte Carlo models, the systematic errors in the 4-jet analysis of previous section are of the same size as if the jet energy classification method had been used instead.

The JETSET independent fragmentation (IF), diagram 8 and Table 3, has significantly different NNw output distributions. Despite that the best DELPHI tuning [9] has been used, it is

	PS		ME		IF	
Jet	E_jet	NNw	E_jet	NNw	E_jet	NNw
q_1	81%	81%	79%	82%	79%	76%
q_2	62%	63%	61%	63%	60%	61%
g_1	59%	61%	60%	62%	60%	59%
g_2	71%	71%	69%	71%	70%	69%

Table 3: Jet identification probability in 4-jet events. q_1 is the most quark like jet and g_2 the most gluon like jet. The NNw was trained on PS events.

not very surprising that there are such differences since IF usually fails to describe fragmentation dependent effects, e.g. the "string effect". The jet-energy ordering does not show the same degeneration in performance, Table 3, because the partons are generated according to the ME scheme and hence their energies are still correctly described.

5 Conclusions

It has been shown how to construct jet-energy independent variables that exploit the fragmentation differences between quarks and gluons. Jet classification with those observables gives about the same performance as the commonly used jet-energy ordering. There is no significant increase in the performance when combining the two methods.

As an example of application on real data a four jet analysis measuring the triple-gluon vertex has been carried out. Data clearly prefers QCD to an Abelian theory, which is excluded to more than 97% confidence level.

The method is insensitive to 50% variations in some of the fragmentation parameters of the Lund string model. A significantly worse performance on "independent fragmentation" generated data can be seen. However, ordering the jets within e.g. 4-jet events so that the two most quark like jets are assigned as quarks and the rest as gluons, turns out to be rather insensitive to variations in the Monte Carlo.

6 Acknowledgement

Many of the ideas in this paper have been developed together with Dr. T.Åkesson.

7 Figure captions.

Figure 1 The jet-energy dependence of the average value of the moments (eq. 1) in 4-jet events. The jet-energy is calculated from angular constraints.

Figure 2 The moments in Figure 1 after the jet-energy dependence has been divided out (eq. 2).

Figure 3 Uppermost: the NNw response on the test sample. Below: the NNw layout. The line width is proportional to the weight size. The target values for the output node are 0 for

a quark jet and 1 for a gluon jet.

Figure 4 The jet-energy dependence of the moments (eq. 1) for 1990 DELPHI data and Monte Carlo (q and g together).

Figure 5a The generalized Nachtmann-Reiter angle distribution for data and Monte Carlo. The data is corrected for detector inefficiencies and the errors have been correspondingly propagated.

Figure 5b The secondary parton's opening angle, α_{34}, distribution for data and Monte Carlo. The data is corrected for detector inefficiencies and the errors have been correspondingly propagated.

Figure 6 a and b The NNw response for different Monte Carlos and tunings. The left (right) diagram in each pair corresponds to the quark (gluon) efficiency-purity function. Solid line is the DELPHI PS default tuning. Diagram 1-6 have different JETSET PS tunings, diagram 7 and 8 are JETSET ME and IF respectively (cf. Table 2).

References

[1] See for instance: Z.Fodor, ITP Budapest Report No.465 (1988); Z.Fodor, invited talk at the Triangle Meeting on Particle Physics, Vienna 1989, Preprint UWThPh-1989-64; Z.Fodor, Phys. Lett. B263 (1991) 305-310.

[2] S.Bethke, A.Ricker, P.M.Zerwas, Z.Phys. C49 (1991) 59-72.

[3] M.Z.Akrawy et al. OPAL Coll., Phys. Lett. B261 (1991) 334-346.

[4] L.Lönnblad, C.Peterson and T.Röngvaldsson, Phys. Rev. Lett. 65 (1990) 1321; Nucl. Phys. B349 (1991) 675.

[5] DELPHI Collab., P.Aarnio et al., Phys. Lett. B240 (1990) 271.

[6] T.Sjöstrand, Comput. Phys. Commun. 28 (1983) 229.

[7] J.G.Körner, G.Schierholz and J.Willrodt, Nucl. Phys. B185 (1981) 365; O.Nachtmann and A.Reiter, Z.Phys. C16 (1982) 45; M.Bengtsson and P.M.Zerwas, Phys. Lett. B208 (1988) 306.

[8] DELPHI Collab., P.Abreu et al., Phys. Lett. B255 (1991) 466.

[9] DELPHI Collab., Comparison of DELPHI data with QCD models, Contribution to the Geneva EPS-LP'91 Conference, DELPHI note 91-74 (1991), unpublished.

Figure 1

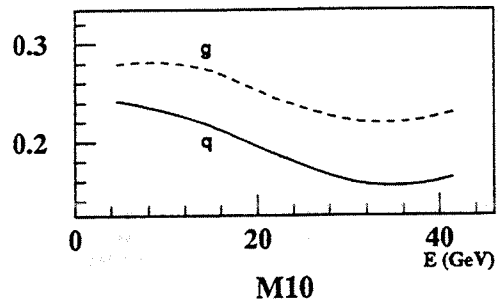

M10

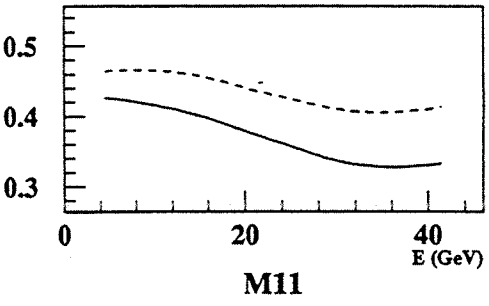

M11

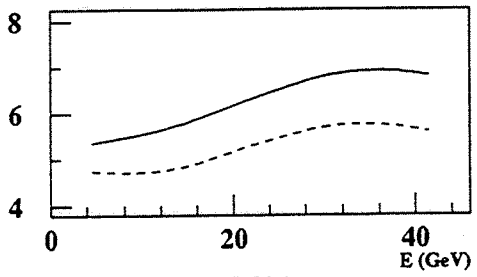

M14

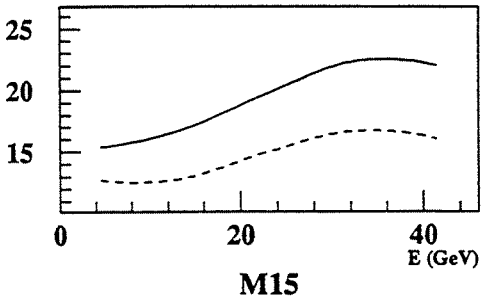

M15

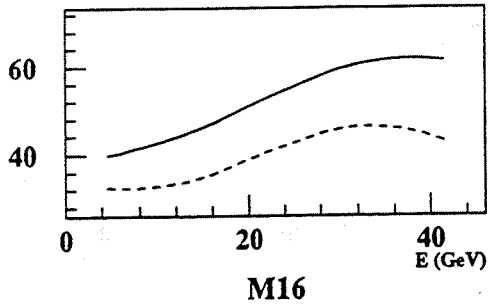

M16

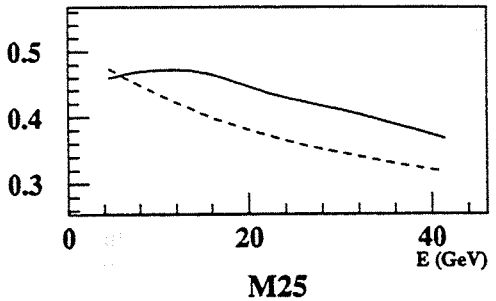

M25

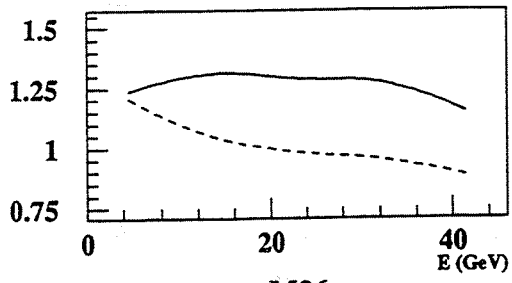

M26

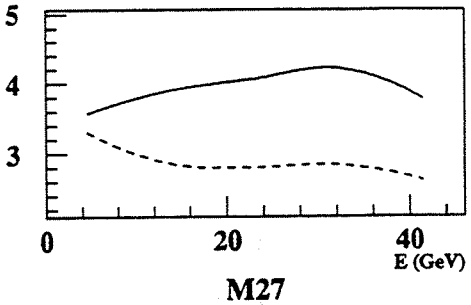

M27

Figure 2

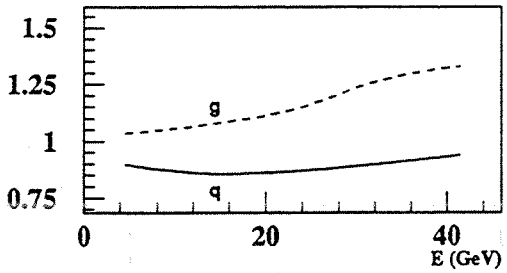

F10

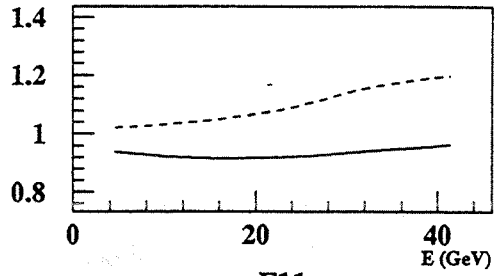

F11

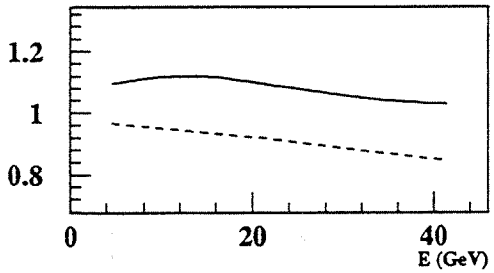

F14

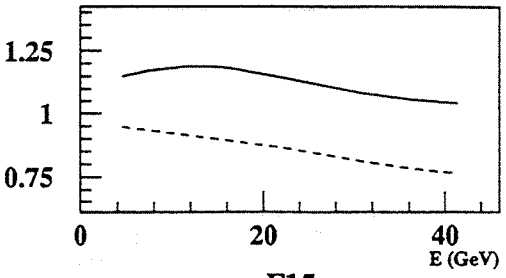

F15

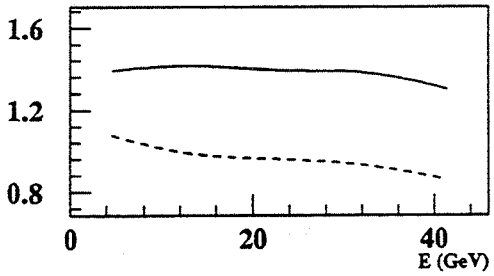

F16

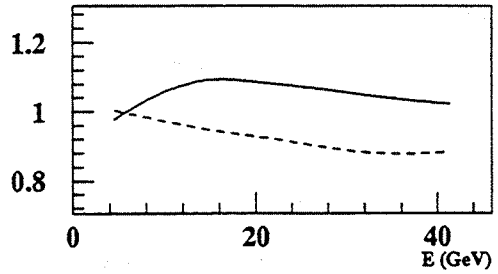

F25

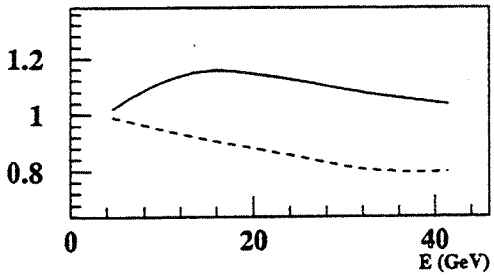

F26

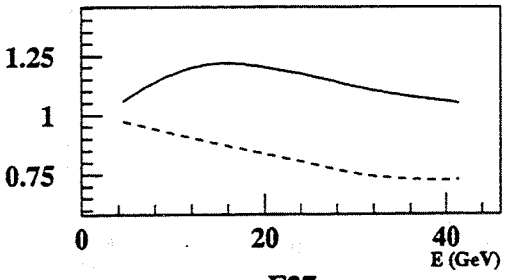

F27

Figure 3

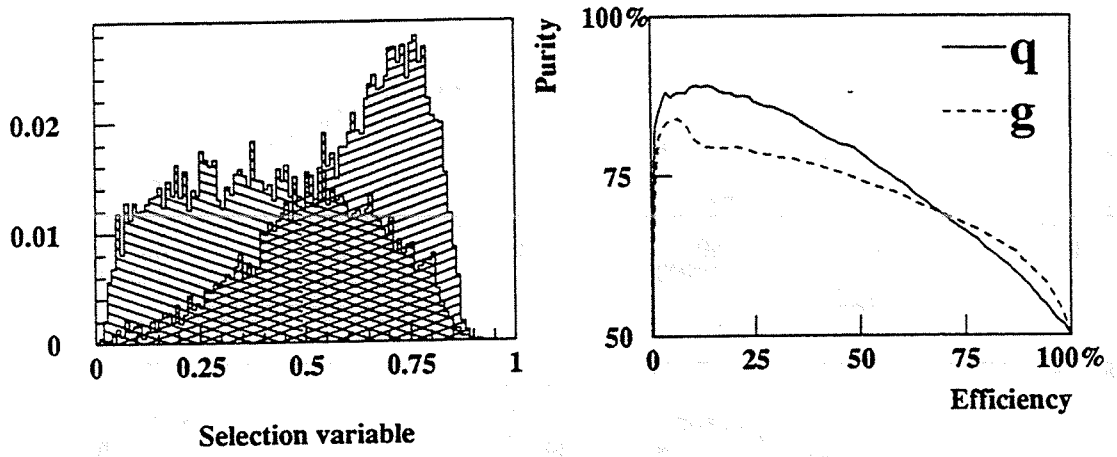

Output target values: 0=q, 1=g

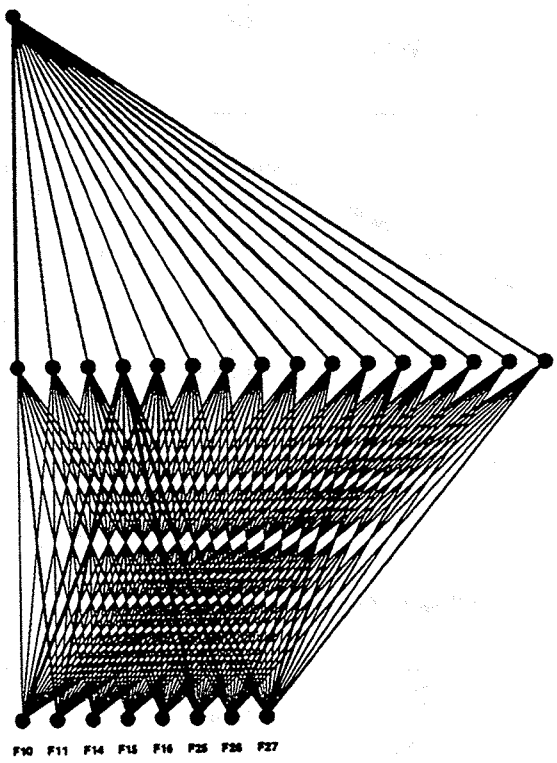

Figure 4

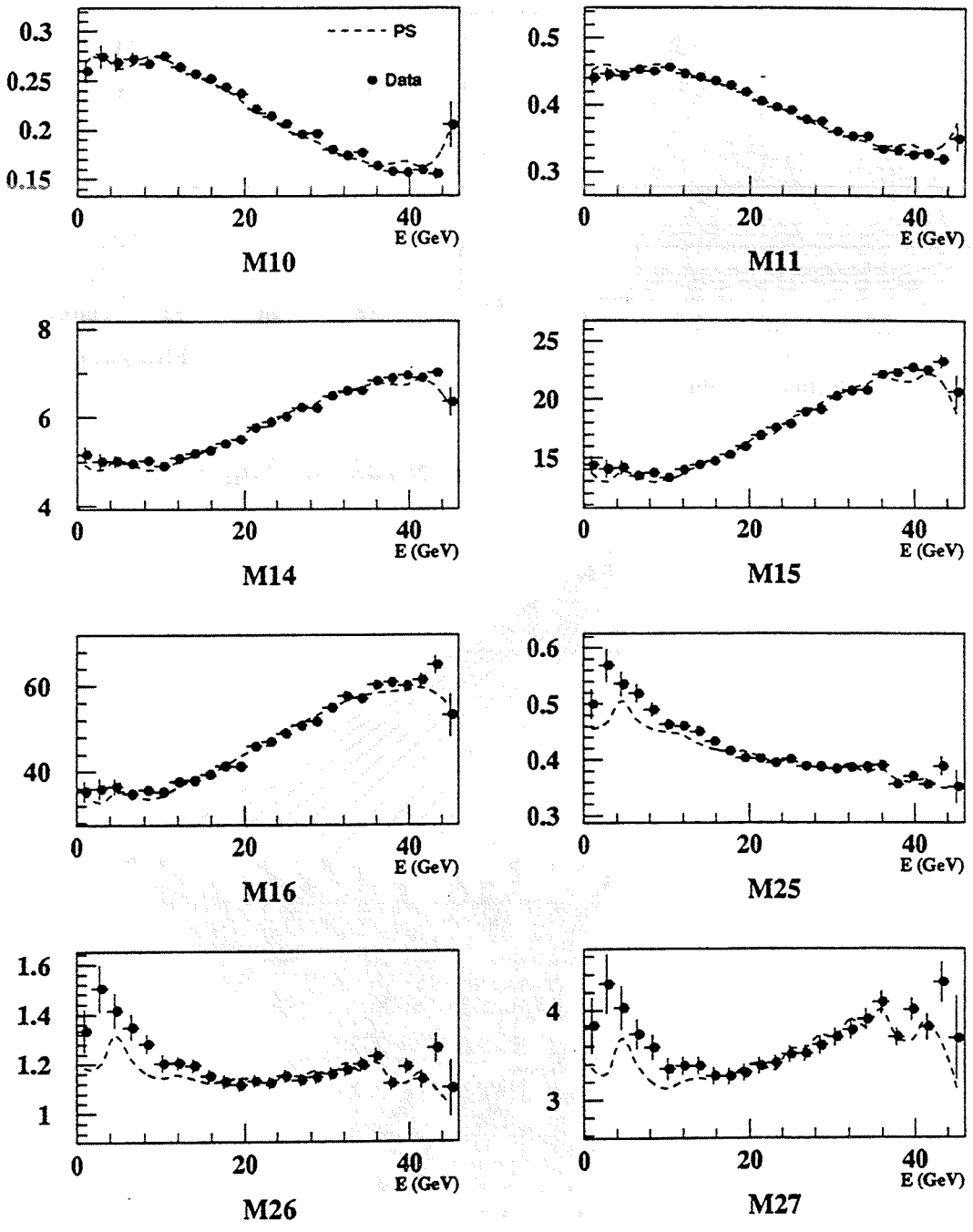
PS
Data
0.3
0.25
0.2
0.15
0
20
40
E (GeV)
M10
0.5
0.4
0.3
M11
8
6
4
M14
25
20
15
M15
60
40
M16
0.6
0.5
0.4
0.3
M25
1.6
1.4
1.2
1
M26
4
3
M27

Figure 5a

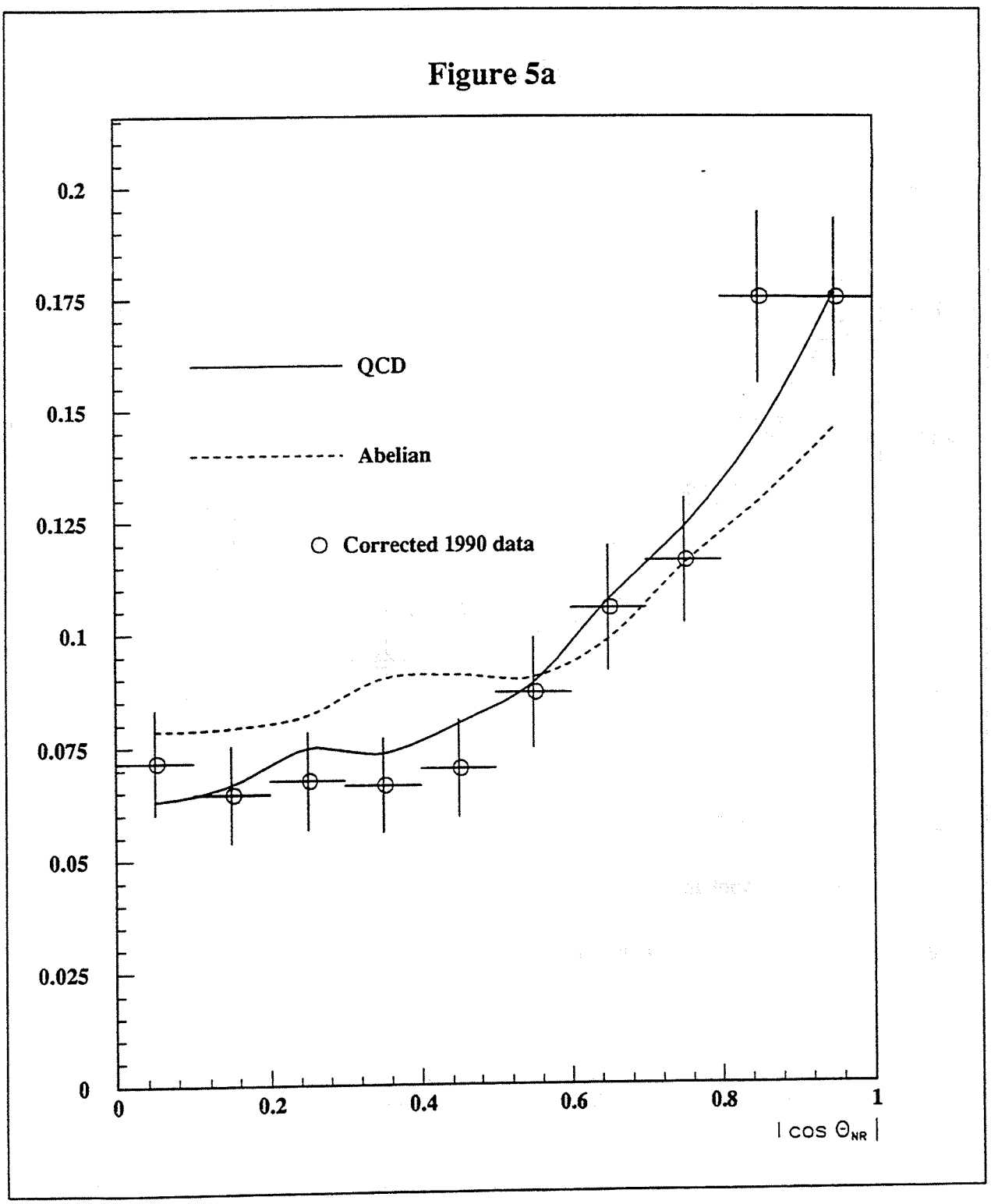
0.2
0.175
0.15
0.125
0.1
0.075
0.05
0.025
0
0
0.2
0.4
0.6
0.8
1
| cos Θ_NR |
QCD
Abelian
Corrected 1990 data

Figure 5b

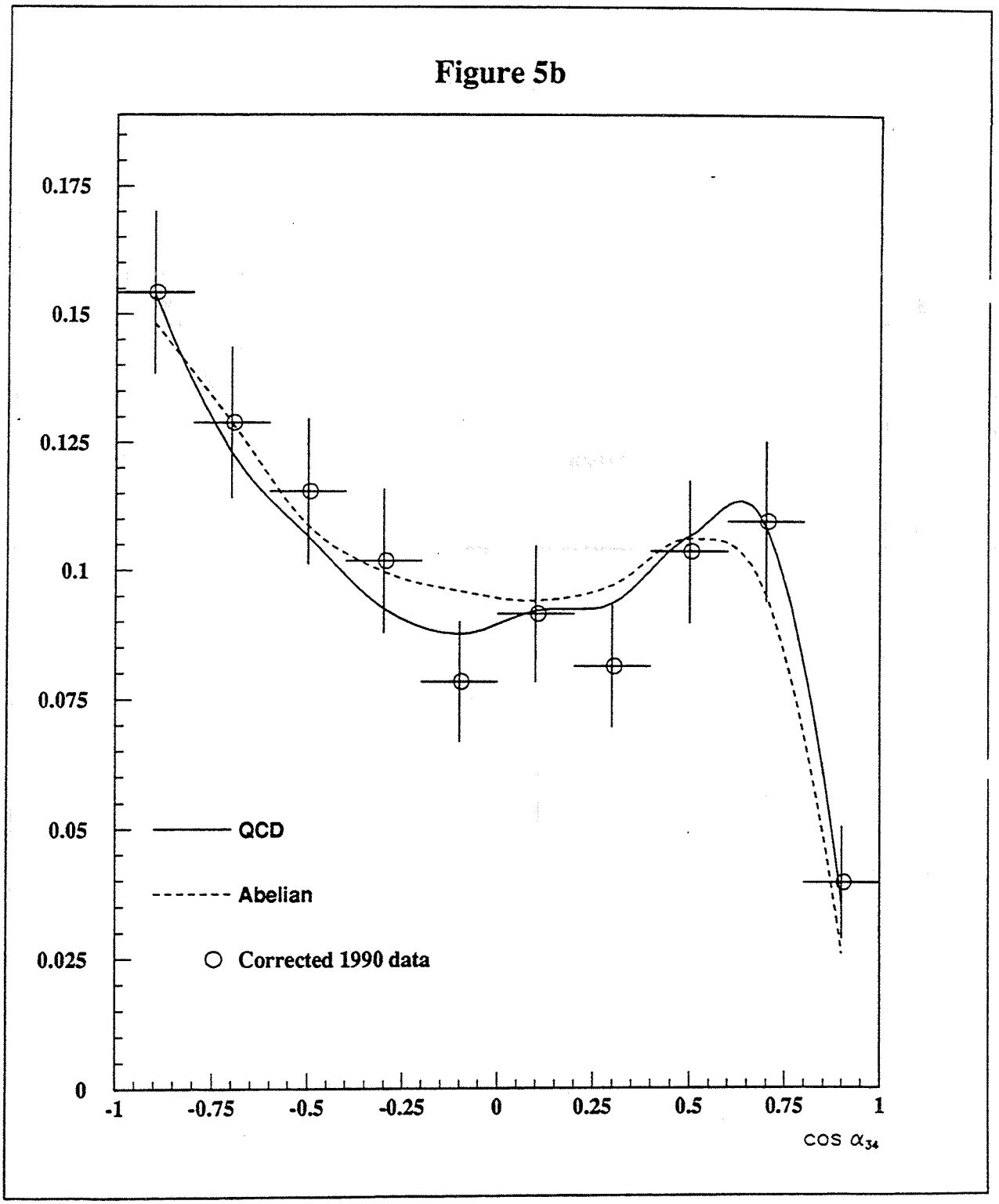
0.175
0.15
0.125
0.1
0.075
0.05
0.025
0
-1
-0.75
-0.5
-0.25
0
0.25
0.5
0.75
1
cos α_{34}
QCD
Abelian
Corrected 1990 data

Figure 6a

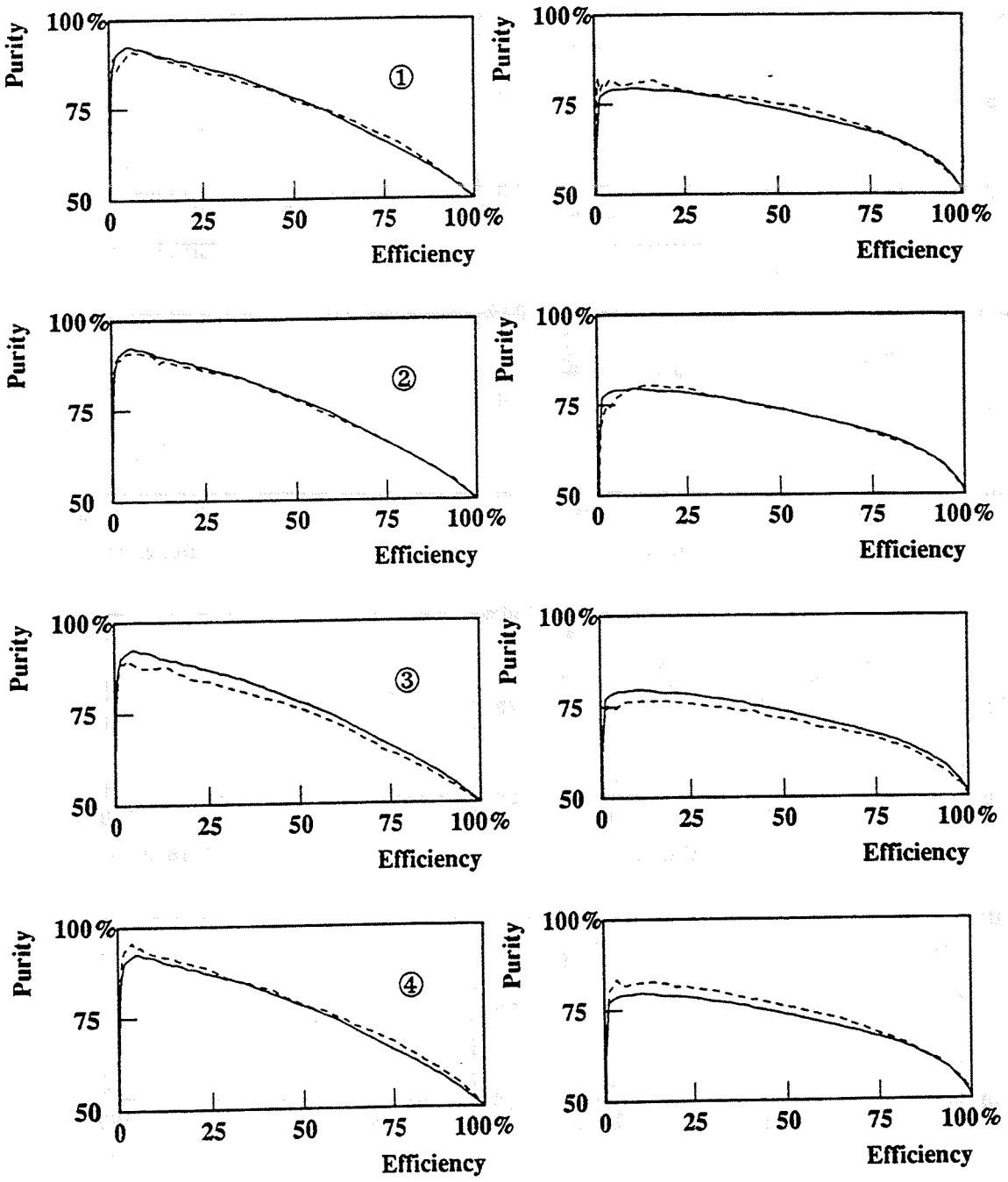

Figure 6b

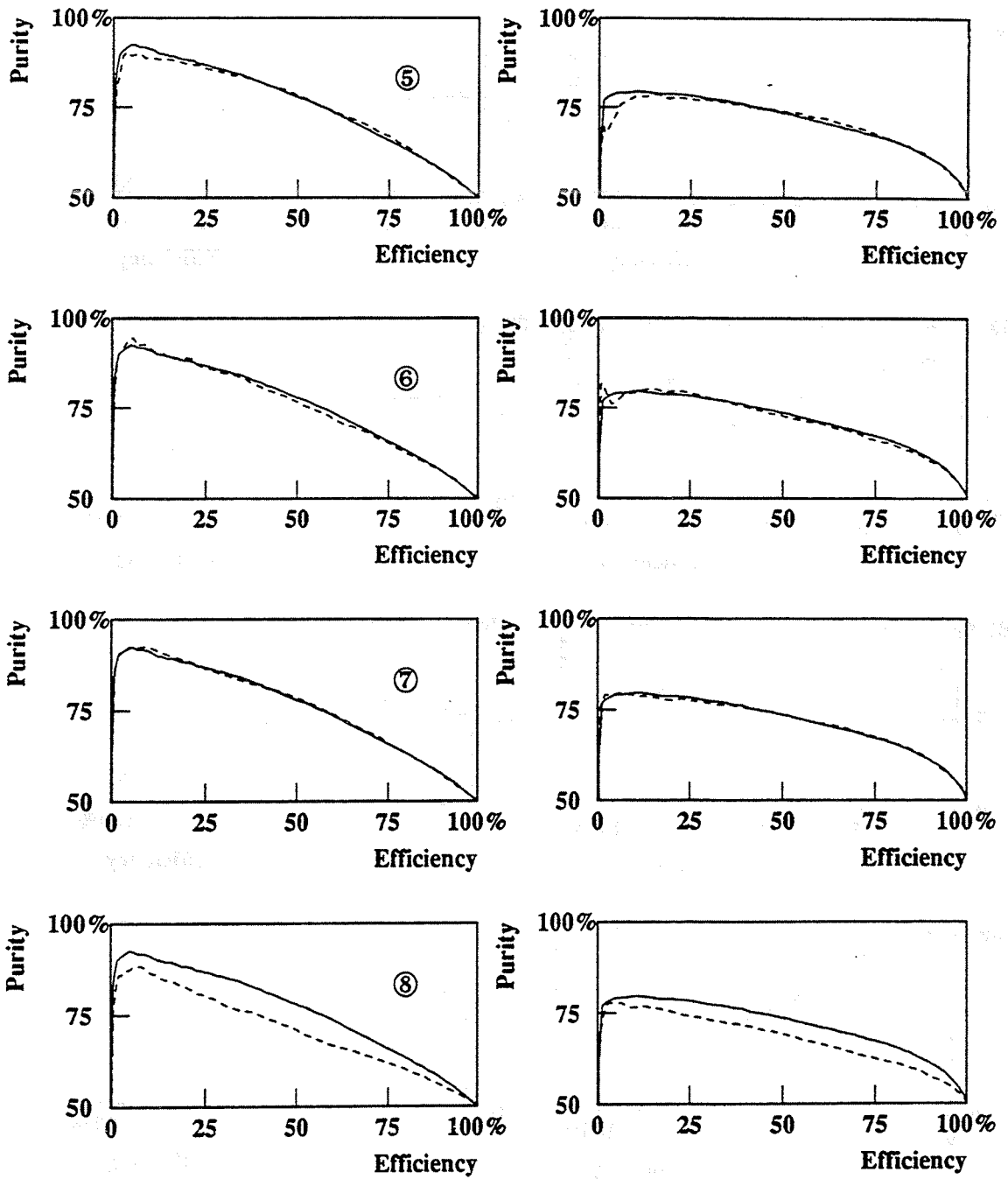

Appendix E

Addendum to: Evidence for the triple-gluon vertex from 4-jet events at LEP

Addendum to: Evidence for the triple-gluon vertex from 4-jet events at LEP

DELPHI Collaboration

Abstract

In this addendum we present a new type of jet classification, based on Neural Network technique. The classification is proved to be insensitive to the jet energy, i.e. it exploits only the fragmentation differences between quarks and gluons. Thus, we can make a measurement of N_c/C_f and T_R/C_f which is basically independent from our previous one where the jet energy was used to classify the jets. For the data taken with the DELPHI detector during 1991 we get the result: $N_c/C_f = 2.53 \pm 0.08(stat.)$. The small statistical error reflects the fact that the new method has a better identification of the parton origin of the jets. The model dependence and its influence on the fit result is discussed and quantified.

1 Jet classification method

In [1] the following moments were suggested:

$$M_{nm}(E_j) = \sum (\frac{p_t}{E_j})^n \eta^m \tag{1}$$

where the sum is taken over all particles assigned to the jet. p_t and η are the transverse momentum and pseudo rapidity of the particle with respect to the jet-axis. E_j is the jet energy. As pointed out in [1] these moments are sensitive to the softer fragmentation, higher multiplicity and broader p_t of the gluon jets as compared to the quark jets. Among the 7×7 first moments M_{10}, M_{11}, M_{14}, M_{15}, M_{16}, M_{25}, M_{26} and M_{27}, depicted in Figure 1 give best separation between quarks and gluons. Apparent from the figure is that at least the first 6 moments show a non-negligible energy dependence. Since the quarks (gluons) are more likely to populate the high (low) energy region in those moments we would still indirectly use the jet energy as a classifier. The fact that the quark and gluon lines in each diagram are nearly parallel suggests that the energy dependence can be eliminated. Formally we define a new set of variables:

$$F_{nm}(E_j) = \frac{M_{nm}(E_j)}{\overline{M_{nm}(E_j)}} \tag{2}$$

where the mean value indicated in the denominator is taken over all the jets with energy E_j in the sample. By construction the average value, $\overline{F_{mn}(E_j)}$, is of course 1 but for each class (q,g) separately it is not, see Figure 2. In particular, the separation between $F^q_{nm}(E_j)$ and $F^g_{nm}(E_j)$ is larger than their E_j dependence.

To achieve optimal separation between quarks and gluons in the eight defined variables, a "Feed Forward Neural Network" [2] is trained. Two samples of a few thousand JETSET 7.3 parton shower + detector simulated events are prepared for the NNw. One sample is used for training and the other for testing the generalizability of the NNw. Hadronic events are selected

as before with the addition that we use neutral particles in $0.5 \leq E \leq 45$ (GeV). The jet search algorithm LUCLUS defines our jets with the resolution parameter $djoin = 4$ (GeV). In order to have reasonable statistics in the sum (eq. 1) a jet is required to have a minimum multiplicity of 4 particles and a measured energy of at least 7 GeV. Finally, in order to comply to the invariant mass cut-off in the Matrix Element Monte-Carlo used in the fit, the minimum invariant mass of a jet pair is required to be greater than 9.1 GeV. As before we check that the Monte Carlo does describe the data well, in particular for the neutral particle distributions.

The jets are classified such that the two most "quark like" jets, i.e. those giving a NNw response closest to the quark target value, are assigned as the primary $q\bar{q}$ pair and the other two as the secondary partons. The typical performance of the NNw on a $q\bar{q}gg$ event in the test sample is 46% probability of correctly assigning all four jets, whereas it is about 10% lower if the jets are classified from their energy (charged + neutral).

2 Results

The full 4-jet analysis is repeated with the jet energy classification everywhere replaced by the identification method described in previous section. The two-dimensional distributions for the five split classes are given in Figure 3. Figure 4 shows the corrected 1991 DELPHI data and the fitted distribution together with the quadratic parametrization of the correction matrix for the detector. The data contain 6230 4-jet events. The free fit yields the following results:

$$\frac{N_c}{C_f} = 2.53 \pm 0.08(stat.)$$

and

$$\frac{T_R}{C_f} = 1.62 \pm 0.41(stat.)$$

The statistical errors are much smaller compared to the ones in our previous study mainly due to the improved jet identification. The χ^2 for 20×20 bins was 429.

3 Fragmentation model dependence

Since the jet identification is based on the feature of fragmentation a certain model dependence is expected. We try to estimate this dependence by varying the parameters in the Monte Carlo. The limits, within which to vary the parameters, would preferably be decided so that the Monte Carlo still describes the data for important distributions such as thrust, rapidity, 3-jet rate etc. . As a first attempt, however, we fix the limits to $\pm 10\%$ in three of the most important parameters in the JETSET parton shower + string fragmentation model; PARJ(21), PARJ(41) and PARJ(81). By randomly pick twenty points in the parameter space, we produce training samples for 20 new neural networks. All the networks are trained in a similar manner though small differences are unavoidable due to the random initialization phase of the NNw. Each NNw is subjected to the JETSET matrix element QCD and Abelian generator data samples that were produced for the fit above. After extracting the new classes A-E and running the fit-program, the results are entered into the histograms in Figure 5. The 10% variation in the model parameters give about 5% fluctuation in N_c/C_f.

4 Conclusions

It has been shown how to identify the parton origin of a jet by exploiting the fragmentation differences between quarks and gluons. The jet energy is not used in this method. Applying it to the 4-jet study presented in the main paper, the triple-gluon vertex contribution in second order QCD is found to be required by the data. In detector simulated Monte Carlo data, the identification of the two jets originating from the primary partons in 4-jet events, is about 10% better than with the jet energy classification.

An attempt to estimate the fragmentation model dependence shows that a 10% variation of 3 important parameters in the Monte Carlo results in a 5% fluctuation of N_c/C_f.

5 Figure captions.

Figure 1 The jet-energy dependence of the average value of the moments (eq. 1) in 4-jet events.

Figure 2 The moments in Figure 1 after the jet-energy dependence has been divided out (eq. 2).

Figure 3 Two-dimensional distributions in $|cos\Theta_{NR}|$ and $cos\alpha_{34}$ for the 5 classes A,B,C,D and E.

Figure 4 DELPHI 1991 data, the fitted distribution and the quadratic fit to the correction matrix.

Figure 5 The variation of the fit result for N_c/C_f and T_R/C_f over the sample of 20 different neural networks.

References

[1] See for instance: Z.Fodor, ITP Budapest Report No.465 (1988); Z.Fodor, invited talk at the Triangle Meeting on Particle Physics, Vienna 1989, Preprint UWThPh-1989-64; Z.Fodor, Phys. Lett. B263 (1991) 305-310.

[2] L.Lönnblad, C.Peterson and T.Röngvaldsson, Phys. Rev. Lett. 65 (1990) 1321; Nucl. Phys. B349 (1991) 675.
D.E.Rumelhart, G.E.Hinton and R.J.Williams, Learning Internal Representation by Error Propagation in D.E.Rumelhart and J.L.McClelland (Eds.) Parallell Distributed Processing: Explorations in the Microstructure of Cognition (Vol. 1), MIT Press (1986).
J.Dayhoff, Neural Network Architectures: An Introduction, Van Nostrand Reinhold(1990).

Figure 1

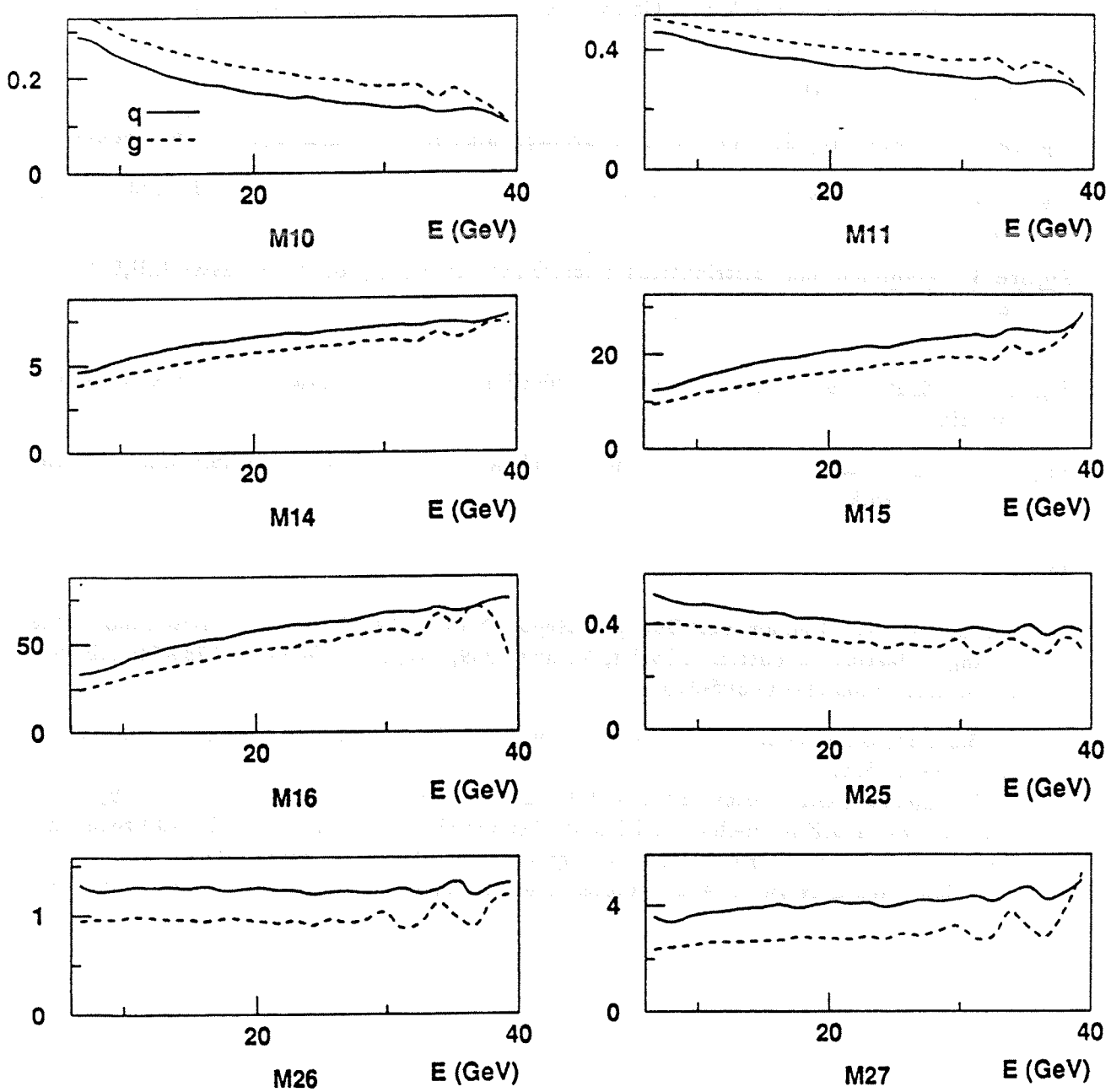
0.2
0
q
g
20
40
M10
E (GeV)
0.4
0
20
40
M11
E (GeV)
5
0
20
40
M14
E (GeV)
20
0
20
40
M15
E (GeV)
50
0
20
40
M16
E (GeV)
0.4
0
20
40
M25
E (GeV)
1
0
20
40
M26
E (GeV)
4
0
20
40
M27
E (GeV)

Figure 2

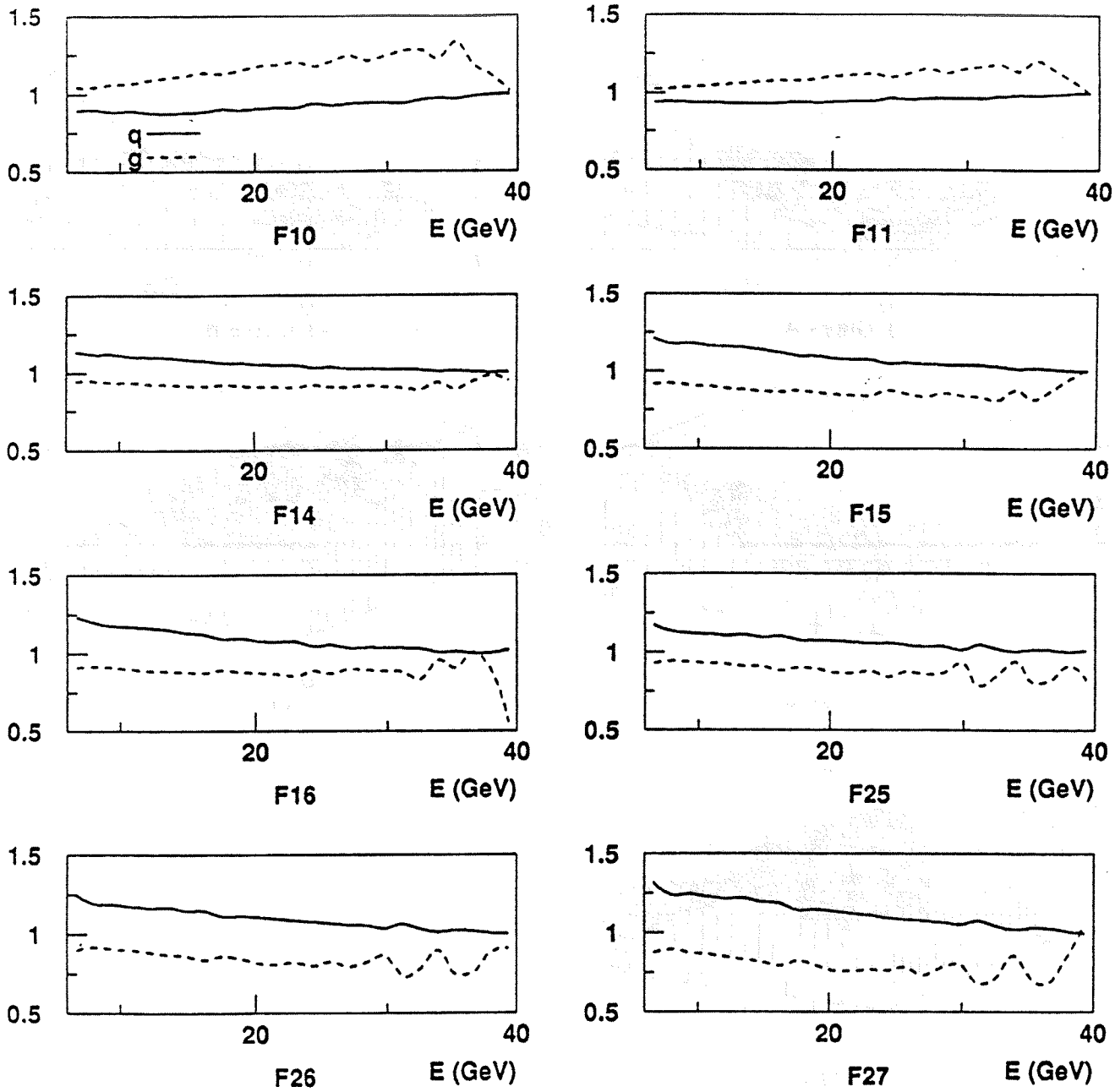

Figure 3

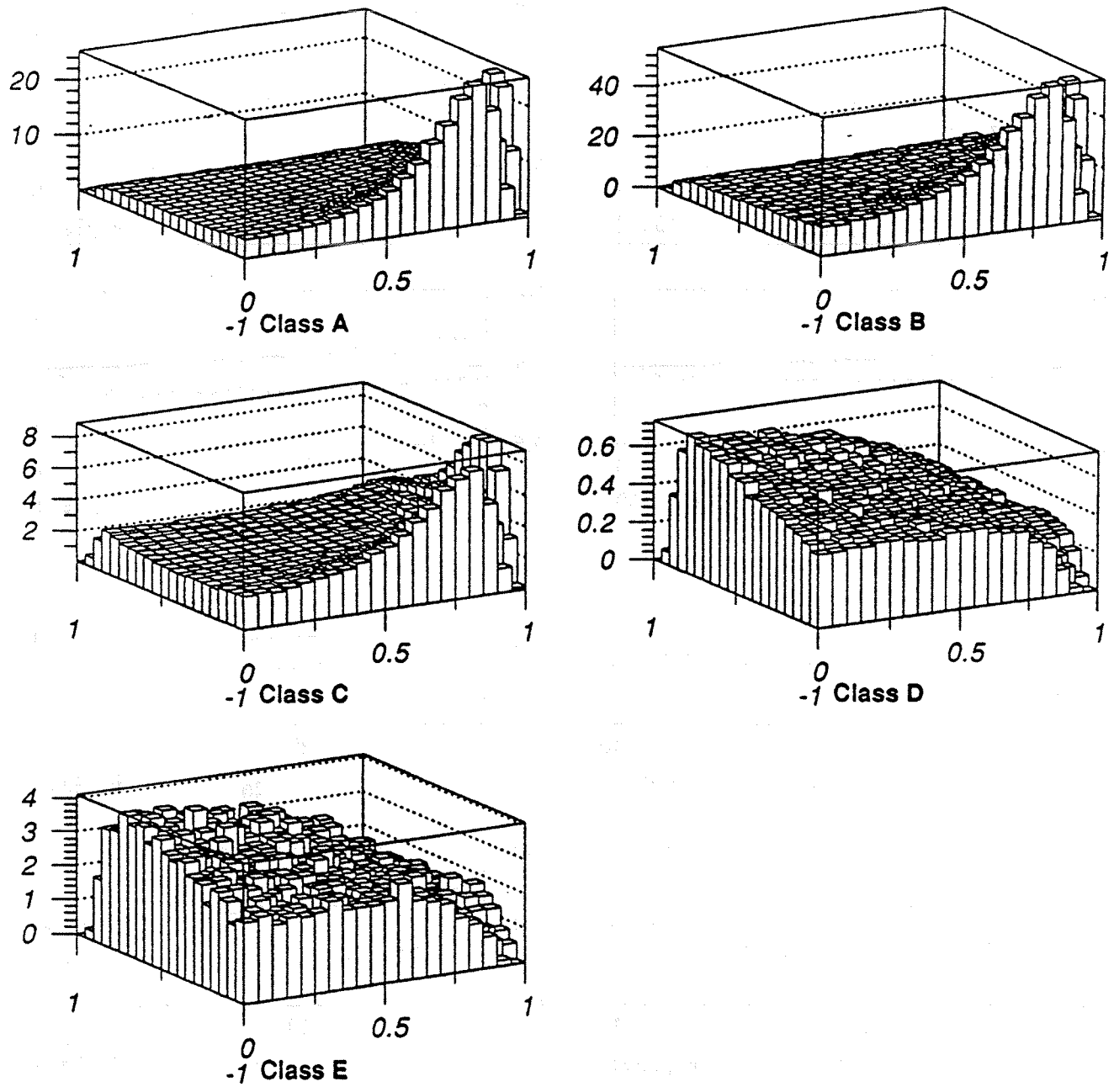
20
10
1
0.5
1
0
-1
Class A
40
20
0
1
0.5
1
0
-1
Class B
8
6
4
2
1
0.5
1
0
-1
Class C
0.6
0.4
0.2
0
1
0.5
1
0
-1
Class D
4
3
2
1
0
1
0.5
1
0
-1
Class E

Figure 4

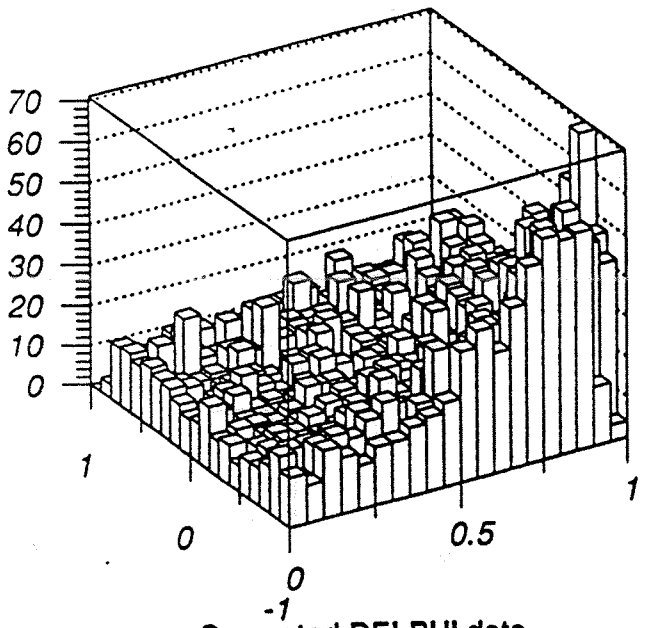

Corrected DELPHI data

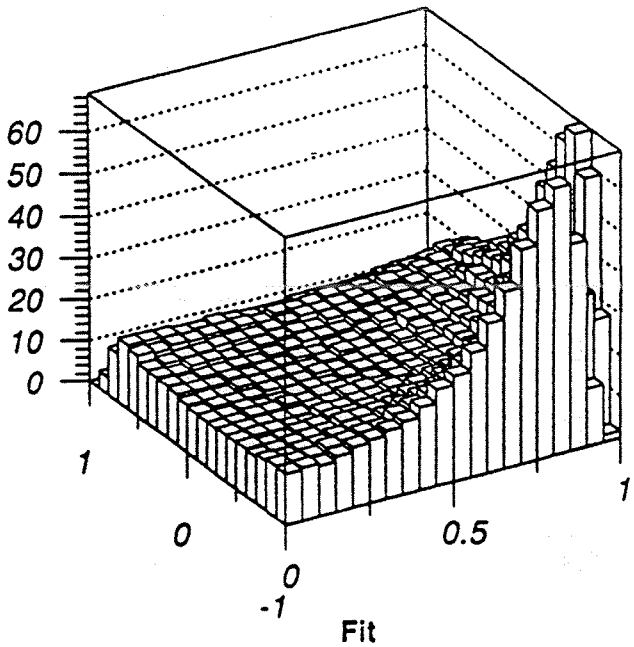

Fit

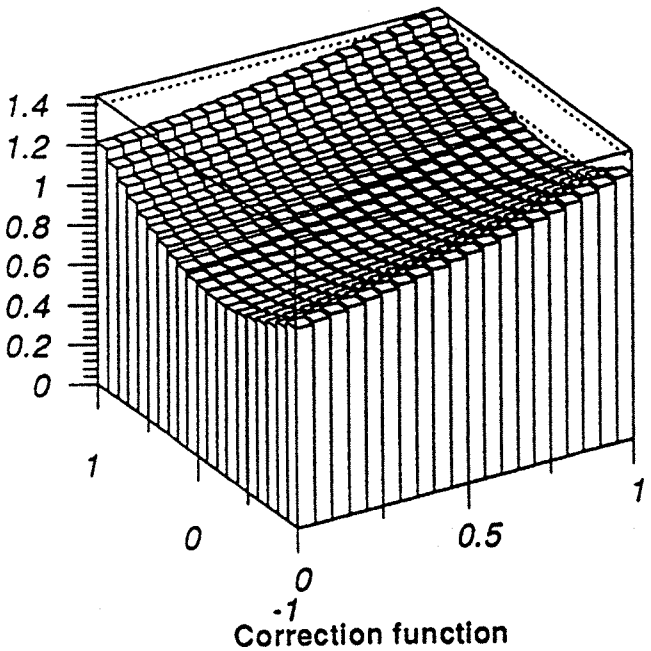

Correction function

Figure 5

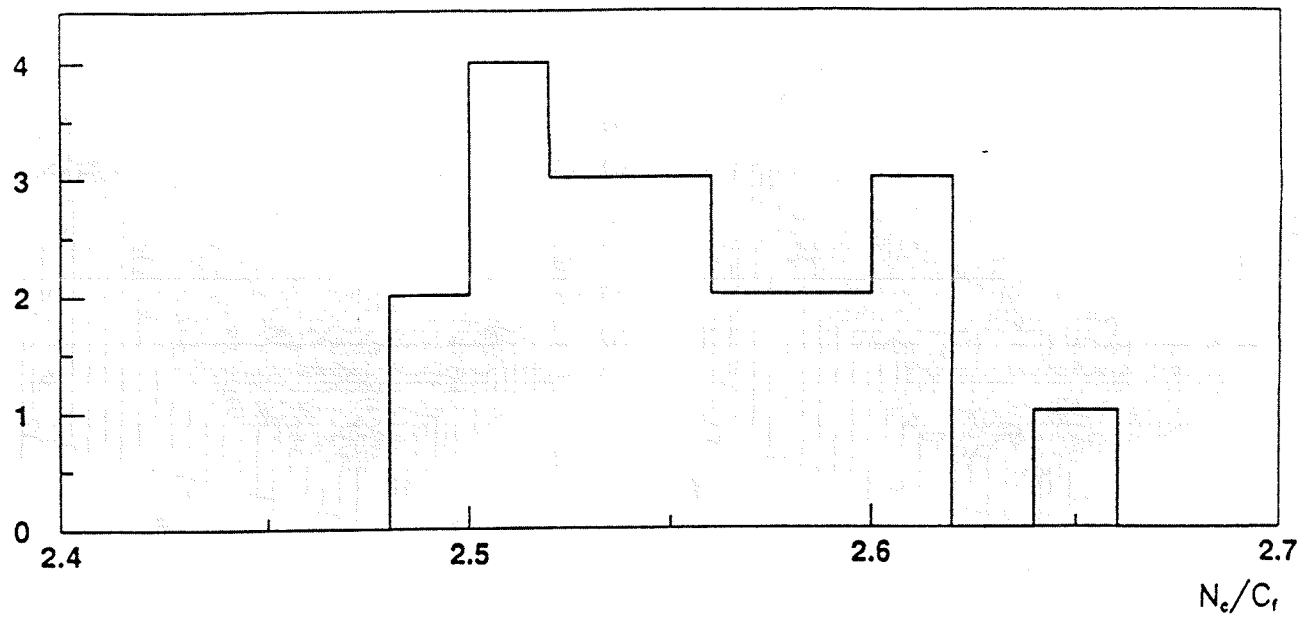

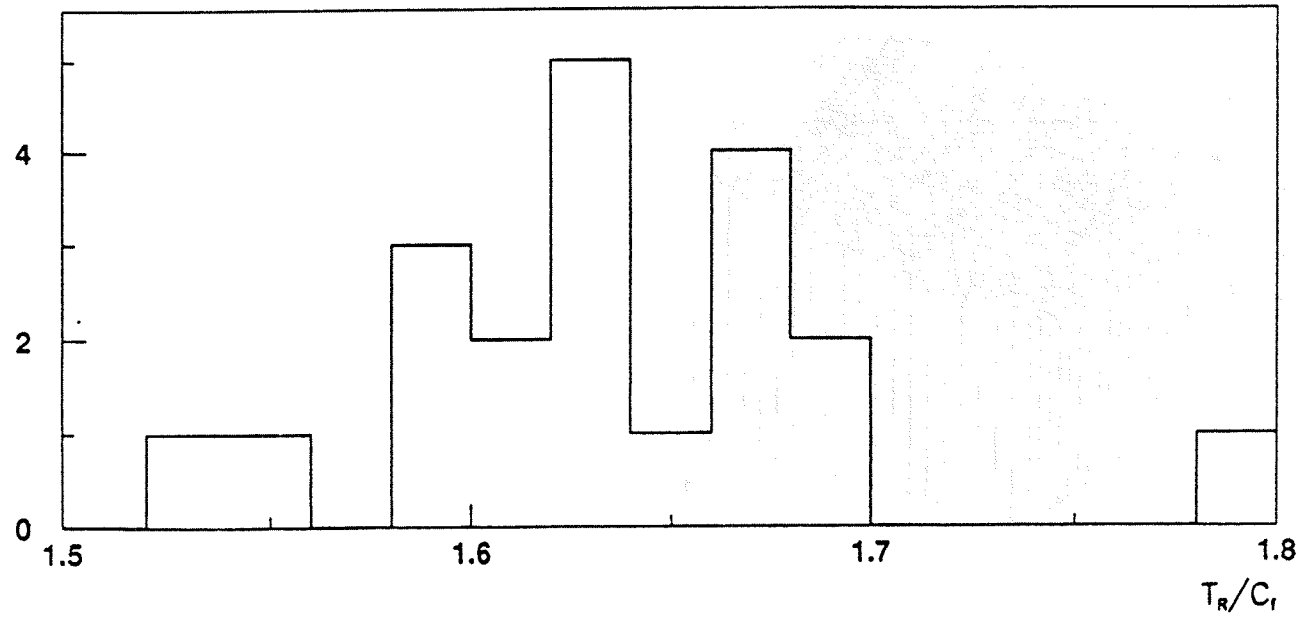

Bibliography

[1] DELPHI Coll., P.Aarnio et al.: Nucl. Instr. Methods A303 (1991) 233.

[2] F.Hartjes et al.: Nucl. Instr. Methods A256 (1987) 55

[3] C.Brand et al.: IEEE Trans. Nucl. Sci. NS-36 (1989) 122;
C.Brand et al.: Nucl. Instr. Methods A283 (1989) 567;
Y.Sacquin: Contribution to the proceedings of the VIth International Wire Chamber Conference, Vienna;
L.Chevalier: Thèse, Université Paris Sud, July 20 1992;
G.Hamel de Monchenault: Thèse, DAPNIA/SPP 92-11

[4] O.Bärring: LUNFD6/(NFFL-7046) (1987), unpublished

[5] M.Shapiro. PhD Thesis, LBL-18820 (1984), unpublished

[6] A.Amery et al.: Nucl. Instr. Methods A283 (1989) 502

[7] M.Berggren et al.: Nucl. Instr. Methods 225 (1984) 477;
H.G. Fischer: Nucl. Instr. Methods A265 (1988) 218

[8] A.Firestone: DELPHI 91-111 CAL 83 (1991) unpublished P.Yepes: DELPHI 92-39 GEN 128 CAL 90 (1992) unpublished

[9] M.Calvi, C.Matteuzzi: DELPHI 92-28 CAL 87 (1992) unpublished

[10] P.Checcia et al.: Nucl. Instr. Methods A275 (1989) 49

[11] Ph.Charpentier: Proceedings of the CHEP conference, Tsukuba, March 11-18 1991;
M.Jonker: Proceedings of the CHEP conference, Tsukuba, March 11-18 1991

[12] A.Vacotto: CERN school of computing, Renesse (1986), CERN 87-04 (1987) 147

[13] J.Barlow et al.: IEEE trans. nucl. sci. 36 (1989) 1549

[14] DELPHI collaboration: DELPHI 89-15 PROG 130 (1989) unpublished;
DELPHI collaboration: DELPHI 89-68 PROG 143 (1989) unpublished;
DELPHI collaboration: DELPHI 89-44 PROG 137 (1989) unpublished;
D.Bertrand, L.Pape; DELPHI 87-95 PROG 98 (1988) unpublished

[15] R.Brun et al.: PAW Reference Manual version 1.07, CERN Program Library entry Q121 (1989);
V.Berezhnoi et al.: CERN Program Library entry L210 (1988)

[16] O.Bärring: Nucl. Instr. Methods A284 (1989) 459

[17] G.V.Marr and J.B.West, At. Data Nucl. Data Tables 18 (1976)

[18] L.Landau, J.Phys. USSR 8 (1944) 201

[19] L.Chevalier: Thèse, Université Paris Sud, July 20 1992

[20] See for instance:
F.Lapique and F.Piuz, Nucl. Instr. Methods, 175 (1980) 297;
W.W.M.Allison and J.H.Cobb, Ann. Rev. Nucl. Part. Sci. 30 (1980) 253;
W.W.M.Allison and P.R.S.Wright, Formulae and Methods in Experimental Data Evaluation (1984), vol. 2 part. E;
R.Talman, Nucl. Instr. Methods, 159 (1979) 189;
H.Bichsel, Phys. Rev., B1 (1970) 2854;
H.Bichsel, Phys. Rev., A9 (1974) 571;
H.Bichsel, Nucl. Instr. Methods, A235 (1985) 174;
H.Bichsel, Rev. of Mod. Phys., Vol. 60 (1988) 663;
V.M.Grishin,V.K.Ermilova and S.K.Kotelnikov, Nucl. Instr. Methods, A307 (1991) 273;
V.M.Grishin,V.K.Ermilova and S.K.Kotelnikov, Nucl. Instr. Methods, A309 (1991) 476

[21] DELPHI collab., Phys. Lett., B255 (1991) 466;
DELPHI 91-52 Phys 107: contribution to the Geneva-LP'91 Conference;
T.Hebbecker: Plenary talk at the Geneva-LP'91 Conference

[22] M.Hahn, M.Halpaap, H.Müller and A.Sietz, *Evidence for the Triple-Gluon Vertex from 4-jet Events at LEP*, Contribution to the Dallas Conference 1992.

[23] O.Bärring, Addendum to Evidence for the Triple-Gluon..., Contribution to the Dallas Conference 1992.

[24] T.Åkesson and O.Bärring, DELPHI 90-59 PHYS 78 (1990)

[25] O.Bärring, DELPHI92-38 PHYS 170 (1992)

[26] M.Bengtsson, Z.Phys., C42 (1989) 75

[27] B.Andersson, G.Gustafson, B.Söderberg, Z.Phys. C20 (1983) 317

[28] R.K.Ellis, D.A.Ross, A.E.Terrano, Nucl. Phys., B178 (1981) 421

[29] See for instance: Z.Fodor, ITP Budapest Report No.465 (1988); Z.Fodor, invited talk at the Triangle Meeting on Particle Physics, Vienna 1989, Preprint UWThPh-1989-64; Z.Fodor, Phys. Lett. B263 (1991) 305-310.

[30] L.Lönnblad, C.Peterson and T.Röngvaldsson, Phys. Rev. Lett. 65 (1990) 1321; Nucl. Phys. B349 (1991) 675
C.Peterson, Proceeding of the Neural Networks Workshop at Elba June 5-14 1991, p 338

[31] D.E.Rumelhart, G.E.Hinton and R.J.Williams, Learning Internal Representation by Error Propagation in D.E.Rumelhart and J.L.McClelland (Eds.) Parallell Distributed Processing: Explorations in the Microstructure of Cognition (Vol. 1), MIT Press (1986);
J.Dayhoff, Neural Network Architectures: An Introduction, Van Nostrand Reinhold(1990)

[32] T.Sjöstrand, Computer Phys. Comm. 39 (1986) 347;
LUCLUS is described in T.Sjöstrand, Computer. Phys. Comm. 28 (1983) 229

[33] M.Hahn, Thesis at Karlsruhe University, Germany, (1992)